Die approbierte Originalversion dieser Dissertation ist in der Hauptbibliothek der Technischen Universität Wien aufgestellt und zugänglich.
http://www.ub.tuwien.ac.at

The approved original version of this thesis is available at the main library of the Vienna University of Technology.
http://www.ub.tuwien.ac.at/eng

DISSERTATION

A novel method of thermally assisted photo-electrochemical energy conversion

ausgeführt zum Zwecke der Erlangung des akademischen Grades eines Doktors der Naturwissenschaften unter der Leitung von

ao.Univ.-Prof. Dipl.-Ing. Dr.techn. Karl PONWEISER

am Institut für
Energietechnik und Thermodynamik (E302)

eingereicht an der Technischen Universität Wien
Fakultät für Maschinenwesen und Betriebswissenschaften

von
Dipl.-Ing.(FH) Dipl.-Ing. Georg Chr. BRUNAUER
Matrikel-Nr.: 0728326, Kennzahl: E 791 700
Theresia Pampichler-Straße 44/1, 2000 Stockerau

Wien, am 30.06.2016

Eigenhändige Unterschrift

PREAMBLE

The present work was inspired by the vision of converting solar radiation into chemical energy. After seven eventful years, characterized by many periods of drought but also by scientific breakthroughs, I am still fascinated…

At the beginning of this story, an abstract idea of energy conversion by using solar energy started to reveal itself. I can look back on a very intensive period and formative experiences: the first conceptual ideas, establishment of a high-tech start-up, a large project grant, and after a long period of restraint … the desired progress in scientific work, finalizing this PhD thesis.

But that is not the end of the story: there are people who accompanied me along the way. Now it is time to say to all of them THANK YOU…

First of all, my sincere thanks are owed to my whole family. A new joy in life I've found in my wife Maria-Christina and in our son Emmanuel.
My career was followed by highs and lows. In all these situations I've appreciated Prof. Karl Ponweiser personally as a mentor. Finally, I gratefully acknowledge all the scientific support and accommodation by the research group of solid state electrochemistry, directed by Prof. Jürgen Fleig.

And even though, with the completion of this thesis, the story now comes to this important milestone, I believe that GOD will continue …

OPENING CITATIONS

Both religion and science require a belief in God. For believers, God is in the beginning, and for physicists He is at the end of all considerations…
To the former He is the foundation, to the latter, the crown of the edifice of every generalized world view.

Max Planck

I am the Lord, and there is no other, besides me there is no God; I equip you, though you do not know me, that people may know, from the rising of the sun and from the west, that there is none besides me; I am the Lord, and there is no other. I form light and create darkness, I make well-being and create calamity, I am the Lord, who does all these things. "Shower, O heavens, from above, and let the clouds rain down righteousness; let the earth open, that salvation and righteousness may bear fruit; let the earth cause them both to sprout; I the Lord have created it.
In the same way, let your light shine before others, so that they may see your good works and give glory to your Father who is in heaven

Isaiah 45:5-8
Matthew 5:16

I want to know how God created this world…
I want to know His thoughts.

Albert Einstein

KURZFASSUNG

Die Wasserzerlegung mittels Solarstrahlung stellt eine vielversprechende Methode zur Energiespeicherung dar. Als Energiequelle für einen derartigen Prozess dient konzentrierte Solarstrahlung. Diese ist uneingeschränkt verfügbar und im höchsten Maße erneuerbar. Wasser(-dampf) dient hierbei als Ausgangsstoff. Der daraus gewonnene Kraftstoff (z.B. Wasserstoff), und die bei dessen Umwandlung (Verbrennung) entstehenden Emissionen (Wasserdampf) sind im hohen Grad umweltverträglich. Die vorliegende Arbeit widmet sich einem grundlegend neuen Ansatz zur Umwandlung von kurzwelliger (UV-) Strahlung in chemische Energie. Die Energieumwandlung (bspw. die Wasserzerlegung) erfolgt photo-elektrochemisch in einem thermisch aktivierten Zustand.

Ein bewährtes Verfahren zur Produktion von Wasserstoff ist die Hochtemperatur-Wasserdampfelektrolyse. Die benötigte elektrische Energie für diesen Elektrolyse-prozess kann einerseits mit konventionellen Kraftwerken (fossil, Kernkraft) oder mit erneuerbaren Methoden (Wasserkraft, Sonne, Wind) generiert werden. Alternative Methoden zur Produktion von solarem Wasserstoff befinden sich derzeit noch im Stand der (Grundlagen-)Forschung: zwei- oder mehrstufige thermochemische Wasserzerlegung basierend auf Metalloxiden und die Photoelektrolyse nahe bei Raumtemperatur, unter der Verwendung photoaktiver Elektroden. Trotz intensiver wissenschaftlicher Anstrengungen im Bereich der photo-elektrochemischen Zellen (*kurz*: PEC) liegen die erzielten Wirkungsgrade bislang noch immer deutlich unterhalb jener von bereits etablierten Technologien. Ein Vertreter einer solchen Technologie ist: Photovoltaik & Elektrolyse. Materialchemische Aspekte, wie die Stabilität, etc. zählen hier zu den Herausforderungen.

Das Ziel der vorliegenden Arbeit beruht auf dem Erarbeiten von neuem Grundlagenwissen zur Realisierung einer thermisch aktivierten, photo-elektrochemischen Energieumwandlung. Realisiert findet sich dieser neuartige Ansatz in einer *Solid Oxid Photo-Electrochemical Cell* (*kurz*: SOPEC). Die Vorteile hier sind: *i*) Vermeidung von Stabilitätsproblemen des Elektrodenmaterials in wässriger Umgebung, *ii*) Herabsetzen der theoretischen Wasserzerlegungsspannung, *iii*) die Möglichkeit der Produktion von Wasserstoff bei Drücken unterhalb des Umgebungsdrucks, *iv*) die Vermeidung zusätzlicher Elektrolysespannung und *v*) die Bildung von Synthesegas. Die unter kurzwelliger Strahlung (UV-Licht) generierte Spannung (und Strom) führt letztlich dazu, Sauerstoff durch die Zelle elektrochemisch bei Temperaturen von 400-500°C zu pumpen. Als ambitioniertes Ziel galt es die Möglichkeit der thermisch aktivierten, photo-elektrochemischen Energieumwandlung, basierend Mischmetalloxiden zu beweisen.

ABSTRACT

Solar energy driven water-splitting combines several attractive features for energy utilization. Concentrated solar radiation represents the energy source for such process. It is readily available and is supremely renewable. Water is used as base stock. The resultant fuel (generated hydrogen) and the emissions with fuel consumption (water steam) are environmentally benign. The present work is about a new approach for the energy conversion using short wave-length (UV-vis) radiation. Here, the water splitting process follows a photo-electrochemical reaction regime assisted by a thermochemical reaction.

One option for electrochemical hydrogen production is high-temperature steam electrolysis. The electrical power necessary for such electrochemical process can be provided by conventional conversions methods (fossil and nuclear power plants) or by renewable energy sources (hydrodynamic, sun, wind). Alternative technologies for producing hydrogen in a single set-up are still under research and/or development: Thermochemical water splitting based on oxides at two different temperatures and photo-electrochemical water splitting using photoactive electrodes. Despite huge research efforts, efficiencies of photo-electrochemical cells are still far below those of established technologies and the best photo-anodes (from an efficiency point of view) often suffer from degradation in aqueous solutions. For further developing one-cell based devices, very new and innovative ways have to be paved.

It is the goal of this thesis to perform basic research on mixed conducting metal oxides, generating fundamental knowledge necessary for realizing high-temperature (350-500 °C) photo-electrochemical water splitting in a solid electrolyte based cell; named *Solid Oxid Photo-Electrochemical Cell* (SOPEC). Advantages are: *i*) avoidance of stability problems of electrodes in aqueous water, *ii*) lowering the theoretical water splitting voltage, *iii*) the possibility for producing hydrogen already at pressures lower than ambient pressure, *iv*) avoiding additional bias voltages and *v*) enabling formation of synthesis gas and thus reactions to hydrocarbons in the same cell due to high cell operation temperatures. The entire SOPEC consists of a high-temperature photovoltaic (HT-PV) part and an electrochemical cell part. Under short-wave radiation (UV light), this driving force is used in the electrochemical part of the cell to pump oxygen from low to high partial pressures. The experiments demonstrate the feasibility of high-temperature photo-electrochemical cells for solar energy storage. This ambitious thesis is therefore basic research with an applied focus, namely the long term goal of solar fuel production. It may initialize a new technology for chemical energy conversion in combination with materials research at so far unknown combinations of materials.

NOMENCLATURE

Abbreviations

Variable	Description
(g)	index; gaseous
(l)	index; liquid
(s)	index; solid
AC	alternating current
CO	carbon monoxide
CO_2	carbon dioxide
DC	direct current
e.g.	exempli gratia; for example
EC	electrochemical cell
EIS	electrochemical impedance spectroscopy
FC	fuel cell
Fe	Iron
H^+	proton
H_2	molecular hydrogen
H_2O	water, water steam
HTE	high-temperature electrolysis
HT-PV	high-temperature photovoltaic
i.e.	id est; that is
LED	light emitting diode
LSCr82	20% strontium doped lanthanum chromite
LSCr91	10% strontium doped lanthanum chromite
LSF64	40% strontium doped lanthanum ferrite
MeO_x	metal oxide
O_2	molecular oxygen
O^{2-}	oxygen ion
PEC	photo-electrochemical cell
PEM	proton exchange membrane
PLD	pulsed laser deposition
Pt	platinum
sc	short-circuit
SEM	scanning electron microscopy
SOEC	solid oxide electrolysis cell

SOFC	solid oxide fuel cell
SOPEC	solid oxide photo-electrochemical cell
$SrTiO_3$	strontium titanate
STF73	30% iron doped strontium titanate
TZP	tetragonal zirconia polycrystal
UV	ultra violet
V-I	voltage-current measurement
vis	visible
XRD	X-ray diffraction
YSZ	yttria stabilized zirconia

Formula units

Variable	Description	Unit
$\dot{S}_{irr\,hydrolyser}$	irreversibilities during water-splitting reaction	J (mol s K) $^{-1}$
$\dot{S}_{irr\,quench}$	irreversibilities during quench peocess	J (mol s K) $^{-1}$
$\dot{S}_{irr\,reactor}$	irreversibilities in solarchemical reactor	J (mol s K) $^{-1}$
$\dot{Q}_{hydrolyser}$	heat losses during water-splitting process	W
$\dot{Q}_{FC}$	heat losses in fuel cell	W
$\dot{Q}_H$, $\dot{Q}_L$	heating power	W
$\dot{Q}_{quench}$	heat losses during quench process	W
$\dot{Q}_{reactor,net}$	net rate of solar radiation energy per unit of time	W
$\dot{Q}_{reradiation}$	re-radiation losses	W
$\dot{Q}_{solar}$	solar energy input per unit of time	W
$\dot{S}_Q$, $\dot{S}_{Q,H}$, $\dot{S}_{Q,L}$	entropy flow; high-, low-, level temperature	J (mol s K) $^{-1}$
$\dot{S}_{irr}$	irreversibilities	J (mol s K) $^{-1}$
$\dot{W}_{FC}$	electrical power generated by a fuel cell	W
h_{H_2O}, h_{H_2}, h_{O_2}	specific enthalpy	J kg^{-1}
$\dot{W}$	(electrical) power	W
$\dot{m}$, $\dot{m}_{H_2O}$, $\dot{m}_{H_2}$, $\dot{m}_{O_2}$	mass flow, -water, -hydrogen, -oxygen	kg s^{-1}
$\dot{n}$	molar mass flow	mol s^{-1}
s_{H_2O}, s_{H_2}, s_{O_2}	specific entropy	J (kg K)$^{-1}$
A, A_{cell}	area, cell surface	cm^{-2}

C	solar concentration ratio	-
E_g	bang gap	eV
E_t	threshold energy	eV
F	Faraday constant	96485.3365 C mol^{-1}
f	frequency	Hz
f_m	molar flow rate	mol s^{-1}
f_{O2}	oxygen fraction	ppm
f_V	molar volume rate	m^3 s^{-1}
G, ΔG_r	Gibbs free energy, Gibbs free energy change of reaction	J mol^{-1}
H, ΔH_r	enthalpy, enthalpy change of reaction	J mol^{-1}
HHV	high heating value	J mol^{-1}
i	current density	A cm^{-2}
I	electrical current	A
Im[Z]	imaginary part of impedance Z	Ω
I_{PEC}	short-circuit current of the entire PEC cell	A
I_{PV}	photovoltaic current	A
$I_{PV,SC}$	photovoltaic short-circuit current	A
I_S	normal beam insulation	kW m^{-2}
j, $j\phi$	complex number, argument	-
j_{O2}, j_{gas}	molar flux of oxygen molecules, and for ideal gas	mol min^{-1}
LHV	low heating value	J mol^{-1}
n	molar weight	Mol
N_A	Avogadro's number	$6.02214 \cdot 10^{23}$ mol^{-1}
N_{cell}	number of (electrolysis) cells	-
p	pressure	N m^{-2}
Q	heat	J
Q_{gas}	gas flow rate	ml min^{-1}
$Q_{reactor,net}$	net rate of solar radiation energy	J
Q_{solar}	solar energy input	J
Re[Z]	real part of impedance Z	Ω
R_{EC}	internal resistance of electrochemical cell	Ω
$R_{EC,AC,ill}$	AC resistance of the electrochemical cell	Ω

$R_{EC,PEC}$	resistance of the operating electrochemical cell	Ω
R_m	molar Ideal gas constant	8.31445 J (mol K) $^{-1}$
R_{PV}	internal resistance of PV cell	Ω
$R_{PV,AC,ill}$	AC resistance of the illuminated PV cell	Ω
$R_{PV,diff}$	differential resistance of PV cell	V ΔA^{-1}
$R_{PV,PEC}$	resistance of PV cell in the operating PEC cell	Ω
S, ΔS_r	entropy, entropy change of reaction	J (mol K)
t	Time	S
T, T_H, T_L	temperature; high-, low-, level temperature	K
T_{dark}	temperature in dark	°C
T_{setup}	setup temperature	°C
T_{UV}	temperature under UV light	°C
U	internal energy	J
U_{EC}	voltage of the EC cell part	V
U_N	Nernst voltage	V
U_{PEC}	voltage under PEC operating conditions	V
U_{PV}	photovoltaic voltage	V
$U_{PV,OC}$	photovoltaic voltage of open circuit	V
V_r	voltage for the electrochemical water-splitting reaction	V
V_{rev}	reversible voltage	V
V_{stack}, V_{cell}	voltage, -stack, -cell	V
V_{th}	thermo neutral voltage	V
W, W_{rev}	work, energy; reversible work	J
x_j	mole fraction of the considered species j	mol s^{-1}
z	number of electrons per mole of product turnover	-
Z, Z_0	impedance, magnitude of impedance	Ω
α_{eff}	effective absorptivity	-
ε_{eff}	effective emissivity	-
$\eta_{absorption}$	absorption efficiency	-
η_{cell}	cell efficiency	-
η_{con}	overpotential related to mass transport of the chemical species	V

η_{ct}	overpotential related to charge transfer	V
η_{EC}	voltage efficiency (in electrolysis cell)	-
$\eta_{EC,F}$	Faraday efficiency	-
η_{exergy}	exergy efficiency	-
η_{PV}	voltage loss in the PV cell	V
η_{stack}	(electrolysis) stack efficiency	-
η_{Ω}	ohmic overvoltage	V
σ	Stefan-Boltzmann constant	$5{,}67037 \cdot 10^{-8}$ $W(m^2K^4)^{-1}$
ω	radial frequency	s^{-1}
ω_b	relaxation frequency of the bulk	s^{-1}
ω_{sc}	relaxation frequency of the interfacial space charge	s^{-1}
Φ	phase shift, argument	°

TABLE OF CONTENTS

Preamble……i
Opening citations……...ii
Kurzfassung……...iii
Abstract……iv
Nomenclature……..v
Table of contents……x
1 Theory of thermodynamics……..1
1.1 Thermodynamics of thermal dissociation……..2
1.2 Thermodynamics of high-temperature electrolysis……..3
1.3 Fundamentals of electrolysis……5
2 State of knowledge……9
2.1 Overview……...10
2.2 Solar thermochemical path……11
2.2.1 Direct thermal dissociation of water……12
2.2.2 Two-step water-splitting cycles……13
2.3 High-temperature electrolysis……...19
2.4 Photo-electrochemical water-splitting……..24
3 Experimental investigation and discussion……28
3.1 Principle……29
3.1.1 Pre-study considerations……30
3.1.2 Pre-experimental study……..34
3.2 New conceptual research and approach……..43
3.2.1 Photoconductivity of STO (100) single crystal……44
3.2.2 Photochemical properties of STO (100) single crystal……...46
3.2.3 Investigation of $SrTiO_3$(100)/ $La_{0.8}Sr_{0.2}CrO_3$ heterojunction……...50
3.3 The high-temperature Photoelectrochemical Cell (SOPEC)……..62
3.3.1 Design of experimental setup……62
3.3.2 Structure of SOPEC cell and measurement arrangement……63
3.3.3 Characterization of SOPEC cell under operation condition……66
3.3.4 Experimental proof of UV-driven oxygen pumping……70
4 Compilation of the essential results and conclusions……..76
4.1 Acknowledgements……77
4.2 Introduction……..77
4.3 The high-temperature photoelectrochemical cell……78
4.4 Results and discussion……80

4.4.1 UV-light-driven oxygen pumping in the solid state photoelectrochemical cell……80
4.4.2 Characterization of the high-temperature photoelectrochemical cell and the electrochemical cell……85
4.5 Experimental section……...92
4.6 Conclusions……...94
5 Appendix……95
5.1 List of figures……96
5.2 List of tables……102
5.3 References……...103
5.4 Curriculum vitae (CV)……..111

1 THEORY OF THERMODYNAMICS

The energy conversion proceeds according to thermodynamic laws. Hereby in this thesis, the main emphasis lies on a new novel method for photoelectrochemical energy conversion. Before starting with the introduction of this method some aspects according to the current state of knowledge are going to be discussed. These include the techniques for **thermochemical**, **electrochemical** and **photochemical** energy conversion.

1.1 Thermodynamics of thermal dissociation

A basic thermodynamic analysis can be applied to describe a thermal water splitting process in order to determine overall process efficiency limits as a function of temperature and pressure. In **Figure 1.1** a process diagram for thermochemical water-splitting is shown.

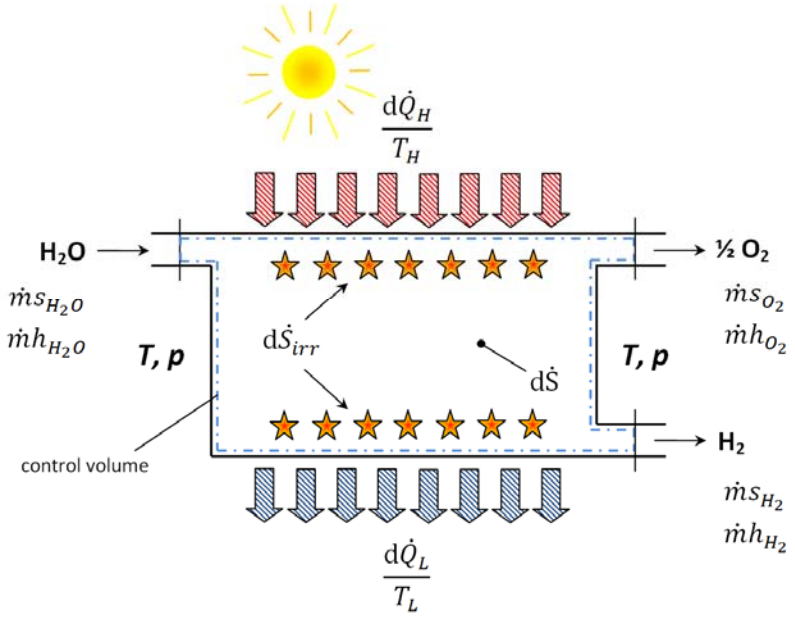

Figure 1.1: Schematic of a stationary thermal water-splitting process operating between a high-temperature (T_H) and a low-temperature (T_L) level

Water enters the control volume (CV) with a *specific entropy* and *enthalpy* ($\dot{m}s_{H_2O}$, $\dot{m}h_{H_2O}$) at a specified temperature T and pressure p. Pure hydrogen and oxygen at a *specific entropy* and *specific enthalpy* ($\dot{m}s_{H_2}$, $\dot{m}h_{H_2}$, $\dot{m}s_{O_2}$, $\dot{m}s_{O_2}$) also at T and p leave the control volume. Two heat sources are available, a high-temperature source at temperature T_H and a low-temperature source at temperature T_L. With the heat transfer between these reservoirs and the control volume (indicated with $\dot{Q}_H$, $\dot{Q}_L$) also the corresponding entropy flow ($\dot{S}_{Q,H}$, $\dot{S}_{Q,L}$) crosses the system boundary. Note: the heat flux to the low-temperature level $\dot{Q}_L$ is placed outward from the CV's point of view, *i.e.* heat flux against the direction of the arrow. Therefore, $\dot{Q}_L$ has to be considered as a negative term. Irreversibilities ($\dot{S}_{irr}$) during the solar thermochemical conversion process arise from non-reversible chemical transformation and re-radiation losses to the ambient. For simplification, no electrical or mechanical work (*e.g.* pumping work) is crossing the control volume boundary.

The thermochemical water-splitting reaction corresponds to the reduction or dissociation of water, and is given by

$$H_2O \rightarrow H_2 + \frac{1}{2}O_2\,. \tag{1.1}$$

The *first* and the *second law* of thermodynamics can be applied for a stationary thermochemical water-splitting flow process as follows

1st law: $$\dot{Q}_H - \dot{Q}_L = \dot{n}\Delta H_r \tag{1.2}$$

and

2nd law: $$\dot{n}\,\Delta S_r = \frac{\dot{Q}_H}{T_H} - \frac{\dot{Q}_L}{T_L} \geq 0, \tag{1.3}$$

where ΔH_r is the change of enthalpy of reaction and ΔS_r is the change of entropy of the reaction.

The balance of the entropy for a steady-state flow processes according Fig. 1.1 is given as follows:

$$\sum_{\text{output}} \dot{m}_o s_o = \sum_{\text{input}} \dot{m}_i s_i + \dot{S}_Q + \dot{S}_{irr}, \tag{1.4}$$

applied for an *adiabatic* steady-state flow process, $\dot{S}_{irr}$is defined as:

$$\dot{S}_{irr} = \left[\sum_{\text{output}} \dot{m}_o s_o - \sum_{\text{input}} \dot{m}_i s_i\right]_{\text{ad}} \geq 0. \tag{1.5}$$

The entropy according to Fig. 1.1 in differential notation is given as follows:

$$\mathrm{d}\dot{S} = \mathrm{d}\dot{S}_{irr} + \mathrm{d}\dot{S}_Q, \tag{1.6}$$

with

$$\mathrm{d}\dot{S}_Q = \frac{\mathrm{d}\dot{Q}}{T}. \tag{1.7}$$

Further on, this principle of the first and second law represents the basis for thermodynamic considerations of solar thermochemical two-step water-splitting processes as well as other processes (*e.g.* high-temperature electrolysis), which will be considered in the following.

1.2 Thermodynamics of high-temperature electrolysis

Hydrogen can be also produced by the thermo electrochemical water-splitting. Generally, such process takes place in a *High-Temperature Electrolyzer* (HTE). Commercial HTEs are using a *Solid Oxide Electrolysis Cell* (SOEC) which is a reversely

operated *Solid Oxide Fuel Cell* (SOFC). Focusing particularly now on HTE, therefore an isothermal high-temperature electrolysis with a control volume (CV) boundary is considered, as shown in **Figure 1.2**.

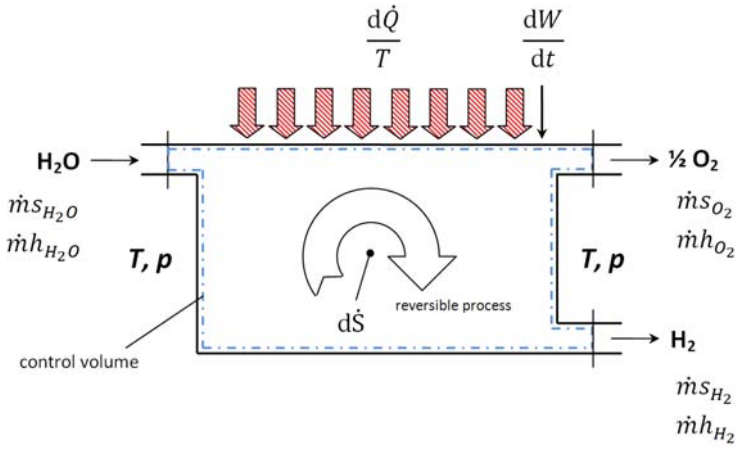

Figure 1.2: Schematic of a reversible stationary high- temperature electrolysis process operating at a constant high-temperature level (*T*) with a pressure (*p)*

In this case, instead of the considered thermochemical water-splitting process before, heat and work cross the control volume boundary. The first law of thermodynamics has to be adapted for this process, and is given by

$$\dot{Q} + \dot{W} = \dot{n}\,\Delta H_r, \tag{1.8}$$

where $\dot{W}$ represents the electrical power which is equal to the differential notation dW/dt = P according Fig. 1.2 and is crossing the control volume boundary. In general, the energy balance for an electrolysis system can be expressed as

$$\dot{Q} + \dot{W} = \dot{n}\,\Delta H_r = \sum_{\mathrm{P}} \dot{n}_i H_{r,i}\,(T_p, p_p) - \sum_{\mathrm{R}} \dot{n}_j H_{r,j}\,(T_R, p_R). \tag{1.9}$$

The equation Eq. 1.8 and Eq. 1.9 shall apply for state-state flow electrolysis processes, where $\dot{Q}$ represents an external heat transfer rate to the electrolyser, $\dot{W}$ is the rate of electrical power supplied to the electrolysis system, the term $\dot{n}\Delta H_r$ is the enthalpy rate of the reaction system, $\dot{n}_i$ is the molar flow rate of each reactant R or product P, $H_{r,i,j}$ is the molar enthalpy of reaction for each reactant or product, T_R and p_R are the reactant temperature and pressure at the inlet of the electrolysis system, and T_P and p_P are the product temperature and pressure at the outlet of the electrolysis system.

For a complete thermodynamic description, the entropy must also be taken into consideration. The equation for the second law of reversible processes is as follows

$$\dot{n}\Delta S_r = \frac{\dot{Q}_{rev}}{T}. \tag{1.10}$$

As a fundamental result of the first and second law, the relationship of energies is defined as:

$$W_{rev} = \Delta H_r - T\Delta S_r = \Delta G_r. \tag{1.11}$$

The Gibbs free energy ΔG is the *maximum* amount of *non-expansion* work W_{rev} that can be extracted from a *thermodynamically closed system*. Such maximum can only be achieved in a completely *reversible process*. Gibbs free energy differs from *Helmholtz free energy* ($F = U - T{\cdot}S$) in a way that the maximum amount of work is obtainable from a closed thermodynamic system at a constant temperature and pressure.

The thermodynamic properties as shown in Eq. 1.11 are plotted for the dissociation of water (Eq. 1.1) as function of temperature in **Figure 2.1** and **Figure 2.6**. These figures are frequently used to argue the motivation for high-temperature electrolysis versus low-temperature electrolysis. Especially, Fig. 2.6 shows that the change of Gibbs free energy ΔG_r decreases with raising temperature whereas the product of temperature and the change of entropy $T\Delta S_r$ increases. It means that in case of a reversible reaction, the requirement of electrical work W_{rev} decreases with temperature. The total energy demand ΔH_r required for the electrolysis can be supplied by a combination of electrical energy and heat which is indicated by the $T\Delta S_r$ term.

1.3 Fundamentals of electrolysis

The water electrolysis is distinguished from the fact that water is separated continuously into the molecules of hydrogen and oxygen in a single process. For this purpose, two electrodes are required which are separated by an electrolyte (liquid or solid) to enhance the ionic conductivity. Furthermore, the electrolyte, *i.e.*, diaphragm, avoids the recombination of the species (*e.g.* hydrogen and oxygen). One electrode is called *cathode*, where the *reduction* takes place and the second one is the *anode*, where the oxidation takes place. The basic components, consisting of a cathode, an anode and an electrolyte configure an electrolysis cell. The overall reaction for electrochemical water-splitting is given by

$$\mathrm{H_2O} + electrical\ energy + heat \rightarrow \mathrm{H_2} + \tfrac{1}{2}\mathrm{O_2}. \tag{1.12}$$

The water electrolysis can be distinguished between three different technologies:

- alkaline electrolysis; using an aqueous electrolyte solution,
- electrolysis with an acid polymer (ionomer) electrolyte for proton exchange (PEM), and

- high-temperature electrolysis; using a solid oxide electrolyte for oxygen ion conduction (SOEC)

A general overview of water electrolysis is given in [1,2,3,4,5]. Beside high-temperature water electrolysis, *solid oxide electrolysis cells* (SOEC) are also capable of dissociation carbon dioxide (CO_2) to carbon monoxide (CO) and oxygen because of their chemical stability against CO poisoning. An overview of steam/CO_2 co-electrolysis for the production of syngas is given in [6,7,8]. The overall reaction of CO_2 electrolysis is expressed as

$$CO_2 + electrical\ energy + heat \rightarrow CO + \tfrac{1}{2}O_2. \tag{1.13}$$

The relationship between enthalpy change of reaction (ΔH_r), Gibbs' free energy of reaction (ΔG_r) and the entropy term of reaction ($T\Delta S_r$) is determined by the first and second law of thermodynamics, as already shown in Eq. 1.11. The total energy demand, *i.e.* electrical energy and heat, for the electrolysis process is calculated from this relationship. In **Figure 2.8**, the energy demand and temperature dependency of high temperature electrolysis of H_2O and CO_2 is shown.

The electrochemical water-splitting process (according Eq. 1.12) is an endothermic ($\Delta H_r > 0$) and non-spontaneous, *i.e.* endergonic ($\Delta G_r > 0$) chemical reaction. From a thermodynamic point of view, the Gibbs' free energy change of reaction represents the minimum cell voltage V_{rev}, *i.e.* the reversible cell voltage, required for the electrolysis reaction, and is given as:

$$V_{rev} = \frac{\Delta G_{rev}}{zF}, \tag{1.14}$$

where z is the number of electrons per mole of product turnover and F is the Faraday constant (96485 C mol^{-1}).

Commercial electrolysis systems can be operated in three different operation modes: **thermoneutral**, **endothermal** and **exothermal**. These modes will be explained later on in chapter 2.3. At this point, it is necessary to anticipate that, if the thermal energy $T\Delta S_r$ is provided by electrical energy, due to internal losses (*i.e.* irreversibilities), the required voltage for the electrolysis is known as thermoneutral voltage (V_{tn})

$$V_{tn} = \frac{\Delta H_r}{zF}. \tag{1.15}$$

At standard conditions (T = 198,15 K, p = 1 bar), the reversible and thermoneutral voltage for the electrochemical water-splitting reaction is V_r^0 = 1.299 V (corresponding to ΔG_r^0 = 237.141 kJ mol^{-1} H_2 [9]) and V_{tn}^0 = 1.481 V (corresponding to ΔH_r^0 = 285.830 kJ mol^{-1} H_2[9]).

In real application of an operating electrolysis cell, the voltage is significantly higher than the theoretical reversible cell voltage derived from the FIRST and SECOND

law of thermodynamics. In addition to the theoretical reversible cell voltage V_{rev}, the real cell voltage V_{cell} can certainly be seen as a sum of several contributions of overvoltages that appear in an operating electrolysis cell:

$$V_{cell} = V_{rev} + \eta_{\Omega} + \eta_{\mathrm{ct}} + \eta_{\mathrm{con}}. \tag{1.16}$$

In Eq. 1.16 the term η_{Ω} represents the ohmic overvoltage, is caused by resistance of cell elements (electrodes, current collectors, *etc*.) as well ionic flow in the electrolyte. η_{Ω} is basically proportional to the electrical current. The term η_{ct} implies the overvoltage required to overcome the charge transfer between the electrodes. The term η_{con} is known as concentration overvoltage, and caused by the mass transport of the chemical species for diffusion and convection.

The reduction of overvoltage is of crucial importance. The correlation between current and voltage is formulized by *I-V* characteristic. Furthermore, the *I-V* characteristic curve provides an adequate investigation method for identifying the different kinds of overvoltages. Finally, detailed results will be derived from BUTLER-VOLMER and TAFEL plots. An important performance parameter that quantifies the ohmic loss associated with the operation of electrolysis cells is the *area-specific resistance* (ASR). This correlation is defined as:

$$ASR = \frac{V_{cell} - V_{rev}^{0}}{i};\ i = \frac{I}{A_{cell}}, \tag{1.17}$$

where V_{cell} is the applied potential, V_{rev}^{0} is the reference or the reversible cell potential and i is the current density (A cm^{-2}).

Until now, only a single cell has been considered. A commercial electrolysis system is composed of many single cells to an electrolysis *stack*. The voltage of such an electrolysis stack is determined by:

$$V_{stack} = N_{\mathrm{cells}} V_{cell}, \tag{1.18}$$

where N_{cells} is the number of electrolysis cells in the stack. The various cell units are electrically connected in series.

The electrolysis efficiency, η_{EC}, can be defined analogous to the definition of fuel cell efficiency [10]. The electrolysis efficiency can be expressed strictly as a ratio of the cell voltages as follows:

$$\eta_{EC} = \frac{\Delta H_r / zF}{V_{cell}} = \frac{V_{tn}}{V_{cell}}. \tag{1.19}$$

The total efficiency of the electrolysis cell (η_{cell}) or of the stack (η_{stack}) is the product of the voltage efficiency (η_{EC}) and the current efficiency. The definition of the current efficiency for a gaseous product j is also known as Faraday efficiency $\eta_{EC,F}$ and is defined as

$$\eta_{EC,F} = \frac{zFx_j f_m}{I}, \tag{1.20}$$

where F is the Faraday constant (96485 C mol^{-1}), z is the number of electrons per mole of product turnover, x_j is the mole fraction of the considered species j in the gaseous mixture, f_m is the molar flow rate, and I is the total electrical current. The molar flow rate f_m is calculated by using of the IDEAL GAS Law, given as:

$$f_m = \frac{p\, f_V}{R_m\, T}, \tag{1.21}$$

where f_V represents the volume rate generated due to the electrochemical reaction and R_m is the molar gas constant for ideal gases (8.414 J (mol K)$^{-1}$).

2 STATE OF KNOWLEDGE

The radiation energy of the sun reaching the surface of the earth is many times greater than the global energy demand. The solar energy source is more or less unlimited and the utilization is ecologically friendly. Inspired by this idea, many different approaches and methods have been developed. Some of these concepts especially by following a (solar-)thermo-, electro-, photochemical approach will be discussed.

2.1 Overview

A brief numerical value example shown by A. STEINFELD and A. MEIER pointed that only 0.1% of the earth's land space with solar collectors that operate with a collection efficiency of merely 20% would generate enough energy to supply the current yearly energy needs of all inhabitants of the planet (~$1.2 \cdot 10^{14}$ kWh) [11]. Indeed, the current value of the annual energy demand has been changed slightly because that cited value is derived from the year 2004. In 2012, the IEA (International Energy Agency) estimated that the world energy consumption was $1.555 \cdot 10^{14}$ kWh [12].

Furthermore, the solar energy source is more or less unlimited and the utilization is ecologically benign. However, solar radiation is dilute so that only~1kW/m^2 is intermittent available during daytime and under clear-sky conditions at earth's surface. This fact will make a broad application of solar energy uncomfortable. These drawbacks can be overcome by concentrating the solar radiation to achieve much higher concentration ratios, (*i.e.* radiation intensities) than 1 sun. Furthermore, converting solar energy into chemical energy carriers, *i.e. solar fuels* [13,14,15,16,17] provide the basis for *energy on demand*. Solar fuels can be stored long term and transported long range, *e.g.* from sunny and desert regions to industrialized and populated centers of the earth, where much of energy is required. Solar fuels can also be burned to generate heat and converted into electrical or mechanical work, or for direct use in fuel cells to generate electricity are being complied with customers' energy demands. In addition to that, solar heat is also used in several processes *e.g.* in heat pumps, cooling and drying processes to avoid greenhouse gas emissions and other pollutants derived from the combustion of fossil fuels for heat and electricity generation.

The focus of this work lies on converting of (solar) radiation energy into chemical energy. From a **thermodynamic point of view** it has to be noted that it is **not possible to transform the whole portion of solar radiation into chemical energy**. In the following, several routs for producing solar fuels from solar energy are highlighted:

- ***Solar thermochemical path:*** concentrated solar radiation is used to drive a thermochemical process. The thermochemical water-splitting reaction followed by a discontinuous process, *i.e.* more than one temperature level is necessary. Such *two* or *more step* water-splitting processes [18] need a *endothermic* step for reactivating the material system up to 2000°C and an *exothermic* step at a low temperature level within hydrogen is produced by oxidizing the material system.

- ***Solar electrochemical path:*** renewable generated electricity from photovoltaic or solar thermal systems followed by an electrolytic process. Electrochemical processes can be performed in a low temperature regime, *i.e*. by means of a PEM[1] electrolysis cell, and in a high temperature regime, *i.e*. by means of a SOEC[2] [19]. In a continuous process water is split into oxygen O_2 and hydrogen H_2.
- ***Solar photochemical path:*** direct use of the photon energy to drive a photoelectrochemical reaction. Several methods from the scientific literature are known in which the principle of photo(electro-)chemical energy conversion is used. Basically, two methods should be mentioned. Firstly, the **biomimetic** approach in which the mechanism of photosynthesis is emulated from nature [20] and, secondly, the **photoelectrochemical water-splitting in aqueous environment** using *n*-type TiO_2. This research activities are going back to the early 1970s and were firstly demonstrated by A. FUJISHIMA und K. HONDA (*Ref*. [21]).

A completely new approach for **high-temperature photoelectrochemical energy conversion** was found by the author of this PhD thesis. This method will be explained in detail further on in this thesis.

2.2 Solar thermochemical path

Energy conversion by solar-driven production of hydrogen from water was evaluated that thermochemical cycles are thermodynamically efficient and ecological benign [22]. Since 1970s, first studies on *single-step* (direct) thermal water dissociation have been published by E.A. FLETCHER and R. L. MOEN (*Ref*. [23]) and S. IHARA (*Ref*. [24]).

Even tough conceptual convenience of the method a relevant restraint is ensured by a lack of an effective technique for separating of hydrogen (H_2) and oxygen (O_2) at high temperatures [25]. That drawback has been overcome by performing of *two-step* water-splitting cycles, based on redox material systems. Regarding this research field a substantial scientific community has been established, so that a large spectrum of scientific literature is available.

---

[1]Abbreviation: PEM – *Proton Exchange Membrane* is a special kind of polymeric material for proton (H^+) conduction to separate to reduction and oxidation zone in an electrochemical cell for operating temperature between 80-200°C.

[2]Abbreviation: SOEC – *Solid Oxide Electrolysis Cell* uses a solid oxide electrolyte material for oxygen ion (O^{2-}) conduction which is highly temperature-resistant up to approx. 1000°C.

2.2.1 Direct thermal dissociation of water

Solar driven water-splitting processes represent an attractive method to produce hydrogen in a renewable way. In a single step, water is thermally dissociated at a temperature of ~ 4300 K, shown in Fig. 2.1.

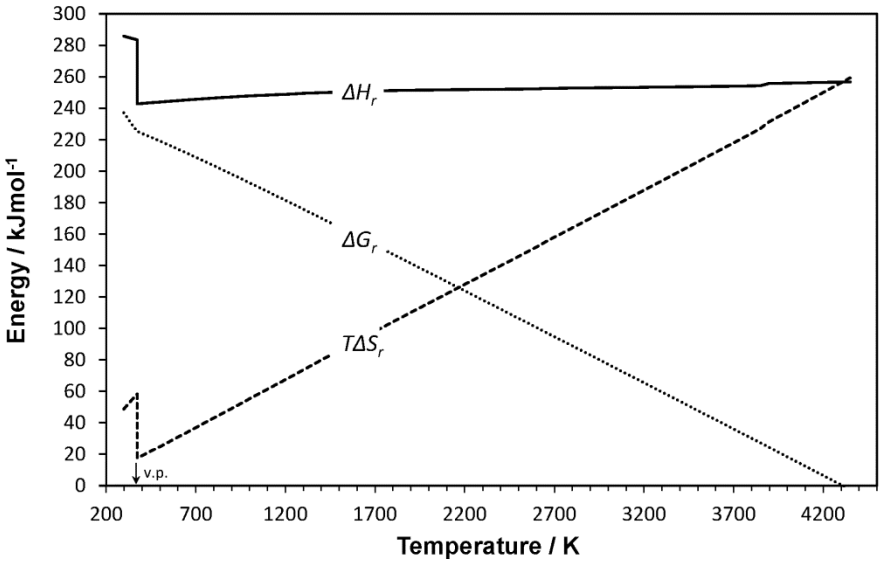

Figure 2.1: Energy requirements for thermal dissociation of water into hydrogen (H_2) and oxygen (O_2) at 1 bar. Calculated from thermochemical data by using *FactSage 6.1* [26].

The temperature required for the thermochemical dissociation is rather high (see Fig. 2.1). Some details in the diagram above should be explained. The trend of each *thermodynamic potential* expressed by

$$G(p,T) = H - TS, \tag{2.1}$$

is shown for the dissociation of water (see Fig. 2.1) in dependence of temperature and at a constant pressure of 1 bar. First, the discontinuity (v.p.) in Fig. 2.1 marks a phase change where water begins to vaporize. In the following the *enthalpy of reaction* (ΔH_r) remains rather constant over a large temperature range. Whereas the *Gibbs free energy* (ΔG_r) decreases and the term ($T\Delta S_r$) increases with temperature. Secondly, not before when ΔG_r is zero, *i.e.* ΔH_r is equal to $T\Delta S_r$, water begins dissociating in H_2 and O_2, but there is no separation of these species (H_2, O_2). In regard to the high temperature, the drawbacks are primarily related to engineering- and material specific aspects. Therefore, different methods have been developed for this purpose up to now. To avoid a recombination of H_2 and O_2 in a thermochemical process a sufficient separation of the products is necessary. This can be achieved by introducing a redox material system, *i.e.* extending from single-step to two- or more-step water-splitting processes. For instance, by using a Zn/ZnO material system the water-splitting

process takes place in two steps: production of hydrogen by oxidizing of zinc to zinc oxide and releasing of oxygen by reduction of zinc oxide back to zinc.

An essential advantage for the introduction of a material system (*e.g.* Zn/ZnO) is that a lower temperature level is required for the thermal dissociation step. In opposite to the very-high temperature single-step process, where the thermal water dissociation takes place (see Fig. 2.1).

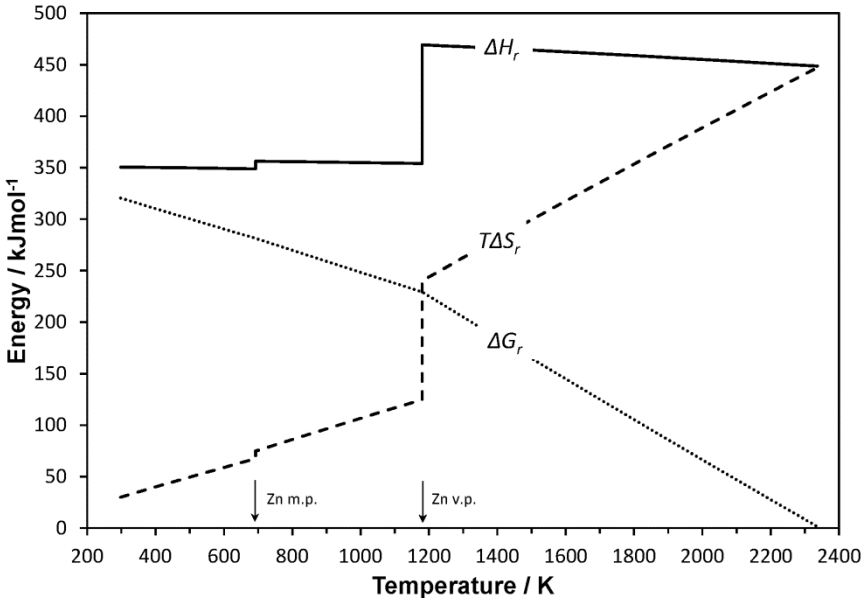

Figure 2.2: Energy requirements for thermal dissociation ZnO(s)⟶Zn + ½ O_2 at 1 bar. Calculated from thermochemical data by using *FactSage 6.1* [26].

The thermal dissociation of solid zinc oxide ZnO*(s)* in zinc takes place around 2300 K, shown in **Figure 2.2.** During the reduction process of ZnO(s) → Zn + ½ O_2 the material is exposed two phase changes. The first (v.p.) at 1180 K from gaseous to liquid state and the second (m.p.) from liquid to solid state. It can be imagine that such process with two phase changes is from an engineering point of view not trivial to handle, because sufficient gas tightness must be guaranteed. A large number of alternative redox cycles have been investigated.

2.2.2 Two-step water-splitting cycles

Several hydrogen production processes via two- and multi-step water-splitting have been summarized by S. ABANADES et *al*. (*Ref*. [18]). Generally, thermochemical cycles require two steps at least and for that reason two temperature levels have to be run-up sequentially. The first step is a *solar-driven* dissociation of the reactants (MeO_{x-1}) within the material is regenerated and oxygen is released (Eq. 2.2). The oxidation is a *non-solar step* in which water is consumed and hydrogen is released (Eq. 2.3). In this

reaction a reactive material oxidizes to the general form MeO_x. Such cycles based on redox-systems, for instance Zn/ZnO [27], FeO/Fe_3O_4 [28,29], CeO_2/Ce_2O_3 [30,31] have been thermodynamically examined and tested in solar reactors. The dissociation and the oxidation step is given by

1st step (solar): $$Me0_x \rightarrow Me0_{x-1} + \tfrac{1}{2}0_2, \quad (2.2)$$

2nd step (non-solar): $$Me0_{x-1} + H_20 \rightarrow Me0_x + H_2. \quad (2.3)$$

The solar thermochemical production of hydrogen and oxygen takes place in a discontinuous water-splitting process. A model flow diagram for a two-step solar thermochemical cycle is shown schematically in **Figure 2.3**.

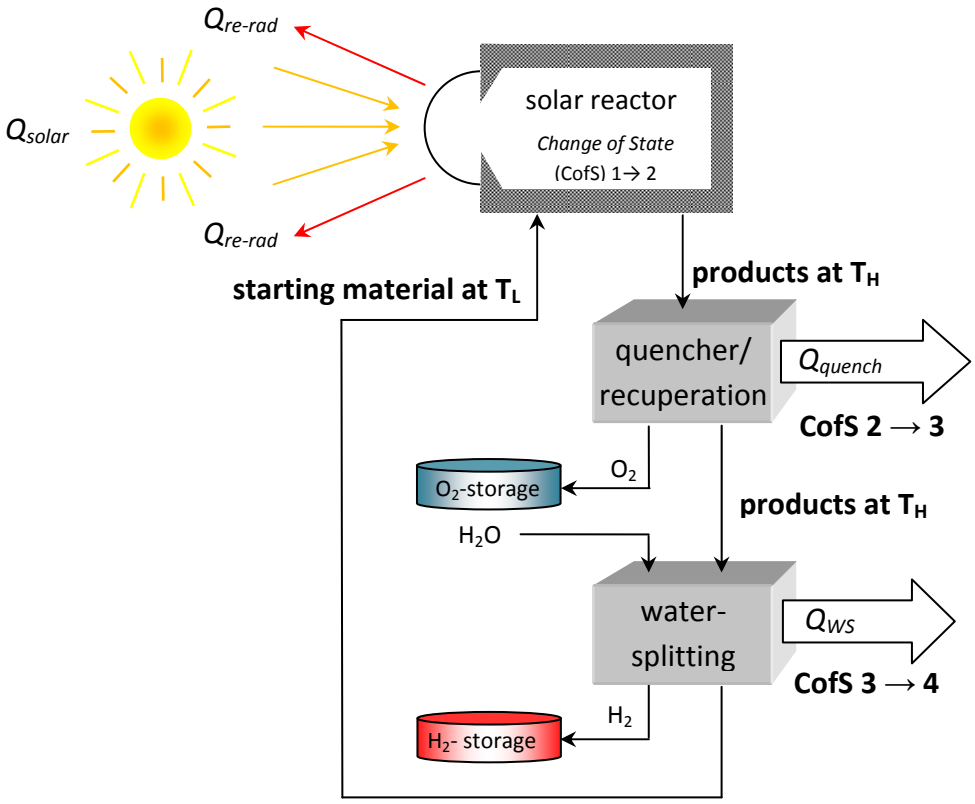

Figure 2.3: Process diagram for regeneration (O_2-releasing) of the reactive material at a high temperature level T_H and an oxidation (H_2-production) at a lower temperature T_L performed by several *change of states* (CofS); Own graphic, adapted from *Ref.* [11].

It uses a **solar reactor**, a **quenching unit** and a **hydrolyser reactor**. An optimal process is working at a constant pressure but in real pressure drops will occur due to frictional forces. For an exergy analysis it is assumed that the solar reactor is a cavity receiver, operating at 2300 K. The absorption efficiency $\eta_{absorption}$ is defined as the net rate at which energy $Q_{reactor,net}$ is being absorbed, divided by the solar energy input entering the solar receiver's aperture Q_{solar}. For simplification, the cavity-receiver is

defined to be a perfectly insulated blackbody. There is no convection or conduction heat losses, only radiation losses through the aperture are considered, *i.e.* cavity's effective absorptivity α_{eff} and emissivity ε_{eff} are equal to 1. The relation is given by E. A. FLETCHER and R. L. MOEN (*Ref.* [23]):

$$\eta_{absorption} = \frac{Q_{reactor,net}}{Q_{solar}} = \left(1 - \frac{\sigma T^4}{I_S C}\right), \tag{2.4}$$

where I_S is the normal beam insulation and is considered to be in kW/m², C is defined as solar concentration ratio of the concentrating system [32,33], T_H is the nominal reactor temperature; for the following exergy analysis it is assumed to be 2300 K and σ is the Stefan-Boltzmann constant.

Irreversibilities in the solar thermochmical reactor arise from non-reversible chemical reaction and reradiation losses to the ambient temperature T_L, given by A. STEINFELD (*Ref.* [27]); exemplary for the solar reactor:

$$\dot{S}_{irr\,reactor} = \left(\frac{-\dot{Q}_{solar}}{T_H}\right) + \left(\frac{\dot{Q}_{reradiation}}{T_L}\right) + \dot{n}\Delta S_r|_{educts(T_L),p \rightarrow products(T_H),p}, \tag{2.5}$$

where $Q_{reradiation}$ indicates the radiation heat loss by the reactor $Q_{reradiation} = (1 - \eta_{absorption})/Q_{solar}$. Irreversibilities also occur during the quenching process and the hydrolysis (water-splitting) reaction. The educts (reactants) are being introduced into the solar reactor at ambient temperature (298 K) and are heated to reactor temperature at 2300 K. The solar reactor is fed with a rate $\dot{n}$ of 1 mol/s. For the calculation chemical equilibrium has been assumed. For the complete thermochemical process it was supposed that it is carried out at a constant pressure p of 1 bar. The net power $\dot{Q}_{reactor,net}$ absorbed by the solar rector has to provide the enthalpy change of the endothermic reaction:

$$\dot{Q}_{reactor,net} = \dot{n}\,\Delta H_r|_{educts(T_1),p \rightarrow products(T_2),p}. \tag{2.6}$$

During the quenching process and cooling to reach the low temperature level for the water-splitting process thermal power is lost:

$$\dot{Q}_{quench} = -\dot{n}\,\Delta H|_{products(T_2),p \rightarrow products(T_3),p}. \tag{2.7}$$

The mass flow rate $\dot{n}$ of water to the hydrolyser is also set to 1 mol/s. The exothermic reaction is given by:

$$\dot{Q}_{hydrolyser} = -\dot{n}\,\Delta H_r|_{educts(298K),p \rightarrow products(298K),p}. \tag{2.8}$$

From a thermodynamic point of view it is interesting to know how efficient an energy conversion process is working. Even in this case, the exergy analysis provides a result of an amount of solar radiation energy for those is being converted into *work* via a heat engine. More efficiently would be a *fuel cell* to generate electric work directly. The theoretical maximum available work that could be received from the

reaction of hydrogen and oxygen is calculated by introducing a *reversible* fuel cell. The products of the two-step water-splitting process (H_2/O_2) recombine to water (H_2O) and electrical power is generated. The work output W_{FC} of the fuel cell is given by:

$$\dot{W}_{FC} = -\eta_{FC}\, \dot{n}\, \Delta G_r|_{H_2+\frac{1}{2}O_2(298\,K),1\,bar \rightarrow H_2O(298\,K),1\,bar}\,. \tag{2.9}$$

In an isothermal operating ideal fuel cell with a supposed efficiency η_{FC} of 100% also heat Q_{FC} is rejected to the ambient:

$$\dot{Q}_{FC} = -\,T\,\dot{n}\,\Delta S_r|_{H_2+\frac{1}{2}O_2(298\,K),1\,bar \rightarrow H_2O(298\,K),1\,bar}\,. \tag{2.10}$$

Finally, the exergy efficiency η_{exergy} is defined as the amount of solar energy Q_{solar} converted into chemical energy given by the Gibbs free energy change of the reaction ΔG_r. Therefore, η_{exergy} is the ratio of the fuel cell's work output to the solar power input:

$$\eta_{exergy} = \frac{W_{FC}}{Q_{solar}}\,. \tag{2.11}$$

Several thermochemical two-step water-splitting processes haven been studied in detail. In the following, the thermodynamic data of three different cycles are shown.

Zn/ZnO – redox system [27]:

energy balance	Concentration ratio C= 5,000		Concentration ratio C= 10,000
$\dot{Q}_{solar}$	815 kW		662 kW
$\dot{Q}_{reradiation}$	258 kW		105 kW
$\dot{Q}_{reactor,netto}$		557 kW	
$\dot{S}_{irr_{reactor}}$		0.81 kW K^{-1}	
$\dot{Q}_{quench}$		209 kW	
$\dot{S}_{irr_{quench}}$		0.52 kW K^{-1}	
$\dot{Q}_{hydrolyser}$		64 kW	
$\dot{S}_{irr_{hydrolyser}}$		0.27 kW K^{-1}	
$\dot{Q}_{FC}$		49 kW	
$\dot{W}_{FC}$		237 kW	
$\eta_{absorption}$	68%		84%
η_{exergy}	29%		36%
$\eta_{exergy}(\eta_{FC} = 0.7)$	20%		25%

Table 2.1: Exergy analysis of two-step water-splitting thermochemical cycle using Zn/ZnO material system. ZnO and H_2O molar flow rates are set to 1 mol/s.

FeO/Fe_3O_4 – redox system [28]:

energy balance	Concentration ratio *C*= 5,000		Concentration ratio *C*= 10,000
$\dot{Q}_{solar}$	1148.6 kW		932.2 kW
$\dot{Q}_{reradiation}$	364.6 kW		148.2 kW
$\dot{Q}_{reactor,netto}$		784.0 kW	
$\dot{Q}_{quench}$		478.3 kW	
$\dot{Q}_{hydrolyser}$		18.0 kW	
$\dot{Q}_{FC}$		53.8 kW	
$\dot{W}_{FC}$		233.9 kW	
$\eta_{absorption}$	68.3%		84.1%
η_{exergy}	20.4%		25.1%

Table 2.2: Exergy analysis of two-step water-splitting thermochemical cycle using FeO/Fe_3O_4 material system. Fe_3O_4 and H_2O molar flow rates are set to 1 mol/s.

Ce_2O_3/CeO_2 – redox system [30]:

energy balance	Concentration ratio *C*= 5,000		Concentration ratio *C*= 10,000
$\dot{Q}_{solar}$	1056 kW		-
$\dot{Q}_{reradiation}$	335 kW		-
$\dot{Q}_{reactor,netto}$		721 kJ mol^{-1}	
$\dot{Q}_{quench}$		-	
$\dot{Q}_{hydrolyser}$		-127 kJ mol^{-1}	
$\dot{Q}_{FC}$		-49 kJ mol^{-1}	
$\dot{W}_{FC}$		237kJ mol^{-1}	
$\eta_{absorption}$	68%		-
η_{exergy}	22%		-

Table 2.3: Exergy analysis of two-step water-splitting thermochemical cycle using Ce_2O_3/CeO_2 material system. The molar flow rates of CeO_2 is set to 2 mol/s and H_2O is set to 1 mol/s.

In the exergy analysis for the Zn/ZnO – redox system (**Table 2.1**) and for the FeO/Fe_3O_4 – redox system (**Table 2.2**) both solar concentration ratios (5,000 and 10,000) have being considered. For the Ce_2O_3/CeO_2 – redox system (**Table 2.3**) the thermodynamic data are only shown for a solar concentration ratio of *C*= 5,000. The

exergy efficiency for a concentration ratio of 5,000 is around 20% for all cycles. By increasing the solar concentration ratio up to 10,000 (see **Table 2.1** and **Table 2.2**) the exergy efficiency is slightly rising to 25%.

There have been investigated many other material systems to overcome some technological drawbacks. For instance; a decrease of the process temperature will avoid thermal losses and new reactive composite material systems will prevent sintering of the powder. Promising materials are mixed oxides of the type $(Fe_{1-x}M_x)_3O_4$ that shall be reducible at lower temperatures than the redox-systems which were mentioned before. The reduced phase $(Fe_{1-x}M_x)_{1-y}O$ is able to split water [34,35]. For getting a higher thermal stability of the redox-system (*e.g.* avoiding sintering) a mixture of yttria stabilized zirconia (YSZ) and a reactive material like $NiFe_2O_4$ helps to proceed the water-splitting without the treatment (crushing the reduced phase) [36]. In other approaches solid structures, *i.e.* honeycomb structures, were used to fix the reactive material [35].

The maximum achievable efficiencies $\eta_{TC,max}$ of all thermochmical processes can be related to Carnot efficiency, *i.e.* engines are operating between an upper and lower temperature level (T_H, T_L), see **Figure 2.4**.

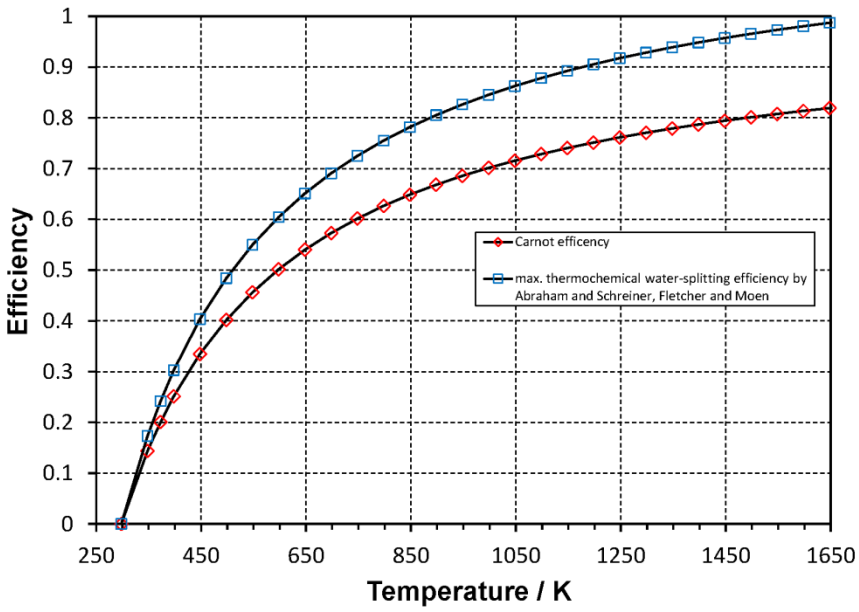

Figure 2.4: Theoretical thermochemical water-splitting efficiency compared to Carnot efficiency.

This fundamental result was derived for thermochemical cycles by B. M. ABRAHAM and F. SCHREINER (*Ref.* [37]), and applied to solar thermal dissociation of water by E.A. FLETCHER and R. L. MOEN (*Ref.* [23]). Here, it has to be taken into consideration that, conceptually, a reversible fuel cell which converts hydrogen and oxygen to

(liquid) water at a lower temperature level. Such that the efficiency expression can be written as:

$$\eta_{TC,max} = \left(1 - \frac{T_L}{T_H}\right)\left(\frac{HHV}{-\Delta G^0_{f,H_2O}}\right), \tag{2.12}$$

where *HHV* is the "high heating value" of hydrogen and $-\Delta G^0_{f,H_2O}$ the standard-state Gibbs energy of formation for water.

2.3 High-temperature electrolysis

Another method for the hydrogen production is the high temperature steam electrolysis (*HTE*). In general, the water electrolysis for the production of hydrogen (at low- and high-temperature) is a well proven technology. In opposite to two-step thermochemical water-splitting, hydrogen and oxygen is produced continuously. The HTE technology requires less electrical energy consumption compared to conventional low temperature electrolysis, as a consequence of the more favorable thermodynamic and kinetic conditions for the reaction.

Furthermore, this process allows the conversion of electrical energy in addition with thermal energy into chemical energy (*e.g.* hydrogen). Experimental investigation shows that the molar Gibbs energy (ΔG_r) drops from ~ 1.23 eV (237 kJ mol^{-1}) at ambient temperature to ~ 0.95 eV at 900°C (183 kJ mol^{-1}) [9], while the molar enthalpy of the reaction (ΔH_r) remains unchanged (ΔHr ~ 1.3 eV or 249 kJ mol^{-1} at 900°C) [9]. Thus, a significant part for the energy requirement to drive a beneficial HTE process, *i.e.* low-loss operating mode, can be provided by heat. A HTE process uses a solid oxide electrolysis cell (*SOEC*) to drive an electrothermochmical water-splitting reaction and is given by

$$H_2O + 2e^- \rightarrow H_2 + O^{2-}, \tag{2.13}$$

$$O^{2-} \rightarrow \tfrac{1}{2}O_2 + 2e^-, \tag{2.14}$$

whereas in reaction (2.13) the electrochemical reduction supported by thermal energy takes place. According to that process hydrogen and oxygen ions are produced. Oxygen ions will pass through a thermal resistant solid oxide membrane to the anode and molecular oxygen will be released (2.14). The overall reaction is the water-splitting reaction according to Eq. 2.15.

$$H_2O \rightarrow H_2 + \tfrac{1}{2}O_2\,. \tag{2.15}$$

A scheme of a SOEC as well as the reactions at the cathode (reduction) and the anode (oxidation) are schematically indicated in **Figure 2.5**.

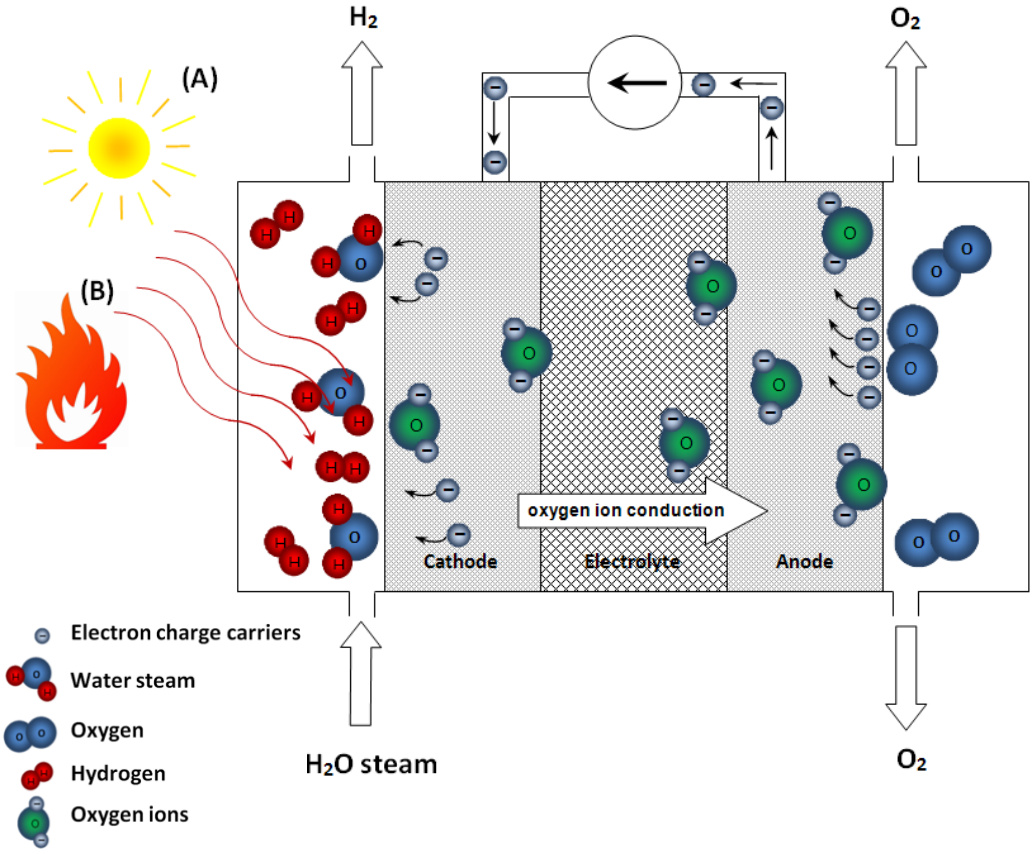

Figure 2.5: Scheme of a solid oxide electrochemical cell (SOEC) for high-temperature electrochemical water-splitting.

Such a high-temperature electrolysis cell is driven by an external DC power supply. The thermally assisted electrochemical water-splitting reaction according to Eq. 2.13 takes place at the cathode. Oxygen ions (O^{2-}) are pumped from the cathode (*e.g.* Ni/YSZ cermet) through the solid oxide electrolyte (*e.g.* yttrium-stabilized zirconia (YSZ)) to the anode (*e.g.*$La_{1-x}Sr_xMnO_3$/YSZ) where O^{2-}ions are discharged by giving up electrons to the electrical circuit (see Eq. 2.14).

In principle, a SOEC can be operated in three different ways: *thermoneutral*, *endothermal* and *exothermal*.

Thermoneutral mode. The SOEC operates at thermal equilibrium. In this mode the electrical input is equal to the enthalpy of reaction. This is the case when the water steam inlet temperature is equal to the gas outlet temperature. The electrochemical conversion, *i.e.* electrical-to-hydrogen efficiency, is 100%. This implies that the same amount of entropy needed for water-splitting must be equal to the generated heat due to internal irreversibility (reaction losses).

Exothermal mode. In this mode the electric energy input exceeds the enthalpy of reaction, leading to an electrical efficiency below 100%. The generated heat from the electrochemical cell can be reused in the HTE process to preheat the inlet gas flows.

Endothermal mode. The electrical energy input lies below the enthalpy of reaction which means a cell voltage below the thermoneutral case (< 1.3 V at 900°C). For this operation mode heat must be supplied to the process to maintain the temperature. The required heat for the thermo electrochemical process can be contributed by industrial exhaust heat (B) or renewable heat sources, such as solar heat (A); it is schematically illustrated in Fig. 2.5. This high temperature heat could be also provided by conventional sources, for instance from a nuclear reactor and has been thermodynamically considered in few scientific works [38,39]. By driving an endothermal operation mode electrical-to-hydrogen efficiencies achieve more than 100%.

With a commercial SOEC a current density of 1.4 Acm^{-2} with only 1.1 V at 900°C was archived to demonstrate water-splitting at high-temperatures [19]. For instance, this voltage is largely below in comparison with alkaline electrolysis. Another advantage of high-temperature electrolysis by a SOEC is the reduction of electrode *overpotentials* which lead to power losses in the electrolysis cell [40,4].

The advantage of performing high temperature electrolysis is demonstrated by the relationship between total energy demand (ΔH_r), electrical energy demand (ΔG_r) and thermal energy demand ($T\Delta S_r$) as shown in Fig. 2.6.

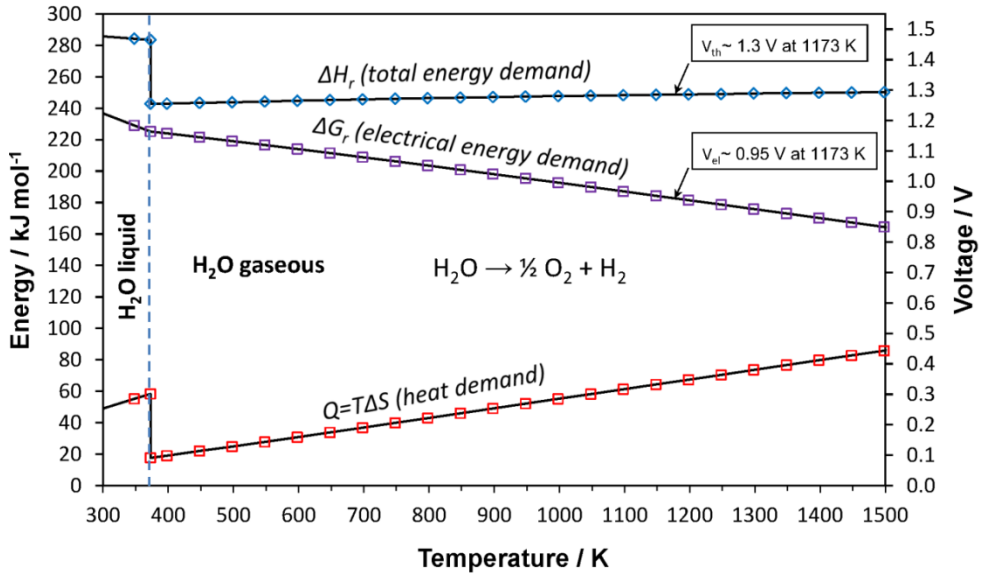

Figure 2.6: Energy demand of high temperature electrolysis demonstrating the advantage of lowered electrical energy demand at high temperatures; calculated from thermochemical data by using *FactSage* 6.1 [26].

The demand of electrical energy ΔG_r decreases significantly with raising temperature, whereas the demand of thermal energy $T\Delta S$ for the thermo-electrolysis increases and the total energy demand ΔH_r rises rather slightly. According to favorable thermodynamics and faster electrode kinetics an operation at high temperatures leads to minimization of internal device losses.

The efficiency of an electrolysis cell, defined as:

$$\eta_{EC} = \frac{LHV}{W} = \frac{V_{tn}}{V_{cell}} \tag{2.16}$$

is increasing when the cell voltage (operating voltage) V_{cell} of the electrolyzer is kept low. LHV is the *lower heating value* of the produced fuel and W is the total electrical energy input. Generally, LHV is defined as the enthalpy change of reaction ΔH_r for *e.g.* water-splitting reaction. The efficiency is 100% if the electrolysis cell is operating at *thermoneutral voltage* V_{th} (or enhalpy voltage). In that case there is no net heat flux through the SOEC, *i.e.* temperature of inlet is equal to outlet gas flow.

In comparison to low temperature alkaline electrolyzers as well as PEM based electrolyzers, SOEC has advantages in efficiency and insensitivity against poisoning, as well as the ability to produce synthesis gas in a direct way (CO_2 reduction is shown in Fig. 2.8.). A comparison of three electrolysis technologies is shown in **Figure 2.7**.

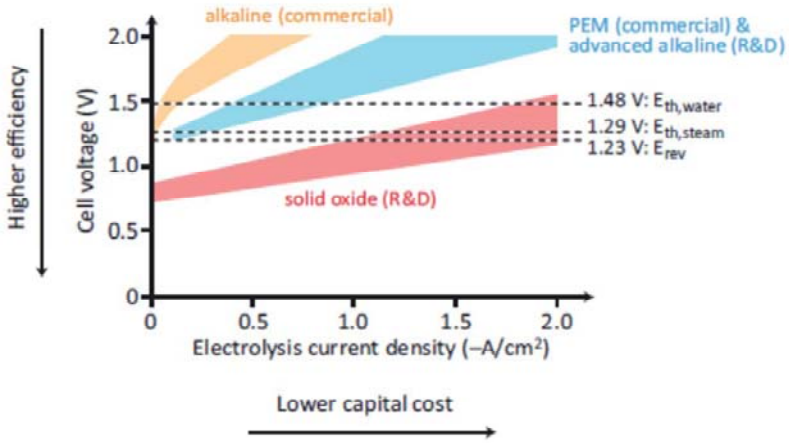

Figure 2.7: Typical polarization curves for state of the art electrolyzer technologies [41].

The electrochemical energy conversion using a high-temperature electrolysis system provides a promising method to produce alternative liquid fuels derived from low-emission energy sources. This is crucial for reaching the desired ambition to meet the demand in the transportation sector. For that reason, the electricity-to-fuel conversion is inevitable for a future energy system. In particular, the high-temperature steam/CO_2 co-electrolysis is an appropriate method to split water and CO_2 directly to syngas (H_2+CO). The principle of a SOEC for electrochemical water-

splitting (Eq. 2.13–Eq. 2.15) was schematically shown in Fig. 2.5. Beside the presented approach using a steam/CO_2 co-electrolysis; CO_2 splitting has been also demonstrated by using a hybrid system. In this approach, a high-temperature carbonate electrolysis (operating at 750-950°C) is driven by a concentrator PV system [42]. By extension in terms of steam/CO_2 co-electrolysis, the system of reaction equation is given as follows:

$$H_2O + 2e^- \rightarrow H_2 + O^{2-}, \tag{2.17}$$

and

$$CO_2 + 2e^- \rightarrow CO + O^{2-}. \tag{2.18}$$

At the anode, oxygen ions are oxidized to gaseous oxygen:

$$O^{2-} \rightarrow \tfrac{1}{2}O_2 + 2e^-. \tag{2.19}$$

Besides the electrochemical reactions (Eq. 2.17–Eq. 2.19) at both electrodes, also other chemical reactions may even take place in parallel. The most important one is the reverse water-gas shift (RWGS) reaction, as given:

$$CO_2 + H_2 \leftrightarrow CO + H_2O\,. \tag{2.20}$$

The RWGS reaction is a heterogeneous catalytic reaction and preferred takes place in presence of a solid catalyst such as Ni in the Ni/YSZ electrode. At high temperatures it is a kinetically fast, equilibrium reaction. In fact, it has been considered [8] that most CO_2-to-COconversion under steam/CO_2 co-electrolysis conditions could be realized through the RWGS reaction instead of the electrochemical CO_2-reduction reaction Eq. 2.18. The energy demand for steam/CO_2 co-electrolysis as function of temperature is shown in Fig. 2.8. The corresponding cell voltage in order to supply a certain amount of energy is also indicated by the right axes in the diagram.

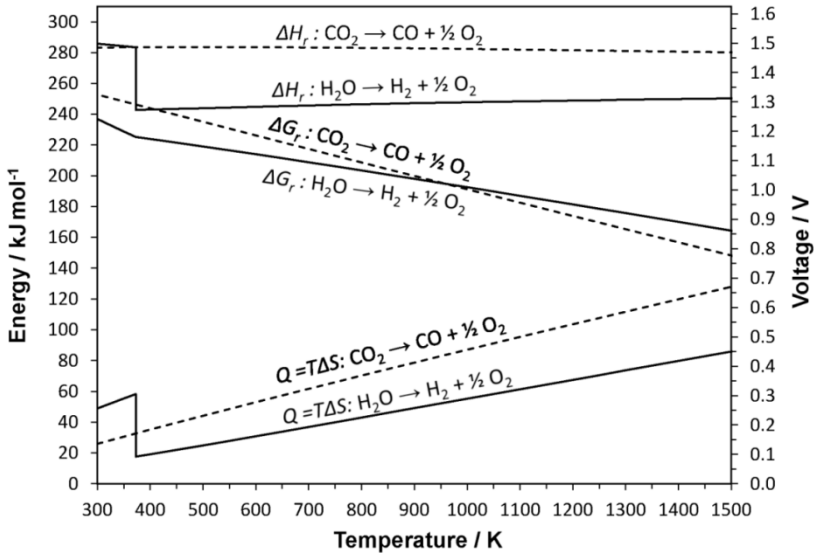

Figure 2.8: Energy demand and temperature dependency of high temperature of H_2O and CO_2 co-electrolysis; calculated from thermochemical data by using *Ref.* [43].

The well-known FISCHER-TROPSCH process has been established in terms of production of synthetic fuels. Thus, the combination of high-temperature steam/CO_2 co-electrolysis and the Fischer-Tropsch process offers an attractive approach to convert efficiently low-emission electrical energy to transportable chemical energy.

2.4 Photo-electrochemical water-splitting

More or less, the functions of a solar cell and an electrolyzer are now combined to one single device, which is favorable in terms of packaging. Such a photo-electrochemical cell (PEC) is used to split water. The preliminary scientific work has been started in the early 1970s and has been published by A. FUJISHIMA et *al*. (*Ref.* [21,44]) using rutile (TiO_{2-x}) as photo-anode and platinum (Pt) as cathode in an aqueous environment and imposed of an external bias between the two electrodes.

In this setup the photo-active semiconductor and the counter electrode are immersed in an aqueous electrolyte. The photo-generated electrons (e^-) and the electron-holes (h^+) are directly used to reduce and oxidize water. The water is provided by the electrolyte and has to be added. When the semiconductor (*e.g.* metal oxide with semiconducting property) is illuminated by photons that have an energy that is equal to or larger than the band gap E_g, electrons are excited from the valence band to the conduction band.

The photo-electrode conventionally consists of an *n*-type semiconductor. Exposure to the light results in intrinsic ionization over the band gap.

$$2h\upsilon \rightarrow 2e^- + 2h^+. \tag{2.21}$$

According to Eq. 2.21 of incident light, electrons are excited from the valence band to the conduction band. This intrinsic ionization of semiconducting oxide materials leads to the generation of electron-hole pairs (e^-, h^+). h represents the Planck's constant and ν is the wavelength of the radiation. Reaction in Eq. 2.21 takes place when the energy of the photons ($h\nu$) is equal to or larger than the band gap of the semiconducting material. For the application in PECs, the most promising material for the photo-active anode is TiO_2 which shows with regard to its relatively large band gap (3.0 eV) good corrosion resistance in aqueous environments [45,46]. For photocatalysis by using TiO_2; material related aspects as well as surface phenomena have been examined in detail [47].

In case that TiO_2 is used as photo-anode, the wavelength of the light source has to be equal to or less than 415 nm. The amount of photon energy ($h\nu$) less than 415 nm (regarding the utilization of TiO_2) will generate electron-hole pairs and heat losses. The heat turnover will increase as the amount of photon energy is larger than the band gap of the semiconducting material (*e.g.* $TiO_2 \rightarrow E_g$ is 3.0 eV).

The recombination of electrons and holes is prevented by the presence of an electrical field at the electrode/electrolyte interface [48]. This electrical field is generated by applying an external bias. It is known that a positive bias on an *n*-type semiconductor is favorable for the observation of photocurrents since the minority charge carries, in that case holes (h^+), tend to go to the surface while electrons (e^-) go towards the bulk of the semiconductor [49]. The photoelectrochemical water-splitting in PECs has been demonstrated in alkaline and acid electrolyte solution. In both configurations the illuminated electrode is working as photo-anode where the oxygen releasing reaction takes place. In one case water from the aqueous electrolyte is oxidized by the holes (h^+) and protons (H^+) are dispersed to the aqueous electrolyte. In the other case the photo-generated h^+ are oxidizing the hydroxide ions (OH^-) at the electrode/electrolyte interface by releasing water and oxygen. In the following, the reactions at the photo-anode and cathode for both configurations under illumination will be discussed.

The electrons (e^-) are transferred to the counter electrode where they reduce protons (H^+) to gaseous hydrogen by using an acid electrolyte [50,46,51], according to Eq. 2.22.

$$2\mathrm{H}^+_{(aq)} + 2e^- \rightarrow \mathrm{H}_{2(gas)}. \tag{2.22}$$

The holes (h^+) that remains in the valence band migrate to the anode/electrolyte interface where they oxidize water to gaseous oxygen and protons.

$$\mathrm{H_2O}_{(liq)} + 2h^+ \rightarrow 2\mathrm{H}^+_{(aq)} + \tfrac{1}{2}\mathrm{O}_{2(gas)}. \tag{2.23}$$

The overall reaction in a PEC is

$$2h\upsilon + H_2O_{(liq)} \rightarrow H_{2(gas)} + \tfrac{1}{2}O_{2(gas)}. \quad (2.24)$$

When the PEC cell is operating with an alkaline electrolyte solution [52,53], hydroxide ions (OH^-) are exchanged between the photo-anode and the cathode. In this case the oxidation at the photo-anode and is given by

$$2OH^-_{(aq)} + 2h^+ \rightarrow H_2O_{(liq)} + \tfrac{1}{2}O_{2(gas)}. \quad (2.25)$$

The holes (h^+) that remains in the valence band migrate to the anode/electrolyte interface where they oxidize hydroxide ions (OH^-) from the alkaline solution. Gaseous oxygen is evolved at the photo-anode and water is dispensed to the aqueous electrolyte solution.

The photo-generated electrons were transferred by external circuit to the metal electrode which is preferably made of platinum (Pt) because of the favorable catalytic and chemically resistant behavior. At the Pt electrode the cathodic reaction takes place where OH^- anions are dispensed to the aqueous electrolyte solution and hydrogen is evolved.

$$2H_2O_{(liq)} + 2e^- \rightarrow 2OH^-_{(aq)} + H_{2(gas)}. \quad (2.26)$$

The overall reaction is equal to the water-splitting reaction according Eq. 2.24.

Since the groundbreaking work of A. FUJISHIMA and K. HONDA (*Ref.* [21]), the method of photo-electrochemical water-splitting has been continuously improved. A general overview of photo electrolysis is given in [54,55,56]. It has been also thermodynamically considered to use concentrated solar radiation for photoelectrochemical water-splitting [57,58].

A PEC cell operating with an acid electrolyte solution was performed by T. BAK and J. NOWOTNY [51] and is shown below

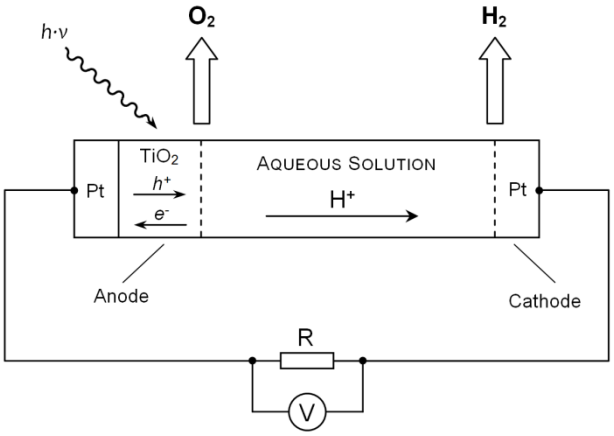

Figure 2.9: Photo-assisted electrochemical water-splitting in an acid electrolyte solution. Own graphic, adapted from *Ref.* [51].

From a thermodynamic point of view, the photo-electrochemical water-splitting is an *endothermic* ($\Delta H_r > 0$) and an *endergonic* ($\Delta G_r > 0$) reaction. Therefore, it is not possible to split water spontaneously, which means that a work input is necessary to run the reaction. The standard Gibbs energy (ΔG_r^0), also called standard free reaction enthalpy, for the water-splitting is 237.141 kJ mol^{-1} [9]. The water-splitting reaction (acc. Eq. 2.24) takes place when the energy of the photons absorbed by the photo-anode is equal to or larger than the threshold energy (E_t):

$$E_t[J] = \frac{\Delta G^0_{H_2O}}{2N_A} = 1.9689 \cdot 10^{-19}\text{J}, \tag{2.27}$$

where ($\Delta G^0_{H_2O}$) is the molar standard free enthalpy of the reaction (237.14 kJ mol^{-1}) and N_A is the Avogadro's number (6.022 ·10^{23} mol^{-1}). The physical correlation between J and eV is defined as:

$$1\text{eV} = 1.6022 \cdot 10^{-19}\text{J}. \tag{2.28}$$

That leads to the following expression:

$$E_t[\text{eV}] = h\,\nu = 1.23\ \text{eV}. \tag{2.29}$$

In case of TiO_2 as photo-anode, the maximum value obtained for photo-voltage of a PEC is 0.7 – 0.9 V [48]. According to reaction 2.24, the electrochemical decomposition of water at standard conditions (T^0= 298.15 K, p^0 = 1 bar) is possible when the electromotive force (EMF) is equal to or larger than,

$$E^0_{\text{H}_2\text{O}}[\text{V}] \geq \frac{\Delta G^0_{\text{H}_2\text{O}}}{2F} \geq 1.23\ \text{V}, \tag{2.30}$$

where F is the Faraday constant (96485.34 As mol^{-1}). In consequence of the low photo-induced voltage in case of TiO_2, an external bias is required to make the water decomposition possible.

Ideally, a PEC does not require an external bias for water decomposition. Previous studies have shown that although several oxide materials, including potassium tantalate ($KTaO_3$) and strontium titanate ($SrTiO_3$) [59,60] do not require an external bias. Regarding to TiO_2 as photo-anode an external bias voltage is certainly required [45,61]. According to real conditions, independently from the used materials (*e.g.* $SrTiO_3$, TiO_2) the application of a potential is necessary to overcome cell impedances.

Until now, it is an elusive goal to improve the photocatalytic behavior for the water-splitting reaction. For that purpose *e.g.* $SrTiO_3$ [62,63,64], $NaTaO_3$ [65,66,67] and TiO_2 [68,69,70] will be doped to obtain *n*-type semiconducting behavior.

3 EXPERIMENTAL INVESTIGATION AND DISCUSSION

A completely new approach for solar-chemical energy conversion was invented by the author of this thesis. A first draft of this method was presented in the diploma thesis [71] from the year 2011. Since that year, intensive research work has been carried out to search for the postulated photoelectrochemical effect at high temperatures. Since then, many different materials have been systematically investigated. In the following, the scientific work will be described in detail.

3.1 Principle

The characteristic of the invented *Solid Oxide Photo-Electrochemical Cell* (SOPEC) process (applied for patent [72,73,74]) is a **thermally assisted**, **photo-electrochemical energy conversion**, using a **solid oxide electrolyte** membrane and driven by **concentrated solar energy** for producing hydrogen and/or syngas (H_2+CO). The SOPEC consists of a photo-anode (1), a solid oxide electrolyte membrane (2), a cathode (3), and an external power supply (4). It is intended to use concentrated solar radiation (5) for the proposed process.

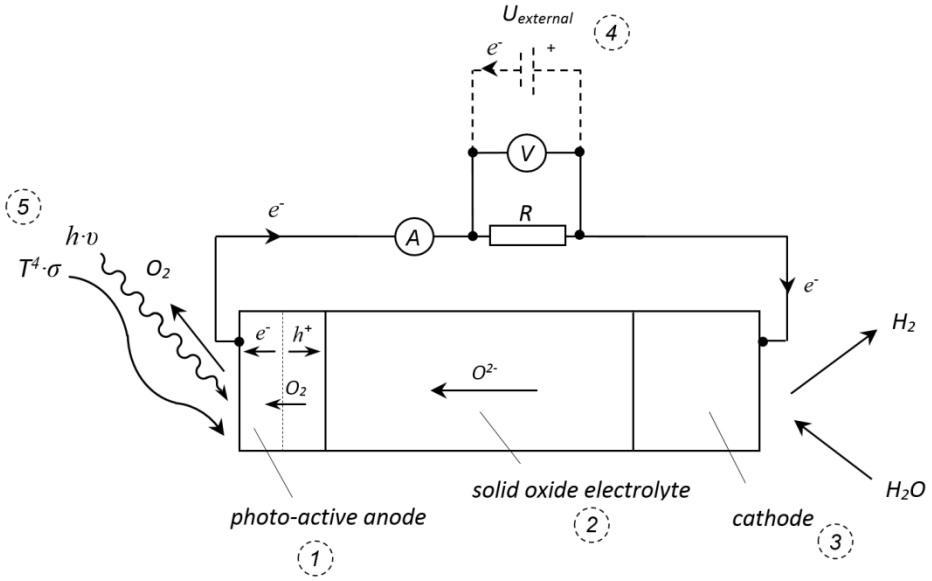

Figure 3.1: Schematic of the SOPEC cell, using concentrated radiation and an external power supply for a solar hydrogen production.

In previous theoretical considerations the principle of this novel process was found. The proof-of-concept was demonstrated in further works and still continues. With respect to the schematic of the SOPEC design in **Figure 3.1**, the thermal assisted photo-electrochemical energy conversion process may be described by several reactions, such as the light-induced intrinsic ionization (acc. Eq. 2.21); resulting in the formation of electron-hole pairs in the photo-electrode; reduction of steam at the cathode (Eq. 3.1), and oxidation of oxygen ions at the anode (Eq. 3.2).

The specification of the requirements for the photo-electrode plays a main role; therefore a lot of time was spent on theoretical and practical considerations. Later on the function of the photo-electrode will be discussed in detail. In the proposed process, the current generated by a high-temperature photovoltaic (HT-PV) element packed on top of the photo-electrode is led back to the anode where water-steam is decomposed in gaseous hydrogen and oxygen ions (O^{2-}).

$$H_2O_{(gas)} + 2e^- \rightarrow O^{2-} + H_{2(gas)}. \quad (3.1)$$

O^{2-} ions are passing through the cathode and straight through the thermal activated electrolyte. The ion conduction through the electrolyte is realized by a *solid oxide membrane* using commercial *yttria stabilized zirconia* (YSZ). O^{2-} ions are discharged at the photo-anode. The oxidation of the oxygen ions is defined as:

$$O^{2-} + 2h^+ \rightarrow \tfrac{1}{2}O_{2(gas)}. \quad (3.2)$$

The proposed process in favorable case takes place without an external power supply. For the SOPEC cell, the overall reaction is given by

$$2hv + H_2O_{(gas)} \rightarrow H_{2(gas)} + \tfrac{1}{2}O_{2(gas)}. \quad (3.3)$$

3.1.1 Pre-study considerations

Since previous experimental studies, metal oxides like TiO_2 (band gap, E_g, of 3.0-3.2 eV) [46] or $SrTiO_3$ (E_g of 3.2 eV) [59] are well known semiconducting materials regarding to their high chemical stability. Both metal oxides and many others are used for water decomposition in a PEC in aqueous environment, as already mentioned in chapter 2.4. The wide band gap E_g excludes the utilization of radiation with longer wavelength. That leads to poor efficiencies; because just a small portion of radiation spectrum is used.

The purpose of this new approach is the creation of conditions for the energy conversion at high temperatures up to 500°C. The **key issue** here **concerns material related aspects**, such as determination of materials with a significant **photoactivity at high temperatures**. **The materials which are applied successfully in PECs** (see chapter 2.4) **are non-transferable to the SOPEC approach**. The function of each part of the SOPEC cell will now be explained in detail, as well as critical aspects related to the **thermal assisted photo-electrochemical water decomposition** which can be realized by the SOPEC cell. The introduction is focused on following critical parts of the cell:

1. PHOTOELECTRODE
2. EXTERNAL CIRCUIT
3. INTERNAL CIRCUIT
4. COUNTER-ELECTRODE

PHOTO-ELECTRODE. The function of the photo-electrode is predominant for the SOPEC process. In previous theoretical studies the requirements in terms of physical and chemical behavior have been defined closely.

For this proposed thermal assisted mode the ion conduction is realized by oxygen ions (O^{2-}). In that consequence water steam has to be split in oxygen ions and gaseous hydrogen. **Initially, it was considered that the photo-electrode performs as a photo-cathode**. Afterwards, in the further evolution of investigation and characterization process it was found that the **photo-electrode should perform as anode**, as shown in Fig. 3.1. This substantial evolution process is now carried out.

A predominant part of effort was related to theoretical and practical considerations for performing a photo-electrode. Critical points were essentially concerned with material related aspects. The main challenge was associated with identifying of **a solid state material** with **a mixed ionic and electronic conducting (MIEC)** behavior which shows a **significant photoactivity under short wave-length illumination at high temperatures**. Indeed, the influence of the atmosphere (*i.e.*, oxidizing, reducing) was also considered. This process has been extended over a period of three years. Unfortunately, the experimental results have been less than expected. This has led to a new approach in which the structure of the *Solid Oxide Photo-Electrochemical Cell* (SOPEC cell) has been **separated in a photoelectrical and an electrochemical** part. In retrospect, it has been shown that in this way it was possible to optimize several part of the entire SOPEC cell independently from each other. The phenomenon in terms of electrochemical behavior in mixed conductors upon light has been investigated by Gregor Walch (researcher of *SOPEC-Bridge* project) which is discussed in his PhD thesis.

In the beginning, the first considerations and activities were proceed by assuming that the photo-electrode shall work as a cathode; *i.e.* a photo-electrochemical reduction (*e.g.* water-splitting) under illumination. The investigation has been focused on mixed metal oxides from the archetype of *perovskite* with the general formula ABO_3. For that reason a **mixed conductor**, consisting of 30% iron doped strontium titanate $SrTi_{0.7}Fe_{0.3}O_3$ (STF73) has been electrochemically characterized in detail. By the way, results of additional scientific work on this material has been published, see *Ref.* [75,76,77]. In general, iron-doped strontium titanate ($SrTi_{1-x}Fe_xO_3$), STF, behaves like a typical *p*-type semiconductor electrode.

We assumed that a *p*-type semiconductor is favorable for inducing of a photocurrent during the period of illumination. Where the minority charge carries, electrons (e^-) tend to go to the surface, while the holes (h^+) go towards the bulk of the semiconducting metal oxide, and oxygen ions O^{2-} are incorporated at the illuminated surface of the *mixed ionic and electronic conducting* (MIEC) material. Unfortunately, a **significant change of photo-induced electronic conductivity has not been observed**! Therefore, AC measurements (electrochemical impedance spectroscopy, EIS) and DC measurements (current-voltage characteristics) have been performed in

different atmospheres and gas compositions (reducing and oxidizing), depending on temperature, light intensity, and wave-length.

The material system was extended towards strontium titanate ($SrTiO_{3-\delta}$) single crystal in 100 orientation (STO 100). STO comes also from the material family of perovskites. Undoped, *i.e*. intrinsic, STO shows more or less a moderate O^{2-} ion conduction, whereas the addition of Fe will increases the O^{2-} ion conductivity. In perfectly stoichiometric ABO_3 composition a divalent cation (Sr^{2+}) is on the A site, trivalent cations (Fe^{3+}) are on the B site and at the same site only tetravalent cations such as Ti^{4+} are accommodated. This must lead to oxygen vacancies in a ratio of one vacancy per two trivalent cations. One oxygen vacancy is divalent. Using KRÖGER-VINK notation [78], a vacancy is denoted by $V_O^{\cdot\cdot}$.

Intrinsic STO has a relatively high E_g of 3.2 eV. According to the wide E_g the utilization of irradiation with longer wavelength is excluded. The photo effect obtained upon irradiation with light of shorter wavelength than 390 nm, whereas a wavelength >390 nm will lead to heat-up the material. A decrease in E_g of the material will increase the range of useable radiation spectrum, especially with outlook for solar radiation. Fe-doped STO shows E_g less than 3.2 eV. E_g will decrease with the Fe concentration in the range of $0 < x < 1$. Increasing Fe content results in a systematic decrease in E_g, following a parabolic law $E_g^0 = (3.2 - 1.9x + 0.5x^2)$ eV [79,80]. Despite reducing of E_g by doping, **no photoconductivity or photoelectrochemical behavior in STF73** has been observed, whereas oxygen incorporation into slightly iron doped $SrTiO_3$ (Fe content of 4.6×10^{19} cm^3) under UV Irradiation has been reported [81]. We still **have not found** a conclusive scientific **answer** for this behavior. Possible reasons for this could be, for example, excessive dopant concentration, crystallinity, *etc*.

A **new attempt was initiated** to find a material system which shows a significant photoactivity for driving a photo electrochemical reaction. Fortunately, another mixed metal oxide material has been identified as a promising candidate for such application; *i.e*. **thermal activated photo electrochemical energy conversion**. Current-voltage (*I-V*) and electrochemical impedance spectroscopy (EIS) have been shown that the material system consisting of STO (100) with 10 and 20% strontium (Sr) doped lanthanum chromite ($LaCrO_3$) thin-film (approx. 400 nm) exhibits a significant photoactivity, *i.e*. light-induced current and voltage. This new research of $La_{1-x}Sr_xCrO_3$/ $SrTiO_{3-\delta}$ (100) heterojunction led to **a modification of the SOPEC cell design**. In a new approach, the $La_{1-x}Sr_xCrO_3$/ $SrTiO_{3-\delta}$ (100) heterojunction has been integrated to **perform a photo-anode** driven solid oxide photo electrochemical cell.

EXTERNAL CIRCUIT. In an ideal case, the SOPEC cell should be **able to operate without any external bias**. The energy of the excited state, in terms of formation of electron-hole pairs, is in a thermodynamic point of view *internal energy* (ΔH) and not *free energy* (ΔG). For a semiconductor at standard condition (T^0 = 298.15 K, p^0 = 1 bar) having a band gap larger than 1.48 eV the application of a potential is theoretically not necessary, whereas the free enthalpy for water decomposition is 1.23 eV at standard condition. The relation between changes in free energy (ΔG), internal energy (ΔH) and entropy turnover ($Q/T = \Delta S$) is given by the Gibbs-Helmholtz equation ($\Delta G = \Delta H - T\Delta S$); it has been already shown by a derivation from 1st and 2nd law of thermodynamics (chapter 1).

In reality, for achieving a high energy conversion rate, *i.e*. fuel production, an external bias voltage may be required. In this scientific work that is not intended. Therefore, the aim is to **demonstrate the thermally activated photochemical** water-splitting **without external energy** supply. In lab the solar radiation will be replaced by an artificial light source by the use of a *light emitting diode* (LED), with an electrical power of 10 watts, and a wave-length of 365 and 405 nm. In addition to that, LED with 10W/740 nm was used to investigate the influence of heat on photochemical reaction; *i.e*. **distinction** between **photo-induced** and **thermal activated** reaction.

The idea of SOPEC is performing the water decomposition at high temperatures, up to 500°C by using a short wave-length LED light source. At this temperature level ΔG drops to ~ 1.0 eV.

Due to the modification of the SOPEC cell arrangement (from photo-cathode to photo-anode driven SOPEC), the HT-PV element is packed on top of an electrolyte supported cell (ESC), which consist of LSF/YSZ/LSF. This leads to the fact that the top side of the ESC performs as an anode. Furthermore, the top of the HT-PV cell is short-circuited with the bottom of the ESC; *i.e*. performs as cathode. The architecture of the SOPEC cell is shown in Fig. 3.1 and Fig. 3.2. A very profound explanation of the function of SOPEC cell will be found in the experimental section of this thesis.

INTERNAL CIRCUIT. The oxygen ion (O^{2-}) conduction through the solid oxide membrane represents the internal circuit and connects the photo-anode with the cathode. For the ion conduction commercial *yttria stabilized zirconia* (YSZ) is used. The ionic conductivity in YSZ is strongly temperature dependent. The YSZ material is used in different forms. Firstly as single crystal in 100 orientation to receive well-defined thin-films. YSZ single crystals (9.5 mol% Y_2O_3) in the dimensions (5x5x0.5) mm, (10x10x0.5) mm and (Ø20x0.5) were purchased from CrysTec GmbH, Germany. Secondly, the YSZ substrates were mainly used for the **light-induced oxygen pumping** and **water-splitting experiments**. Especially for this purpose,

polycrystalline YSZ substrates with 3 mol% Y_2O_3, 300 µm and 2 cm in diameter were used. The polycrystalline substrates are provided by KERAFOL, Keramische Folien GmbH, and are characterized by a high mechanical stability in opposite to YSZ single crystals with rather lower mechanical stability.

COUNTER-ELECTRODE. The photo-generated current is fed directly to the counter-electrode by short-circuiting the top of the high-temperature PV (HT-PV) element and the counter-electrode, as shown in Fig. 3.2. The reaction at this side of the electrode is a **cathodic reaction**, *i.e.* incorporation of oxygen ions (O^{2-}) or dissociation of water steam. This kind of reaction is well known from electrolysis in SOECs. The mechanism for oxygen incorporation in *mixed ionic and electronic conducting materials* (MIECs), *e.g.* in lanthanum-doped strontium manganate (LSM), have been investigated in detail [82,83,84].

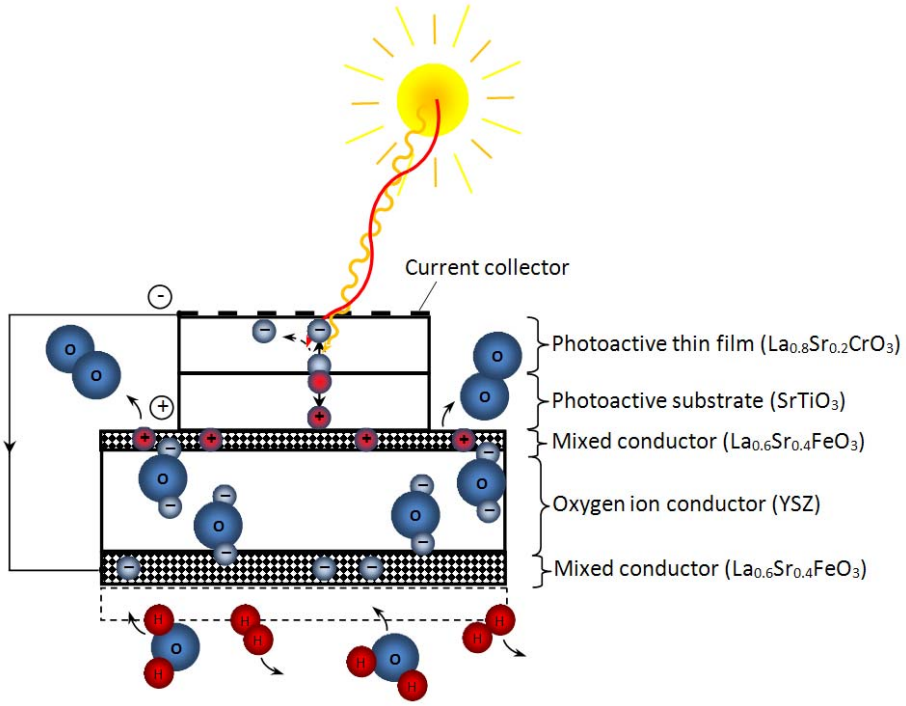

Figure 3.2: Sketch of the investigated Solid Oxide Photo-electrochemical cell operating between 400 and 500°C.

3.1.2 Pre-experimental study

The experimental studies were initiated with the synthesis of 30% iron doped strontium titanate $SrTi_{0.7}Fe_{0.3}O_3$ (STF73). After obtaining synthesized, sintered and pressed STF73 pellets, micro-structured electrodes are made. The deposited thin-film electrodes were characterized by current-voltage (DC) analysis and electrochemical

impedance spectroscopy (EIS). Later on the same procedure was done under illumination. For a sufficient proof, different geometries of micro-structured electrodes and current collectors were manufactured. The objective was to find a relationship between ionic and electronic depending on temperature (400-800°C) and gas atmospheres (reducing and oxidizing conditions). Finally, the electrochemical properties of the solid state material under illumination were investigated.

SYNTHESIS AND MICRO-ELECTRODES. The choice fell to STF73 after a theoretical study [79,80,62,63]. STF73 was prepared by use of commercial fine powder (Sigma-Aldrich, Merck) with high purity (99.99%) of $SrCO_3$, TiO_2 and Fe_2O_3. The powders were mixed in appropriate amounts to obtain the desired Fe/Ti ratio. In a first attempt the ratio (Fe/Ti) of 0.3/0.7 was adopted. After calcination and sintering a pellet of STF73 was obtained. An X-ray analysis of the synthesized material has shown a perovskite structure of $SrTi_{0.7}Fe_{0.3}O_3$, *i.e.* free from phase shift. By pulsed laser deposition (PLD) the synthesized STF73 pellet was deposited on YSZ. The thicknesses of the thin-films were between 300 and 500 nm. For getting a correlation between deposition time and thickness of the thin-film layer several cross section images with *scanning electron microscopy* (SEM) by varying the distance between target and heater L_{TH} (as shown in **Figure 3.3** – **Figure 3.5**) were analyzed. The deposition time was 20 min (12,000 pulses) with a laser pulse energy of 400 mJ (at the laser) and a repetition rate of 10 Hz. In a further step, the produced layer was micro-structured by UV-lithography obtaining a large number of microelectrodes on a single crystal YSZ substrate (10x10x0.5) mm.

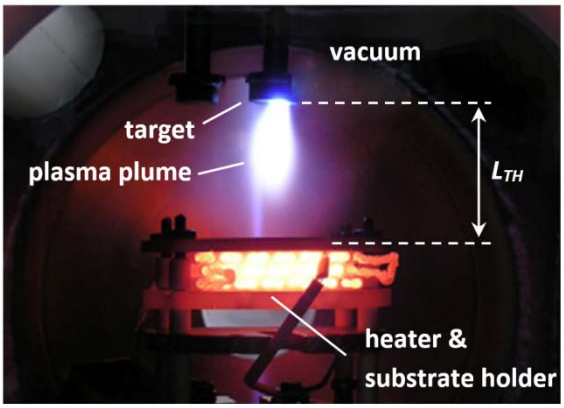

Figure 3.3: View in the vacuum chamber of an operating PLD and the indicated distance between target and heater.

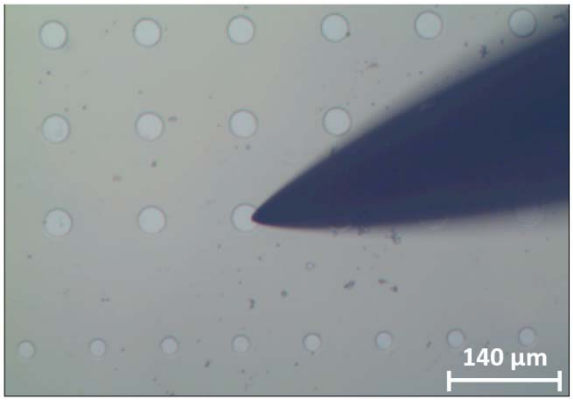

Figure 3.4: Micro-structured STF73 electrodes deposited on YSZ (100) single crystal and electrically contacted by high-precision manipulators for electrochemical characterization.

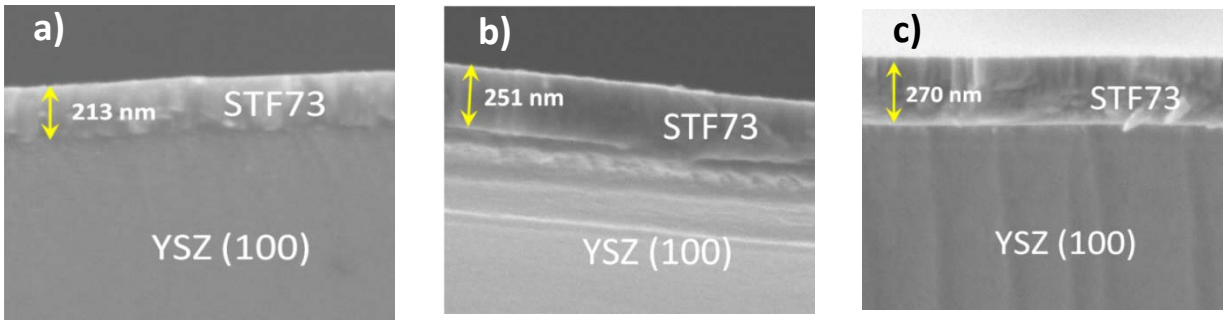

Figure 3.5: SEM cross section image of a 30% Fe doped $SrTiO_3$ (SFT73) layer on a YSZ (100) single crystal deposited with a) L_{TH} = 7.5 cm, b) L_{TH} = 7.0 cm and c) L_{TH} = 6.5 cm.

MEASUREMENT AND SETUP. The measurements take place at temperatures in the range of 500–800°C. The chamber, in which the micro-structures cell will be analyzed, is isolated from the ambiance. Therefore, various atmospheres inside the chamber are adjustable (*e.g.* O_2, N_2/H_2O). Generally, the electrochemical characterization consists of current-voltage (DC) analysis and electrochemical impedance spectroscopy (EIS). At first, current-voltage-curves below and above the water-splitting potential are sensed, obtaining information about kinetics and catalytic behavior of the electrode. Secondly, similar to the procedure before, the measurements will be done under irradiation with light.

Before starting with the research of the pre-experimental study, some basics of EIS characterization will be shown to understand the principles behind this very powerful method. EIS is predominantly used for the electrochemical characterization and measures *dielectric properties* of a material system as a *function* of *frequency*.

In general, *impedance* can be defined

- as a **complex** resistance,
- composed of various **resistors**, **capacitors** or **inductors**,
- considers the **phase differences** between input voltage and output current.

Both, *linear* and *non-linear* systems can be analyzed by using EIS. For instance, electrochemical cells have **non-linear** behavior. At small AC signals (1-10 mV), electrochemical cells become **pseudo-linear**, as indicated in **Figure 3.6**. Systems, *i.e.* electrochemical cells, which are being measured, must be at steady-state. Otherwise, systems which are changing in time provide non-reproducible results. Reasons for being not at steady-state are:

- adsorption effects,
- temperature changes,

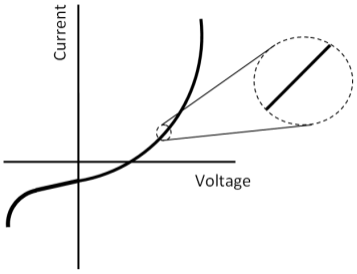

Figure 3.6: Pseudo-linearity of electrochemical systems at low AC amplitudes.

- degradation,
- build up of reaction products,
- *etc.*

A small excitation leads to a pseudo-linear response and results in characteristic phase shifts. The excitation signal and the response signal are functions of time *f(t)*.

excitation: $$E(t) = E_0 \sin(\omega t), \tag{3.4}$$

where *E(t)* is the potential at time *t*, E_0 is the amplitude, ω is the radial frequency with $2\pi f$, and *f* is the frequency.

response: $$I(t) = I_0 \sin(\omega t + \emptyset), \tag{3.5}$$

where *I(t)* is the response at time *t*, I_0 is the amplitude and $\emptyset$ is the phase shift. The complex impedance is derived similar to Ohm's law and is given by:

$$Z = \frac{E(t)}{I(t)} = \frac{E_0 \sin(\omega t)}{I_0 \sin(\omega t + \emptyset)} = Z_0 \frac{\sin(\omega t)}{\sin(\omega t + \emptyset)}, \tag{3.6}$$

where *Z* represents the impedance and Z_0 is the magnitude.

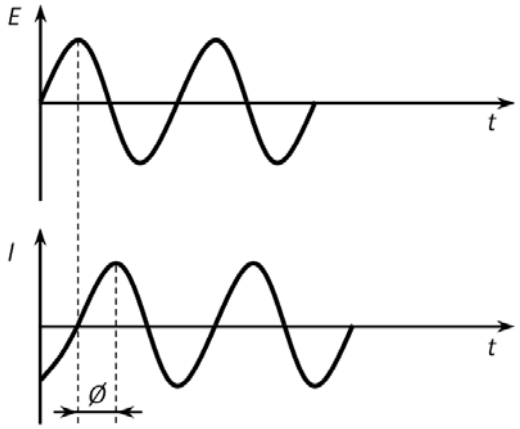

Figure 3.7: Excitation signal and response signal at time *t* with the phase-shift $\emptyset$ in the response signal.

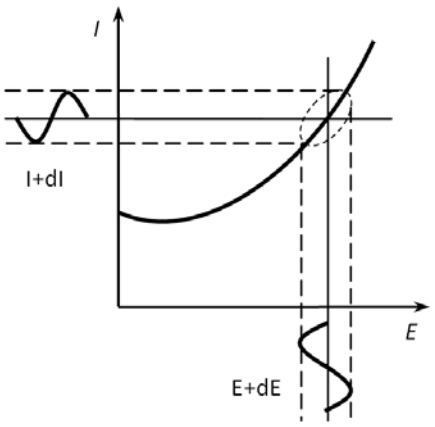

Figure 3.8: Excitation signal and response signal plotted in Lissajous figure.

With EULER relationship $\exp(j\emptyset) = \cos \emptyset + j \sin \emptyset$, the representation of impedance can be expressed as a complex function as follows: $E(t) = E_0 \exp(j\omega t)$ and $I(t) = I_0 \exp(j\omega t - j\emptyset)$ with $Z(\omega) = E(t)/I(t)$ gives

$$Z(\omega) = \frac{E(t)}{I(t)} = \frac{E_0 \exp(j\omega t)}{I_0 \exp(j\omega t - \emptyset)} = Z_0 \sin(\cos \emptyset + j \sin \emptyset). \tag{3.7}$$

The complex impedance $Z(\omega)$, as shown in Eq. 3.9. is composed of a *real* and an *imaginary* part. In regard to the graphical representation, the real part is plotted on *x*-axis and the imaginary part is plotted on *y*-axis.

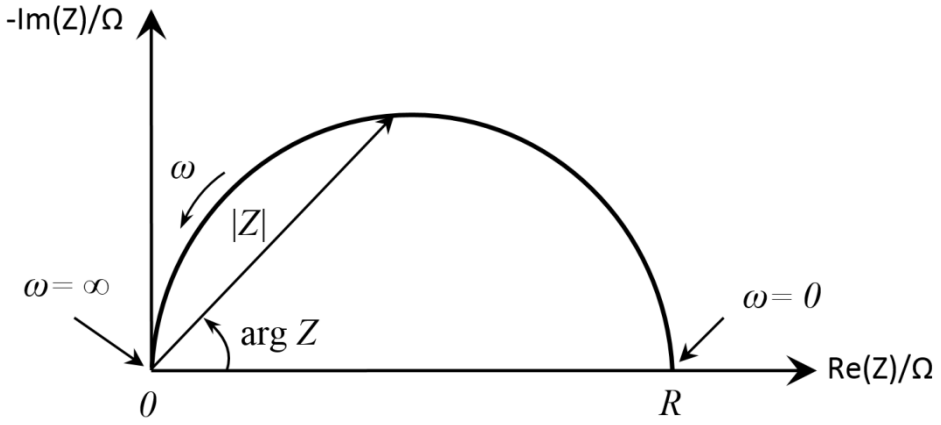

Figure 3.9: Representation of complex impedance constituted as Nyquist plot.

Each point on the Nyquist plot represents the impedance at **a certain frequency**. Furthermore, the Nyquist plot, depicted in **Figure 3.9** can be also expressed as an equivalent electrical circuit as shown in **Figure 3.10**. Such electrical networks can be very extensive. Each element, *i.e*. resistor *R*, capacitor *C*, inductor *L* are connected in series and/or in parallel. In that way, data from EIS measurement can be fitted to a model representing an equivalent circuit.

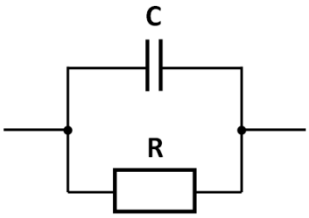

Figure 3.10: Equivalent circuit.

Micro-structured cells (such as shown in Fig. 3.4.) were electrochemical characterized in a setup which is isolated from surroundings. Especially, this was important in terms of electrochemical characterization in different gas atmospheres. The microelectrodes (10-100 μm in diameter) were contacted by micro-manipulated tips by use of a microscope. Such setup is shown below in **Figure 3.11** and **Figure 3.12**.

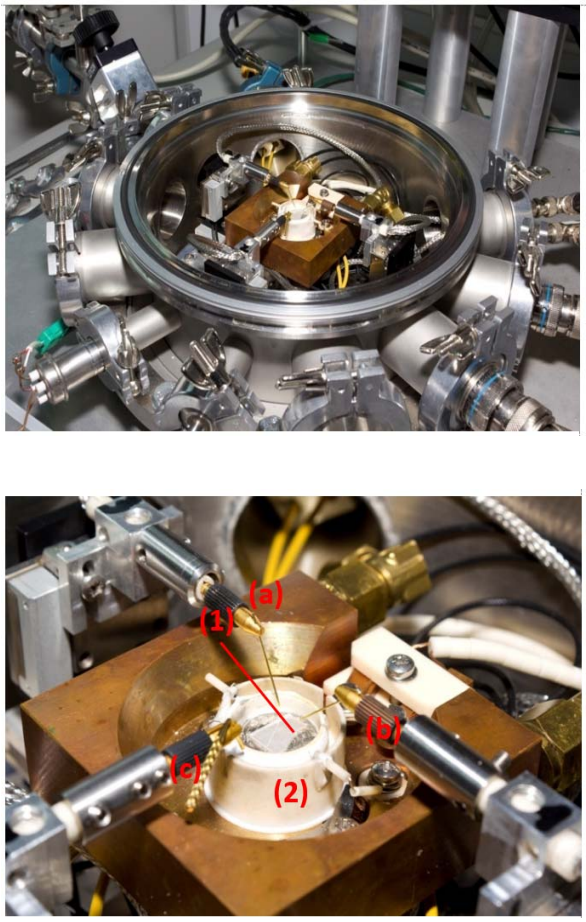

Figure 3.11: Chamber with heating stage, cooling system and high-precision micro-manipulators.

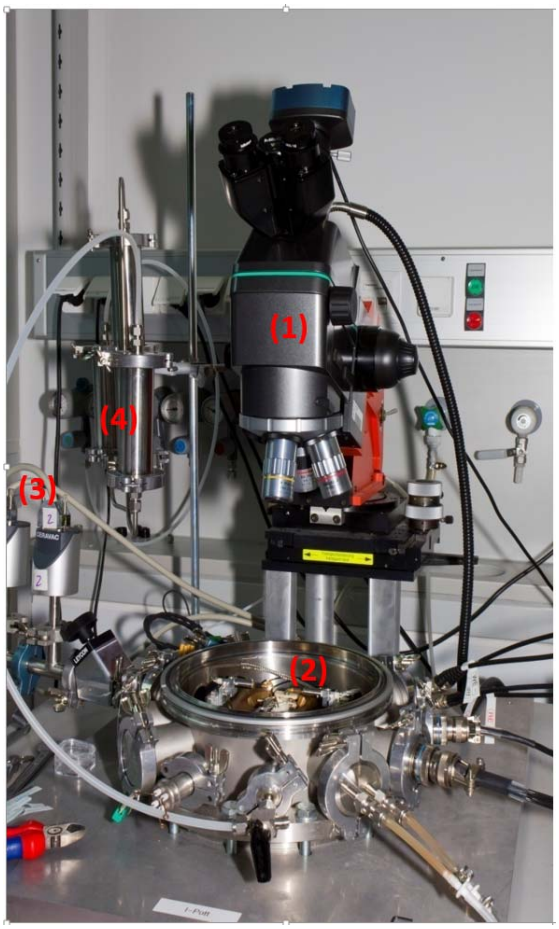

Figure 3.12: Setup for electrochemical characterization with microscope (1), chamber with heating stage (2), pressure gauges (3) and humidifier (4).

As shown in Fig. 3.11, one of the needles (a) is connected with the counter electrode, the second one with the microelectrode (b) of the investigated material (*e.g.* SFT73) and the third one can be applied alternatively (c), *e.g.* as reference electrode. The cell (1) is located on the heating stage (2). The substrate of the cell consists of single-crystal YSZ (100) where the STF73-microelectrodes are deposited. As counter electrode a stripe of silver (Ag) or platinum (Pt) is used. Note that the counter electrode was approx. 100 times bigger than the investigated microelectrode. In that case the influence of the counter electrode, *i.e.* the resistance is negligible.

PRE-EXPERIMENTAL RESULTS. The results of electrochemical characterization of STF73 thin-film microelectrodes deposited on YSZ (100) were differently than we expected. Especially there was **no significant light-induced photo conductivity** observed, *i.e.* neither ionic nor electronic conductivity change. For this purpose EIS characterization was performed (see **Figure 3.13**).

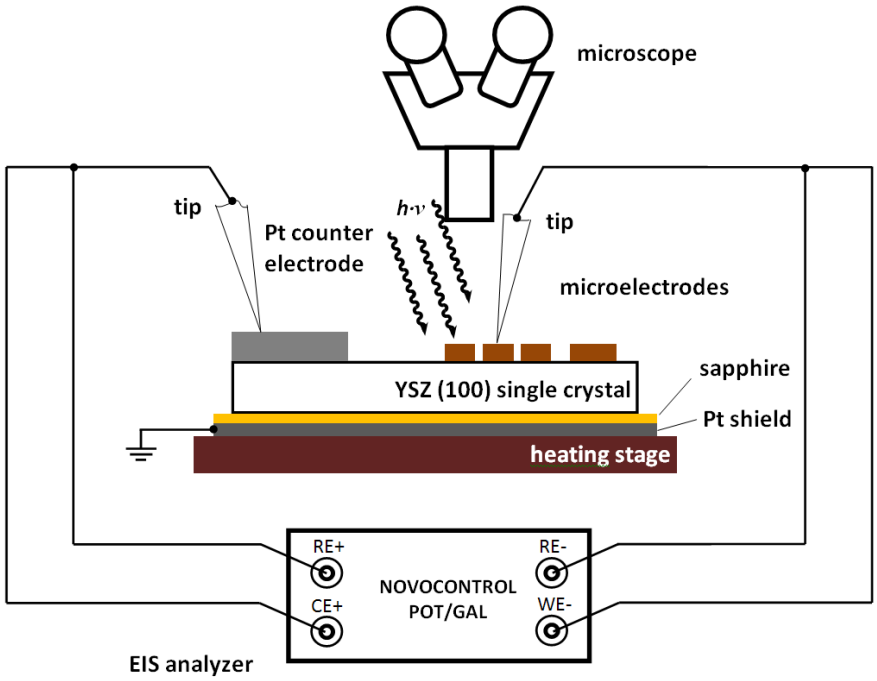

Figure 3.13: Sketch of the investigated STF73 thin-film microelectrodes deposited on YSZ (100) and the measurement arrangement for electrochemical characterization with EIS.

The micro-structured cell in Fig. 3.4 was analyzed in a setup as shown in Fig. 3.14. The micro-electrodes were illuminated by using a 50 W halogen lamp. The emitted light (SoLux, 50 W, 4700 Kelvin) provided a sunlight-similar flash spectrum; according to datasheet.

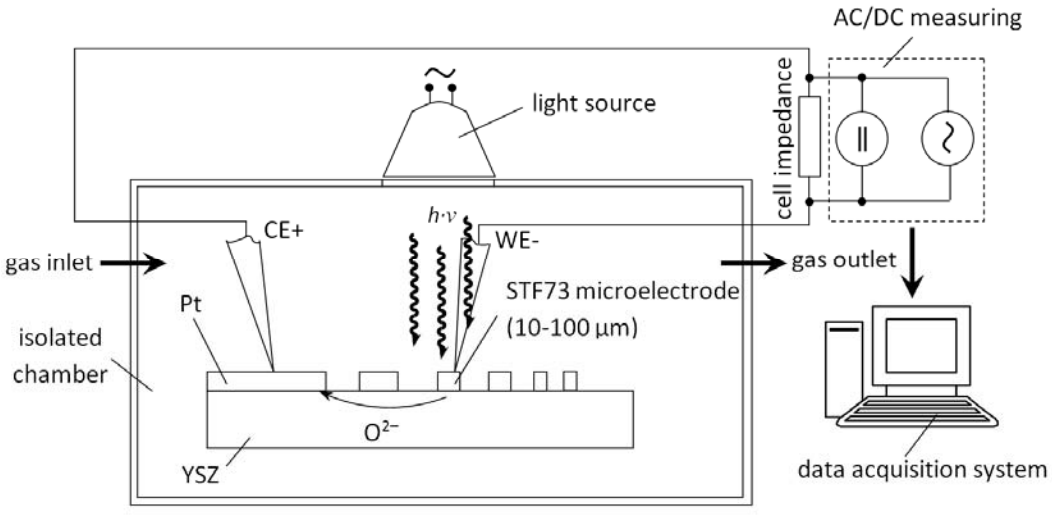

Figure 3.14: Sketch of the measurement environment for electrochemical characterization with EIS.

As previously mentioned, the results were not as satisfactory as we assumed. There was **no significant change in photoactivity under illumination**. It has become clear

that **the initially wrongly assumed photo effect** in STF73 thin-films **was thermally activated**, as shown in **Figure 3.15** and **Figure 3.16**.

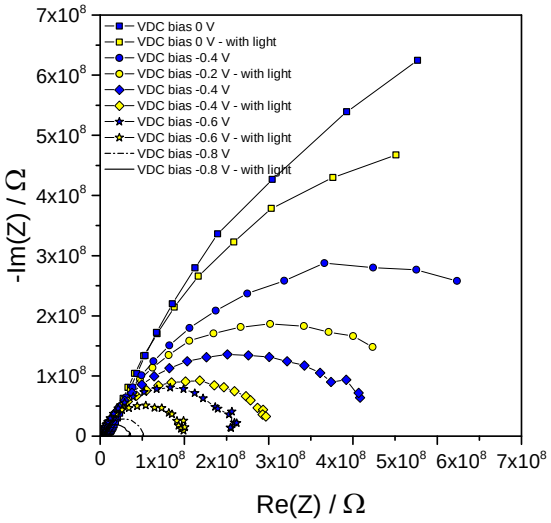

Figure 3.15: EIS measurements on STF73 thin-film microelectrodes with 40 µm in diameter at 700°C (T_{set}) in wet N_2 gas atmosphere by switching the light source (SoLux, 50 W, 4700 Kelvin) on and off.

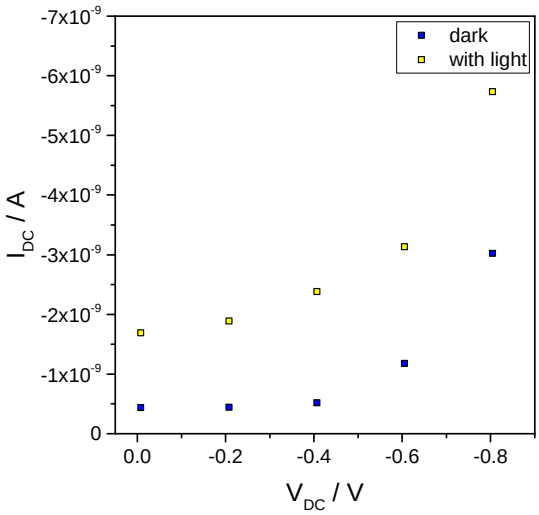

Figure 3.16: DC measurements on STF73 thin-film microelectrodes with 40 µm in diameter at 700°C (T_{set}) in wet N_2 gas atmosphere by switching the light source (SoLux, 50 W, 4700 Kelvin) on and off.

The difference in resistance (**Figure 3.15**) and in *I-V* measurements (**Figure 3.16**) by switching the light source on and off was **primarily thermal activated**.

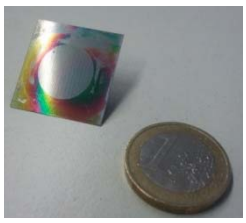

Subsequently, electrochemical cells consist of polycrystalline substrates (25x25x0.3) mm were deposited with STF73 thin-film (approx. 400 nm). On top of the STF73 thin-film a platinum (Pt) current-collector was sputtered. The back side of the substrate was manufactured analogously, as shown in adjacent figure. For these measurements a tubular furnace was used in which a tubular reactor with a fixed STF73/YSZ/STF73 cell was inserted. The cell was fixed between two corundum (Al_2O_3) pipes. At one side the light is fed into the tubular reactor (1).

Figure 3.17: Arrangement of the tubular furnace with the inserted tubular reactor.

Figure 3.18: Setup with a light source by using a 1000 watts xenon arc lamp.

At the other side the temperature of the cell was measured with a pyrometer (2). The nitrogen gas fed to the illuminated side of the cell was humidified by bubbling through water at 30 °C (3). The water content in the nitrogen gas flow is thereby determined with approx. 25 mbar. The arrangement of the experimental setup is shown in **Figure 3.17** and **Figure 3.18**.

The results of the measurement on STF73/YSZ/STF73 cell are shown in **Figure 3.19**. A **photo-induced** effect was not observed.

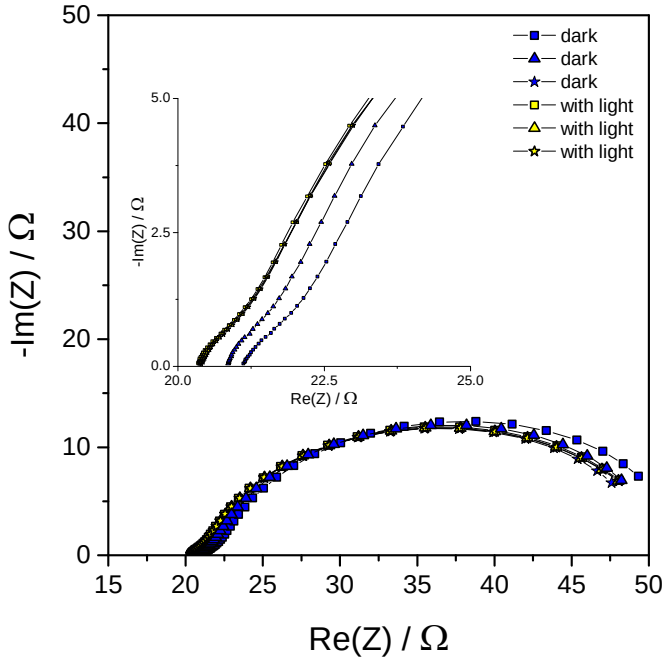

Figure 3.19: EIS measurements on STF73/YSZ/STF73 (25x25x0.3) at 600°C (T_{cell}) in wet N_2 gas atmosphere by switching the light source (Newport, 1000 watts, xenon arc lamp) on and off.

As can be seen from Fig. 3.19, the observed effect is exclusively **thermal activated**. The resistance of the O^{2-} ion conductor (YSZ) is highly temperature-dependent. By switching on the light source, the radiation absorbed by the cell leads to an additional heating of the cell about approx. 5°C. When the light is switched off, the resistance increases to 22 Ω.

Unfortunately, an indication of a significant photo effect in form of photo conductivity has not been observed. However, in separate studies a model for the description of the electronic and ionic conductivity in mixed metal oxides based on STF73 was found. A benefit in regard to this model lies in a separate consideration of the electronic and the ionic conductivity. The results have been published in *Ref.* [76,75,77].

These results lead to a drastic change in the concept. It was absolutely necessary to identify a new material system which has photoactivity at high temperatures.

Therefore literature has been studied. In that context *strontium doped lanthanum chromite* ($La_{1-x}Sr_xCrO_3$) has been identified as a promising candidate [85,86].

3.2 New conceptual research and approach

In the course of experimental investigation and strontium titanate ($SrTiO_3$) *thin-films* and *single crystals* have shown a significant photoactivity. Furthermore, it was found that *strontium doped lanthanum chromite* ($La_{1-x}Sr_xCrO_3$) thin-films deposited on $SrTiO_3$ (STO) single crystals (1), and thin-films (2), lead to an appreciable photo-current and photo-voltage under illumination. For that purpose, two different kinds of high-temperature photovoltaic (HT-PV) cells were composed. The best results have been achieved with the cell type (1). The light-induced photo-voltage and photo-current for cell type (2) were rather low (~100 mV, ~10 µA at 300 °C). The reason for this is not precisely known but it probably lies in the STO thin-film itself or in the impurity of the STO basis material (99%). The maximum achieved values for cell type (1) under illumination (with LED, 10 W electrical power and 365 nm wave-length) were a short-circuit current (I_{SC}) of 2.3 mA at 500°C and open-circuit voltage (V_{OC}) of 900 mV.

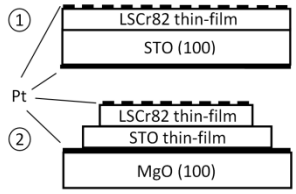

In addition to that, an exceptionally high photoactivity on STO (100) single crystal has been observed. For this purpose STO single crystals with different electrode arrangements were composed. STO single crystal with Pt as top electrode shows under illumination a drastic reduction of the resistance. By performing EIS measurements, it has been also observed that STO single crystal may show a kind of *stoichiometry polarization*.

Hence, a HT-PV cell consist of the heterojunction $La_{0.8}Sr_{0.2}CrO_3/SrTiO_3(100)$ has been identified as a promising candidate for a application in a photoelectrochemical cell. For that reason, the cell SOPEC design has been adapted. The unsatisfying measurement results on STF73/YSZ/STF73 cell lead to a new conceptual approach. For this reason, a new cell design for *HT-PV driven solid oxide photoelectrochemical cell* has been completed.

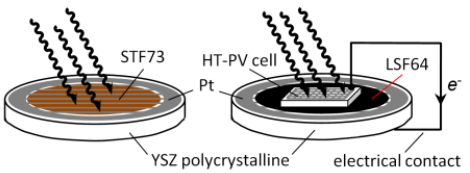

3.2.1 Photoconductivity of STO (100) single crystal

STO is a well-known material from the "family" of perovskites. The amount of literature for *strontium titanate* is extremely high and provides wide range of topics. In contrast to that, it seems that the photoelectrochemical properties of STO remain relatively unknown. However, STO was characterized with EIS measurements in dark and under illumination. For that purpose a STO single in 100 orientation with the dimension (10x10x0.5) mm was used. The electrodes at the bottom and on top were deposited by Pt sputtering. The mesh electrode on top of the STO single crystal was made by photolithography. A sketch of the investigated cell and the measurement setup are shown in **Figure 3.20**.

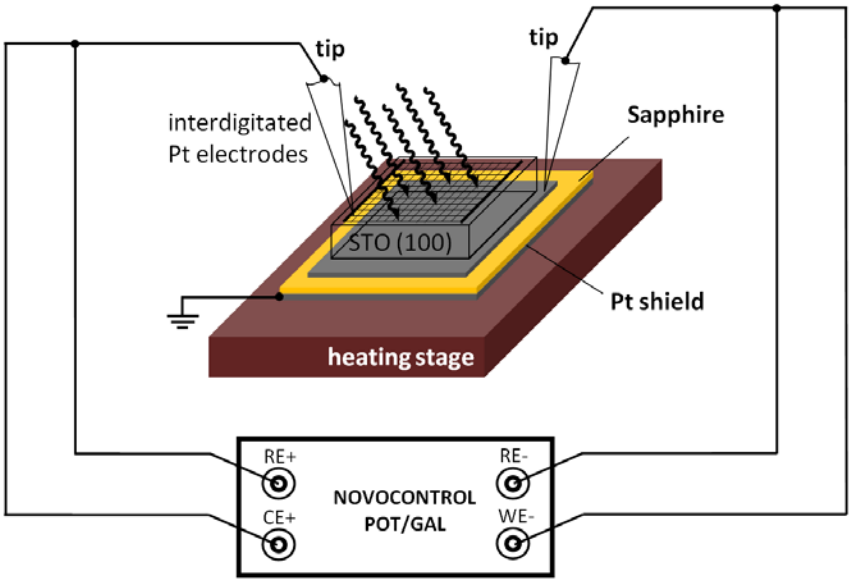

Figure 3.20: Sketch of the investigated STO (100) single crystal with the dimension (10x10x0.5) mm in dark and under illumination, equipped with a plane Pt bottom electrode and a Pt mesh electrode on top.

The results of EIS measurements on Pt/STO/Pt (acc. Fig. 3.20) with the sample ID **GB_STO_07** are shown as follows (**Figure 3.21** to **Figure 3.23**). The investigated Pt/STO/Pt sample was exposed in air under illumination with a LED (100 W/385 nm) by switching the light source on and off. The measurements were performed in a temperature range between 350°C and 450°C in a temperature step of 50°C.

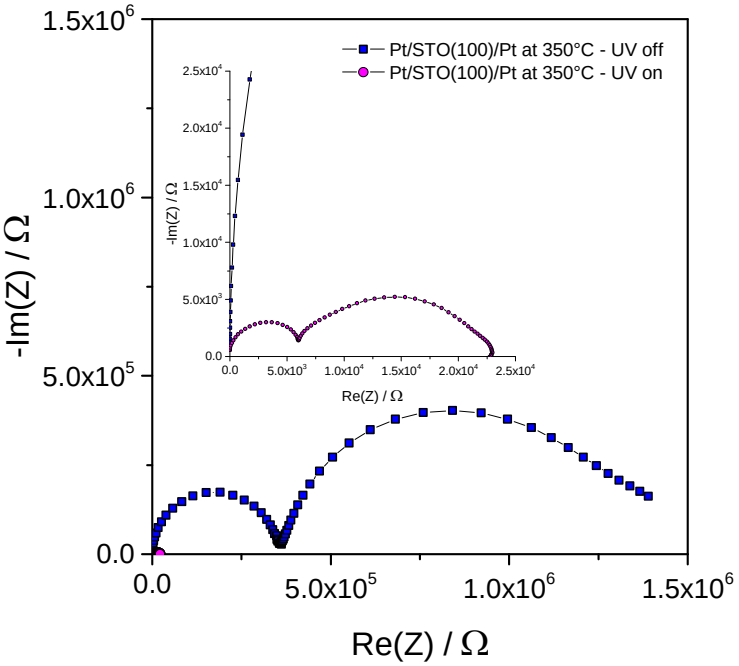

Figure 3.21: Impedance spectrum of Pt/STO(100)/Pt 350°C; the large spectrum represents the resistance of $SrTiO_3$ without illumination; under illumination the impedance spectrum is shrinking.

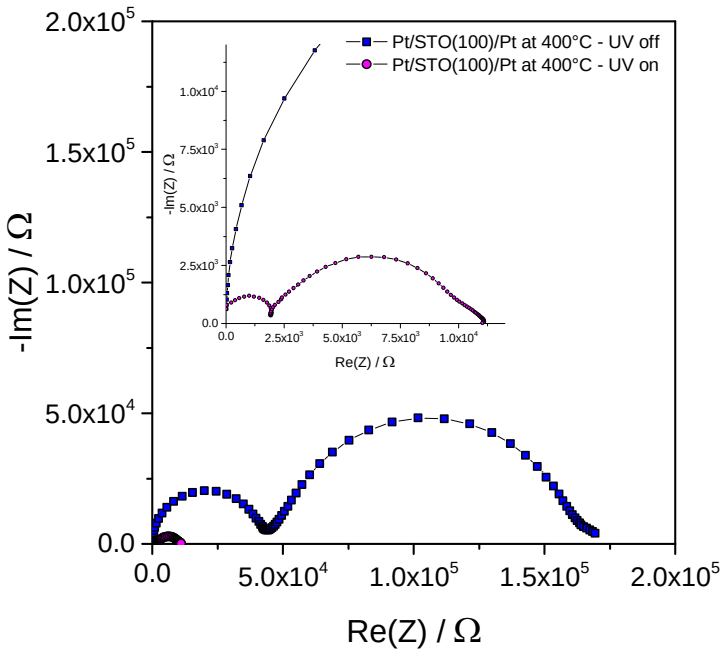

Figure 3.22: Impedance spectrum of Pt/STO(100)/Pt 400°C; the large spectrum represents the resistance of $SrTiO_3$ without illumination; under illumination the impedance spectrum is shrinking.

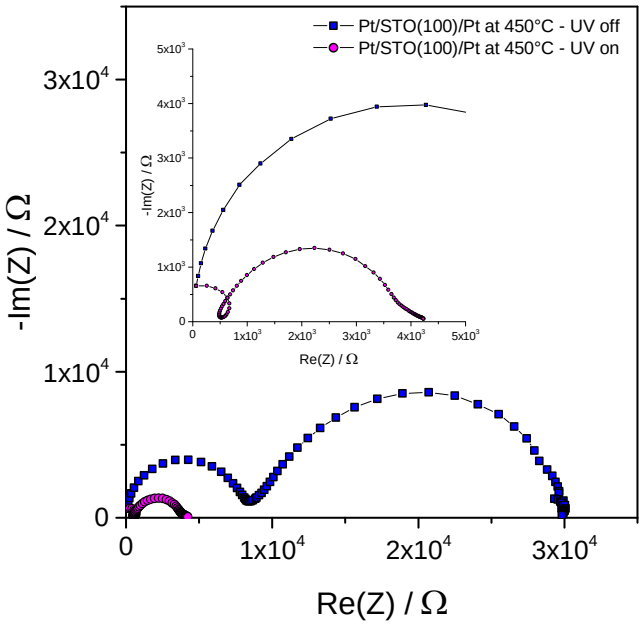

Figure 3.23: Impedance spectrum of Pt/STO(100)/Pt 450°C; the large spectrum represents the resistance of $SrTiO_3$ without illumination; under illumination the impedance spectrum is shrinking.

The dimension of the analyzed Pt/STO(100)/Pt was (10x10x0.5) mm. As can be seen above, the resistance of STO decreases dramatically under illumination. At 400°C (Fig. 3.22) and 450°C (Fig. 3.23) in the case of illumination the resistance will drop in the order of magnitude, and at 350°C (Fig. 3.21) even two orders of magnitude smaller.

In principle, these experimental results demonstrate that a **photo effect** does exist in ABO_3 materials in the form of **photo conductivity at high temperatures**. The objective in further research activities was an experimental investigation even more than just the photoelectrical properties in STO. **The research question here was:** Does STO show electrochemical changes (including ions) under illumination?

3.2.2 Photochemical properties of STO (100) single crystal

The following investigation is focused on photoelectrochemical characterization of STO single crystal with 100 orientation. For this purpose two different samples were prepared. Each of the STO 100 single crystals has a dimension of (5x5x0.5) mm. For an unambiguous identification of the measurement results, the cells were provided with a sample ID. The STO single crystal with the **interdigitated electrodes** has the ID **GB_STO_08** and that with the **circular electrode** has the ID **GB_STO_09**, as shown as follows.

GB_STO_08

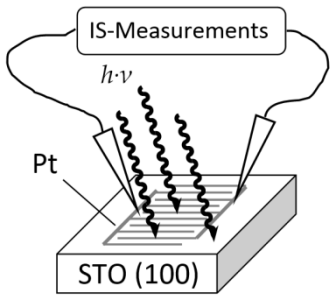

Figure 3.24: Pt/ STO(100)/ Pt single crystal in the dimension of (5x5x0.5) mm is equipped with an interdigitated top electrode; and exposed under illumination for EIS characterization.

GB_STO_09

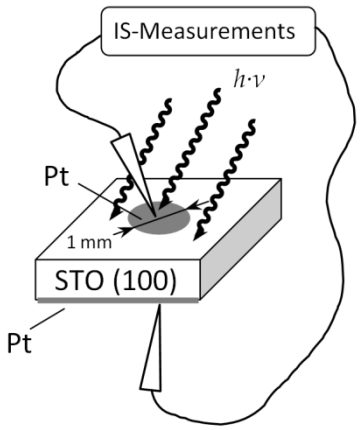

Figure 3.25: Pt/ STO(100)/ Pt single crystal in the dimension of (5x5x0.5) mm is equipped with a circular electrode on top with 1 mm in diameter including a plane bottom electrode; and exposed under illumination for EIS characterization.

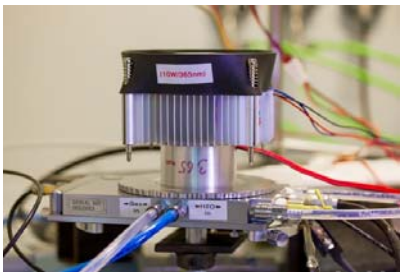

EIS measurements have been performed to investigate the photoelectrochemical behavior in STO single crystal. These measurements have been carried out at a set temperature of 450°C in air. The measurements on GB_STO_ 09 were performed in *I-Pot* setup, see Fig. 3.11. The experimental investigation on GB_STO_08 took place simultaneously in a specially adapted setup as shown in the figure beside.

The results from the experimental investigation will be discussed and presented now. The photo-conductivity in STO single crystal is already known from literature [87,79,88]. In the case of illumination at high temperature, there is rather few or no experience with regard to electronic and ionic conductivity available. Exactly for this reason it seems to be very interesting to know, how the photo-conductivity is changing by use of light sources with different wave lengths? For this purpose a various number of LED sources with the wave lengths 740, 460, 405 and 365 nm were used. Each light source has an electrical power consumption of 10 watts.

EIS characteristics were performed for each wave-length in air at a set temperature of 450°C. The results are shown in the following figure.

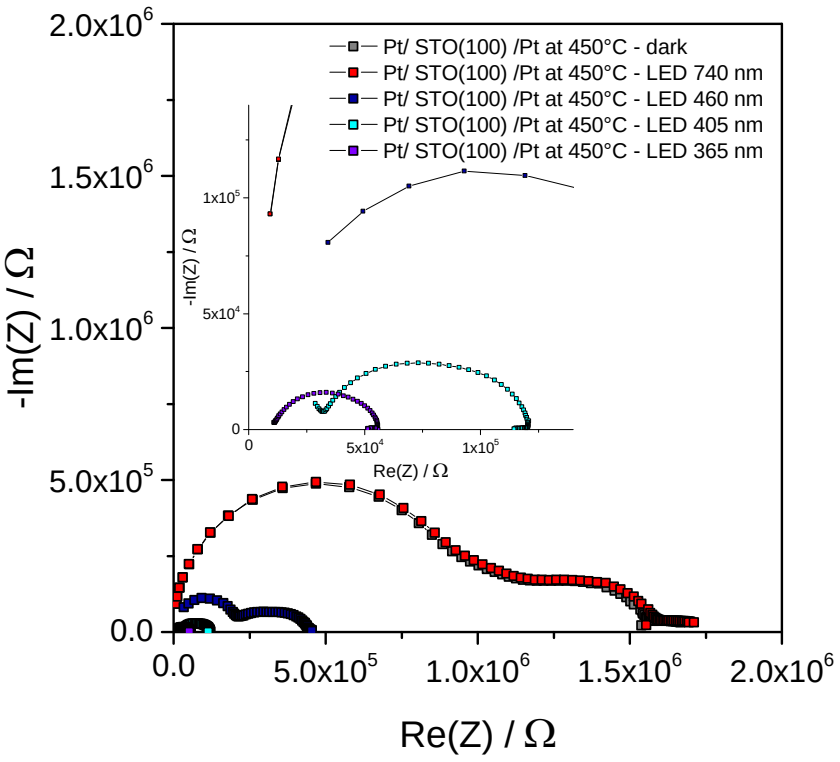

Figure 3.26: EIS measurements on Pt/ STO(100)/ Pt single crystal (GB_STO_08) in air at a set temperature of 450°C; in dark and with different types of LED sources.

In this experimental analysis the STO sample was contacted with a tip at top of the electrode and the other at the bottom. Each short-wave LED (460, 405 and 365 nm) effects a significant change in the resistance, *i.e.* between 365 nm and 460 nm LED in the order of magnitude. One can expect that under illumination with infrared (IR) radiation (740 nm) the photo-conductivity remains the same as in dark. Indeed, the overlapping of the impedance spectra in dark and under 740 nm – illumination has been achieved by temperature compensation with a ΔT of 4°C, *i.e.* 447°C in the case 740 nm.

It has been incidentally observed that **after illumination** with **short-wave radiation** the STO crystal is **not in chemical equilibrium**. Probably, photo generated charge carries (e^-) in the bulk lead to a stoichiometric change (δ) in concentration of oxygen vacancies ($V^{\bullet\bullet}$) and equilibrates with time. **The observed effect has been further investigated by G. Walch in his PhD thesis and will open a new potentially interesting scientific field**. In a first consideration, the effect has been supposed by interpreting of EIS measurement results as shown as follows.

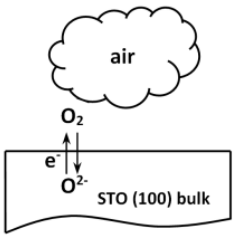

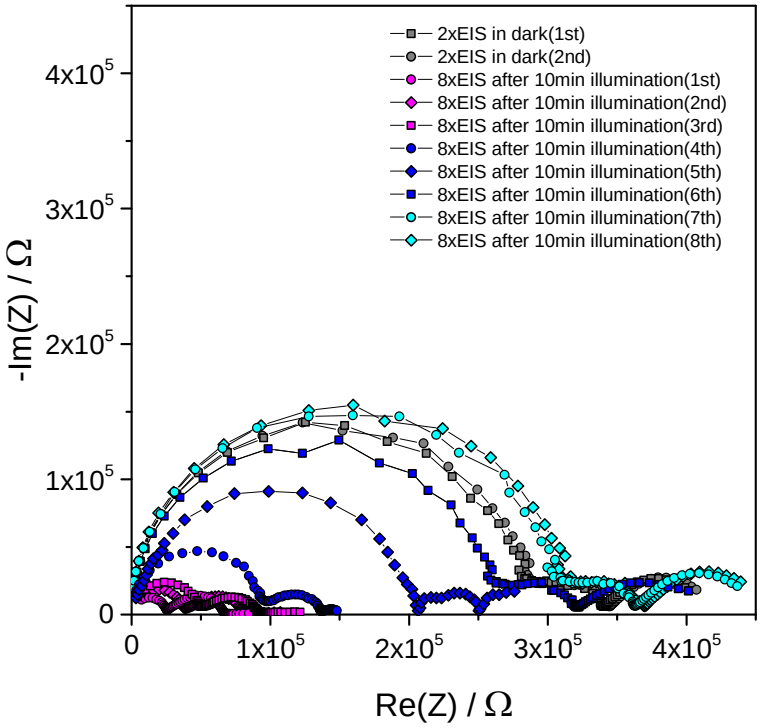

Figure 3.27: EIS measurements on Pt/ STO(100)/ Pt single crystal (GB_STO_09) in air at a set temperature of 450°C; the EIS measurement was performed as follows: (1) 2xEIS in dark, (2) 10 min illumination with 10W-LED/405 nm, and (3) LED-off; 8x EIS in dark.

The following method was applied: These EIS measurements were performed in I-Pot setup in air at a set temperature of 450°C (see Fig. 3.11). The experimental analysis was initiated with two impedance spectra in dark. After that, the Pt/ STO(100)/ Pt cell was illuminated with a wave-length of 405 nm by using a 10 W LED. In this period no EIS measurement was performed. In the following 8 impedance spectra were measured with a start frequency of 1 MHz and an end frequency of 5 mHz from –●– to –◇– . The initial state is more or less reached after the measurement sequence. The last impedance spectrum after illumination (8^{th}) does not exactly correspond with the initial EIS –■–. A reason for this could be that the sample was not completely equilibrated when the measurement was started.

In an analogous way this measurement was applied on a sample with a changed arrangement of electrodes, as shown in **Figure 3.24**. The Pt/ STO(100)/ Pt cell with the sample ID **GB_STO_08** is equipped with an interdigitated finger electrode. In the case before: the electrodes of the sample (GB_STO_09) 'see' the change in chemical composition of STO (100) in the entire bulk. Here, the interdigitated finger is laterally arranged at the surface.

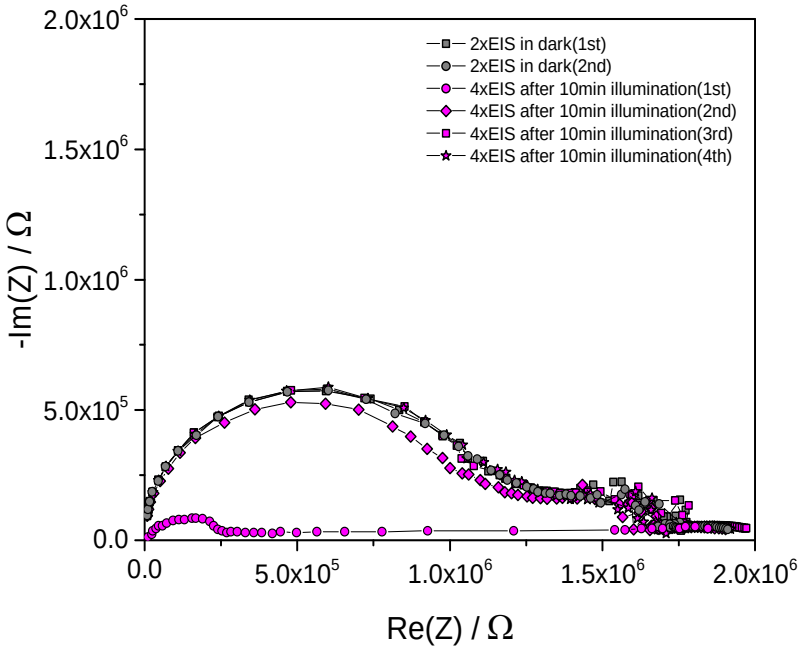

Figure 3.28: EIS measurements on Pt/ STO(100)/ Pt single crystal (GB_STO_08) in air at a set temperature of 450°C; the EIS measurement was performed as follows: (1) 2xEIS in dark, (2) 10 min illumination with 10W-LED/405 nm, and (3) LED-off; 4x EIS in dark.

After switch-off of the illumination the initial conditions are quickly reached. Obviously, the illuminated surface equilibrates quite fast. In other words: the chemical composition in STO single crystal near to the surface is homogenous after a short time of equilibration.

From a scientific point of view, the observed effect of a change in the chemical composition in the bulk of STO single crystal by illumination with a short-wave radiation is highly interested. A detailed experimental investigation is necessary to get a profound knowledge about these effects.

3.2.3 Investigation of $SrTiO_3$(100)/ $La_{0.8}Sr_{0.2}CrO_3$ heterojunction

The declared objective is to find a material system which is able to perform a photoelectrochemical reaction. That will be an absolute indispensable basic premise for driving an (solar-) photochemical energy conversion process. Nevertheless, the found photoactivity in STO single crystal and the pre-experimental investigation bring us closer to the desired goal. In addition to these results another material has been required to achieve a photo **induced voltage** and **current** which allow a **photoelectrochemical water-splitting** reaction. For this purpose *strontium-doped lanthanum chromite* has been identified as a promising candidate for such application.

3.2.3.1 Principles of perovskits

Strontium-doped lanthanum chromite, as well as $SrTiO_3$, exhibits the perovskite structure. By studying literature is has been decided to choose a dopant ratio for strontium of 10 and 20%. The base materials$La_{0.9}Sr_{0.1}CrO_3$ (LSCr91) and $La_{0.8}Sr_{0.2}CrO_3$ (LSCr82) was purchased from AMERICAN ELEMENT, USA.
The general chemical formula for perovskite compounds is ABO_3, where 'A' and 'B' are two cations of very different sizes. The term "perovkite structure" refers to a cubic structure [89]. Due to the different ionic radii of the cations the perovkite structure is expended to an *orthorhombic* crystal structure [90]. The ideal cubic-symmetry structure has the B cation in 6-fold coordination, surrounded by an *octahedron* of anions.

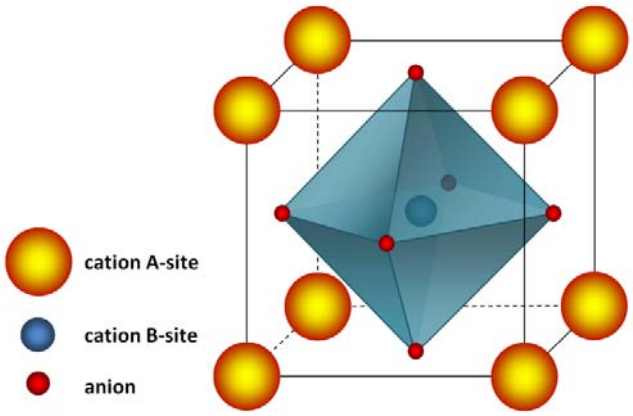

Figure 3.29: Ideal perovskite structure in the general formula ABO_3.

In particular, lanthanides, alkali metals and alkali earth metals are preferably at the site A, transition metals are at the site B. The condition of balanced charge in the crystal is fulfilled ($A^{2+}B^{4+}O_3^{-II}$).

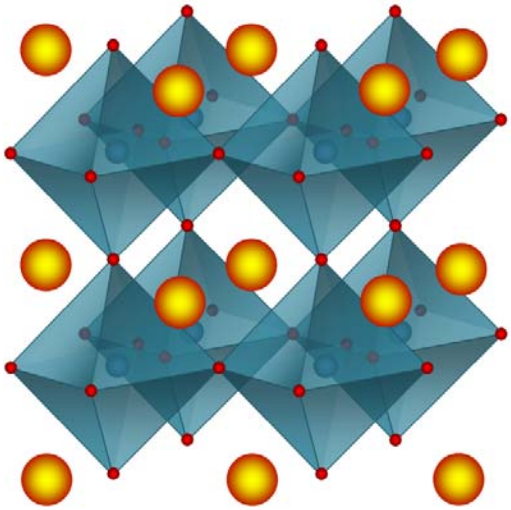

Figure 3.30: Ordered lattice composed of perovskite unit cells.

The physical properties are of great interest in materials science among perovskites include superconductivity, magneto resistance, ionic conductivity, and a multitude of dielectric properties, which are of great importance in microelectronics. For this application the photoelectrical properties play a major rule and are in the focus of attention.

In the case of $SrTiO_3$: Sr^{2+} is on the site A whereas Ti^{4+} is assigned to B-site. In the case of $La_{0.8}Sr_{0.2}CrO_3$: The situation here is more complex. Both, Sr^{2+} and La^{2+} are assigned to A-site and are distributed over the entire lattice in the ratio of 0.8/0.2, and Cr^{2+} is assigned to B-site.

3.2.3.2 Preparation of $SrTiO_3$(100)/ $La_{0.8}Sr_{0.2}CrO_3$ heterojunction

The proposed heterogeneous material system $SrTiO_3$(100)/$La_{0.8}Sr_{0.2}CrO_3$ (STO(100)/LSCr82) was realized successfully and generates photo voltage and current under illumination of short-wave radiation at high temperatures.

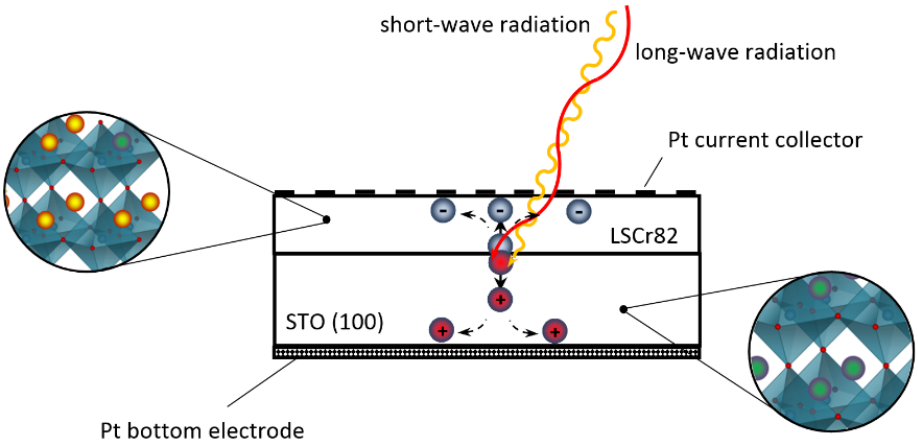

Figure 3.31: Sketch of STO(100)/LSCr82 heterojunction which is used as high temperature photovoltaic (HT-PV) cell.

The photoelectrochemical cell sketched in **Figure 3.31** was prepared as follows: In a first step, a 475 nm thin layer of $La_{0.8}Sr_{0.2}CrO_3$ (LSCr82) was deposited on a nominally undoped, *i.e.* intrinsic $SrTiO_3$ (100) single crystal. For that purpose, the substrates in the dimension (10x10x0.5) mm was purchased by CrysTec GmbH (Germany).Thin-films was prepared by pulsed laser deposition (PLD). It has been considered that the deposition time should be 30 min (18 000 pulses) with the laser operating at a pulse energy of 400 mJ (at the laser) and a repetition rate of 10 Hz. The LSCr82 material for thin-film deposition was obtained from AMERICAN ELEMENTS, LA, USA. The base materials with the patch numbers for LSCr82 (LOT# 1398312544-611) and for LSCr91

(LOT# 1398302547-702) were analyzed with X-ray diffraction (XRD) in order to confirm that the mixed-metal oxide materials are free from phase shift. After that proof, pellets were pressed and sintered at 1200°C for 12 h with a heating and cooling rate of 10°C min^{-1}. A scanning electron microscope (SEM) cross section image of a LSCr82 layer on $SrTiO_3$ is shown in **Figure 3.33**.

On top of this layer, a Pt current collector grid (stripe width: 10 µm, stripe distance: 40 µm and grid coverage of 23%) was prepared by sputter deposition and a subsequent lift-off photolithographic process.

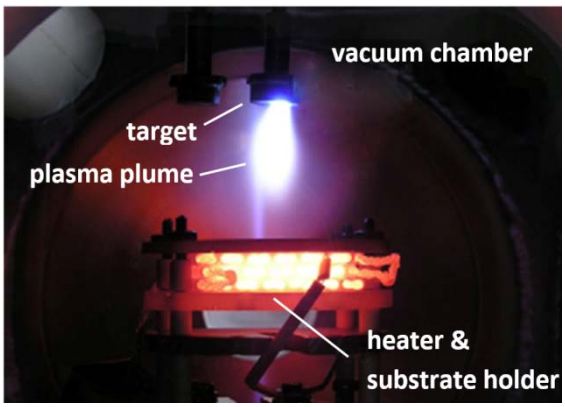

Figure 3.32: View in the vacuum chamber of an operating PLD for the deposition of thin-films.

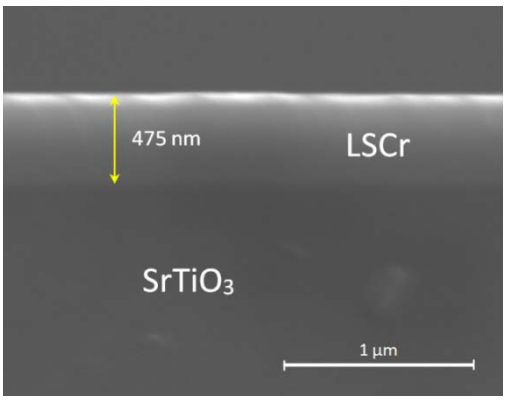

Figure 3.33: SEM cross section image of a 20% Sr doped $LaCrO_3$(LSCr82) layer deposited on a $SrTiO_3$ (100) single crystal.

3.2.3.3 Current-voltage characterization of $SrTiO_3$(100)/ $La_{0.8}Sr_{0.2}CrO_3$ heterojunction

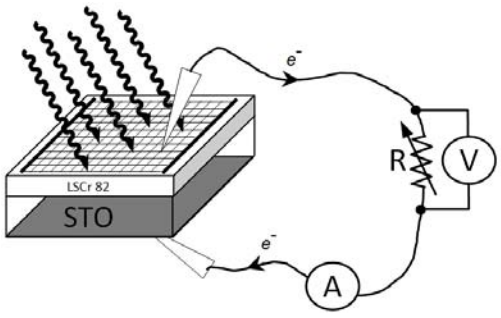

The STO(100)/LSCr82 heterojunction as sketched in Fig. 3.31 was characterized under illumination. For this purpose a DC analysis, *i.e.* current-voltage measurement was performed as shown beside. The cell was illuminated with a 1 W LED (electrical power) by emitting a wave-length of 405 nm. By characterization of open-circuit voltage U_{OC} and short-circuit current I_{SC}, the light source was switched on and off. *I-V* curves were measured at a set temperature of 400°C in air. For this analysis the STO(100)/LSCr82 cell with the sample ID GB_LCRO_23 was used.

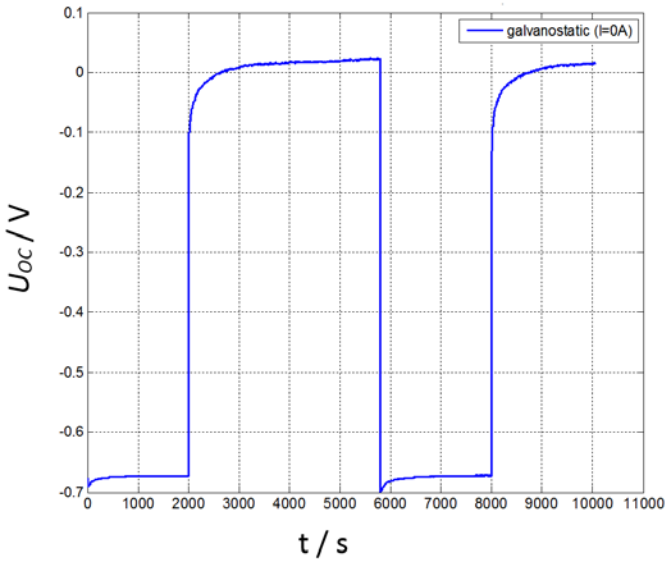

Figure 3.34: DC analysis: U_{OC} (galvanostatic I=0A) at a set temperature of 400°C in air under illumination with LED 1 W/405 nm by switching the light source on-off-on-off.

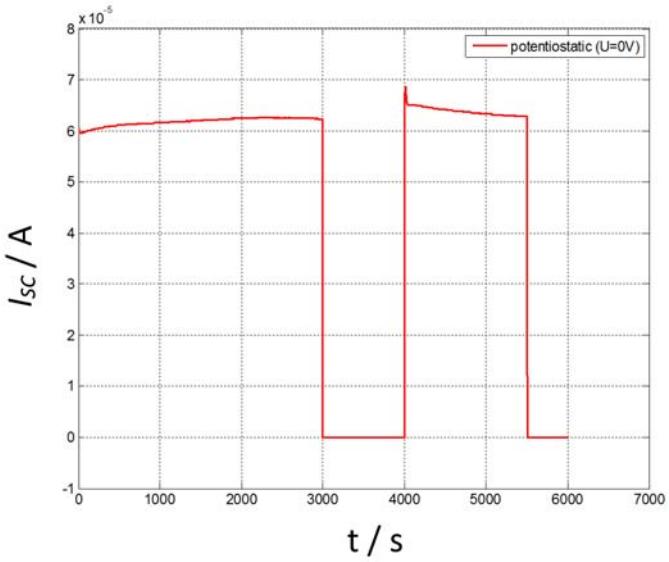

Figure 3.35: DC analysis: I_{SC} (potentiostatic U=0V) at a set temperature of 400°C in air under illumination with LED 1 W/405 nm by switching the light source on-off-on-off.

The results of *I-V* measurement show a U_{OC} of nearly 0.7 V and a maximum I_{SC} of 63 µA under illumination. It seems appropriate that, when the light source will provide a more intense illumination to drive a photo-electrochemical reaction.

For this purpose the setup has been modified as well as the structure of the cell. In more detail: the STO(100)/LSCr82 heterojunction cell will be used as a high-temperature photovoltaic (HT-PV) cell to provide voltage and current for performing a photoelectrochemical reaction. In this approach the HT-PV cell (10x10x0.5) mm with the sample ID **GB_LCRO_31** was packed on top of a solid oxide electrolyte. The

top electrode of the HT-PV cell is electrically contacted with the back side (bottom electrode) of the solid oxide electrolyte, as shown in **Figure 3.36**.

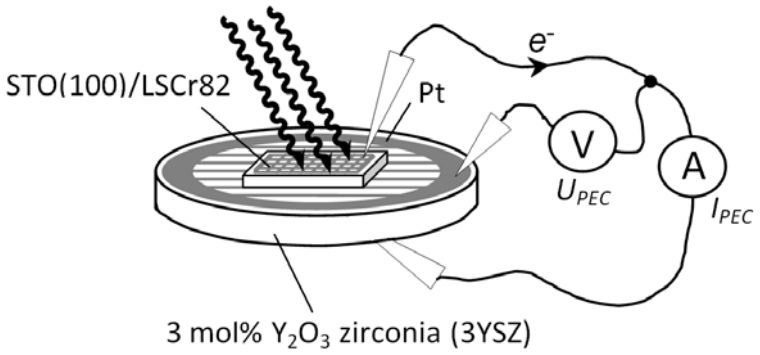

Figure 3.36: Cell structure of a HT-PV cell driven photoelectrochemical cell.

For the sketched cell in Fig. 3.36 a polycrystalline electrolyte substrate with 3 mol% Y_2O_3, 300 μm thickness, and 2 cm in diameter was used. The top and bottom electrode of the substrate was sputtered with Pt grid electrodes (Pt/YSZ/Pt). U_{PEC} and I_{PEC} represent the measured voltages and currents under operation conditions.

The cell sketched (see Fig. 3.36) has been characterized in air at 450, 500 and 550°C. For this analysis two different LED sources both with 10 W electrical power, the first one with 405 nm and the second one with 365 nm wave-length were used. The setup is shown in Figure 3.37.

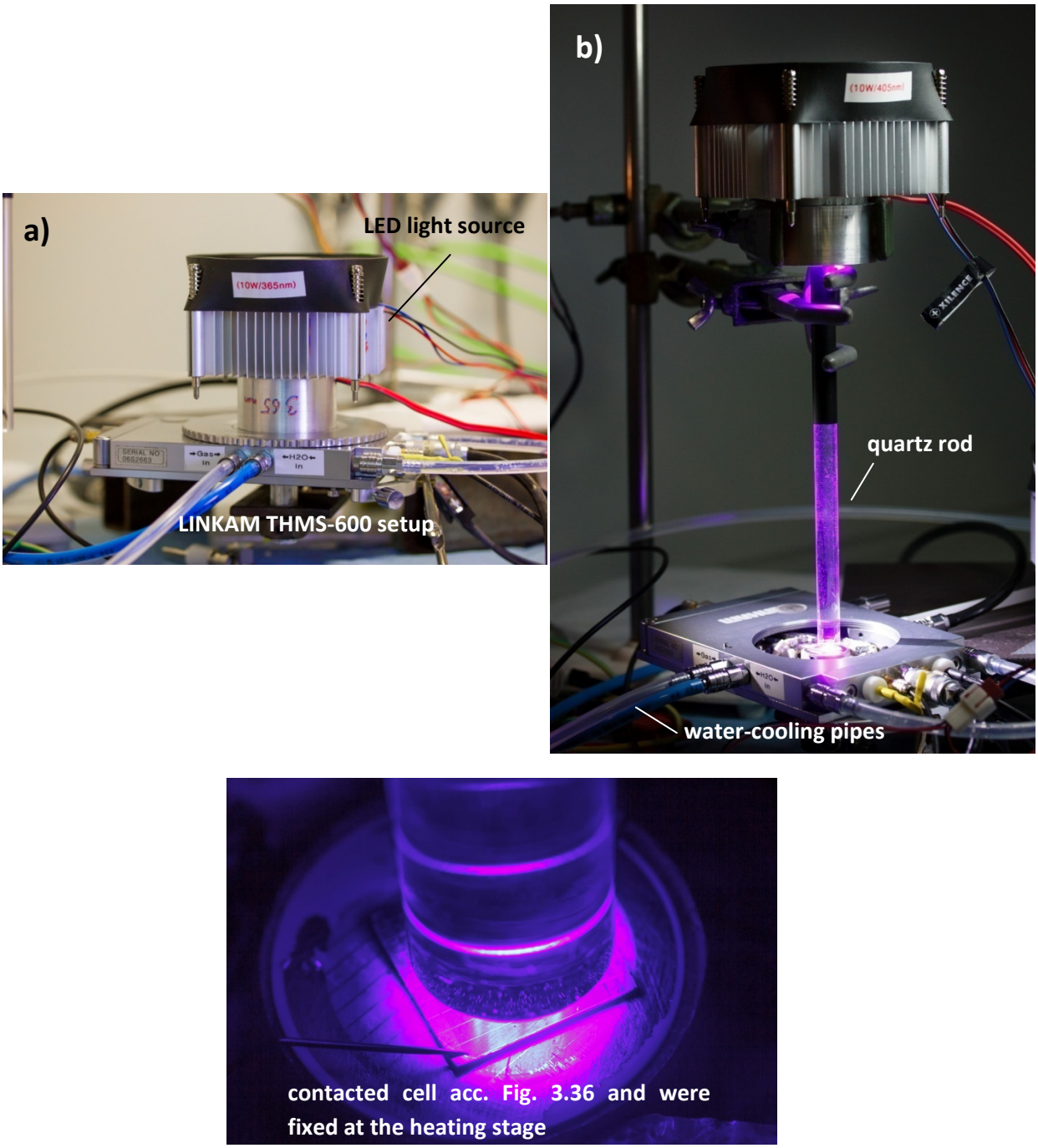

Figure 3.37: Analysis environment for DC characterization under illumination with a) fitted LED and b) by coupling the light through a quartz rod, in air at a set temperature of 450, 500 and 550°C.

The DC characterization of the sketched cell in Fig. 3.36 was performed with fitted LED light source (Fig. 3.37a) and by coupling the light beam through a quartz rod with 2 cm in diameter (Fig. 3.37b). In addition to that the *I-V* measurement carried out depending on temperature at 450, 500 and 550°C, and under illumination with wave-lengths of 405 and 365 nm).

In the following the result of *I-V* characteristics by using 10W-LED/405 nm with fitted light source and by coupling through a quartz rod were presented.

i) **with fitted LED (10 W/405 nm):**

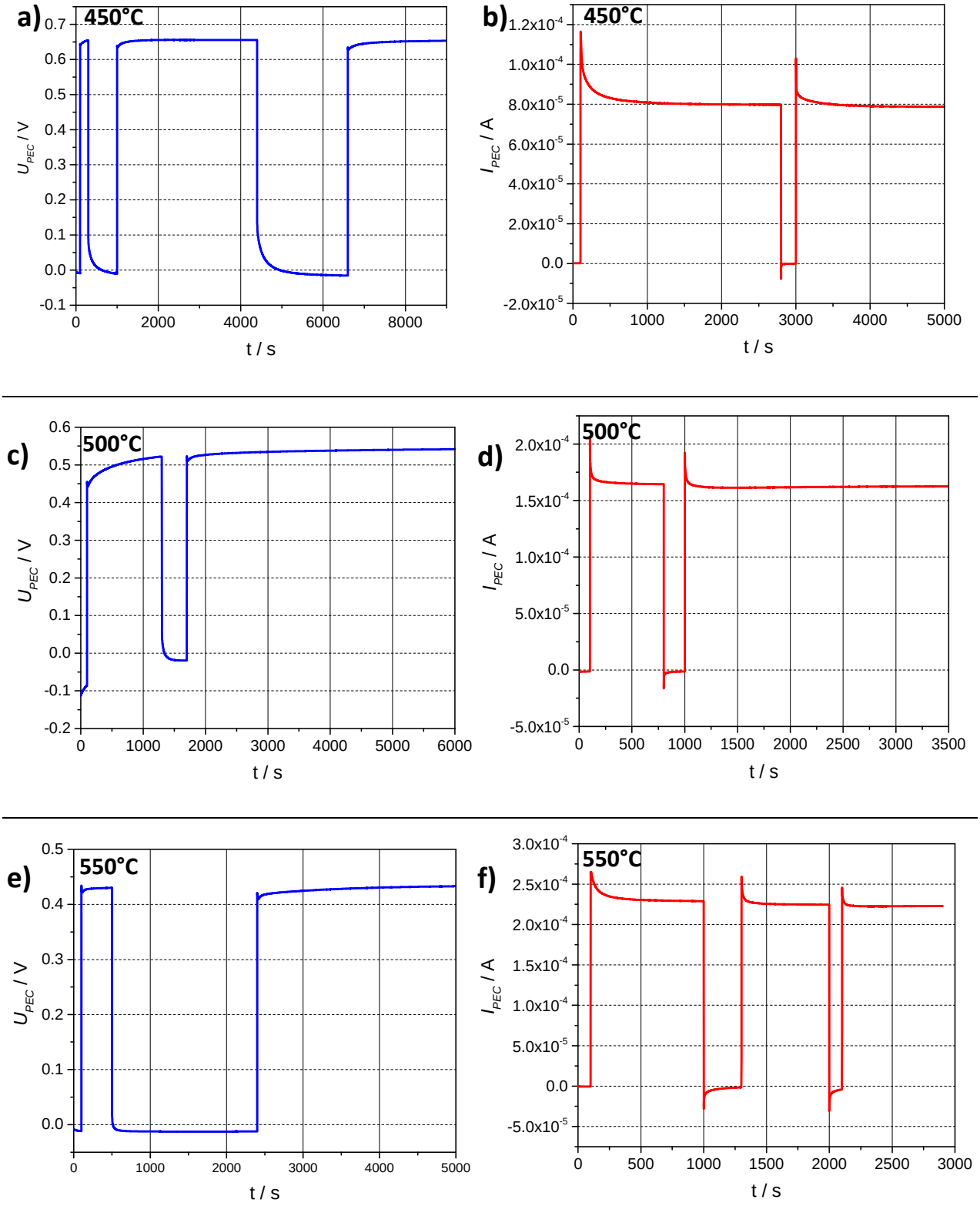

Figure 3.38: *I-V* characteristic of LSCr82/STO(100) + Pt/YSZ/Pt at a,b) 450°C, c,d) 500°C, and e,f) 550°C in air under illumination **with fitted** 10W-LED-405 nm **(acc. Fig. 3.37a)**.

ii) coupling the light beam with quartz rod:

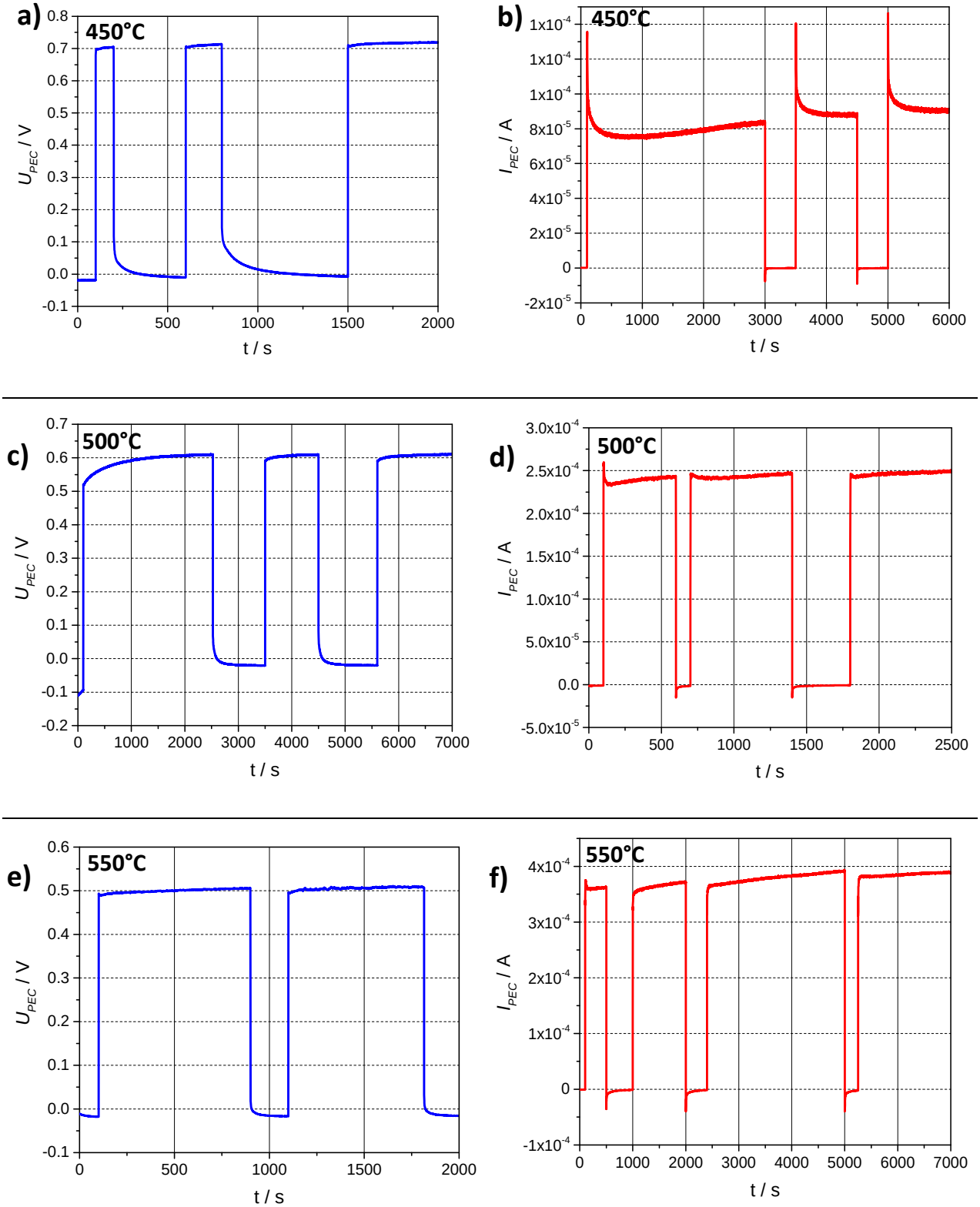

Figure 3.39: *I-V* characteristic of LSCr82/STO(100) + Pt/YSZ/Pt at a,b) 450°C, c,d) 500°C, and e,f) 550°C in air under illumination with 10W-LED-405 nm **by coupling the light through a quartz rod (acc. Fig. 3.37b)**.

***iii)* with fitted LED (10 W/365 nm):**

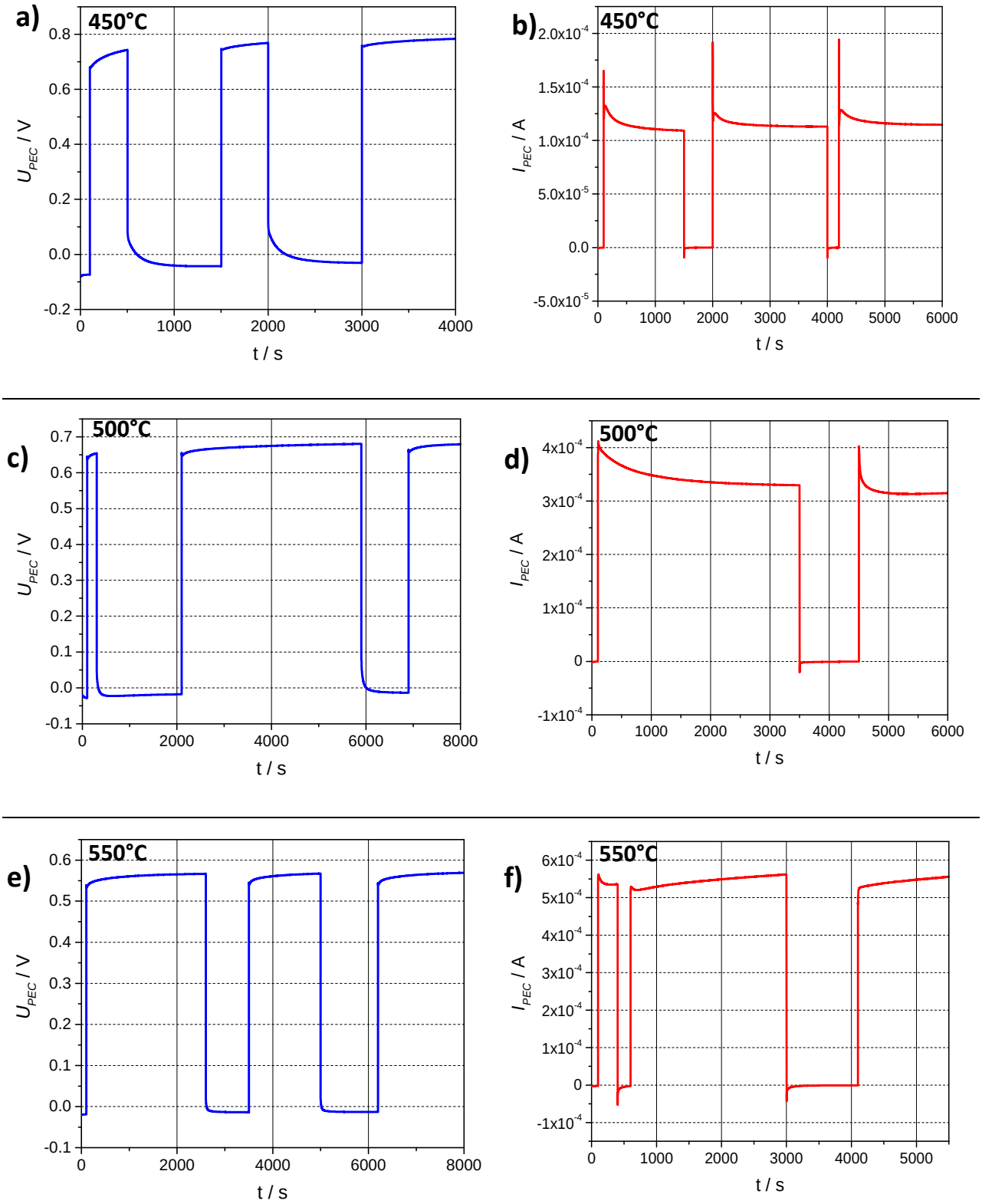

Figure 3.40: *I-V* characterization of LSCr82/STO(100) + Pt/YSZ/Pt at a,b) 450°C, c,d) 500°C, and e,f) 550°C in air under illumination **with fitted** 10W-LED-365 nm **(acc. Fig. 3.37a)**.

***iv)* coupling the light beam with quartz rod:**

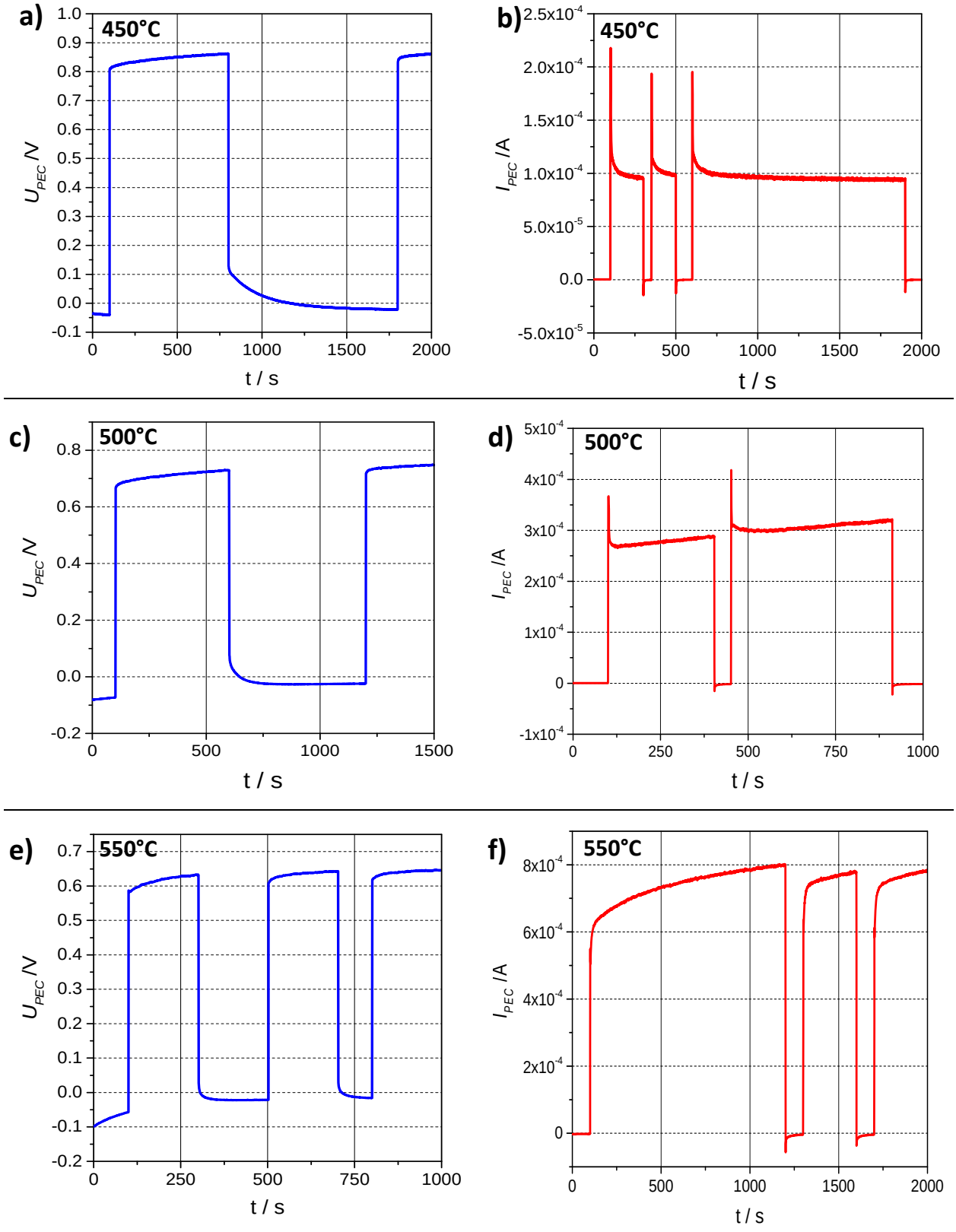

Figure 3.41: *I-V* characterization of LSCr82/STO(100) + Pt/YSZ/Pt at a,b) 450°C, c,d) 500°C, and e,f) 550°C in air under illumination with 10W-LED-365 nm **by coupling the light through a quartz rod (acc. Fig. 3.37b)**.

Table 3.1: Summarized results from *I-V* characterization under illumination with 10 W-LED/405 nm.

10 W-LED/405 nm				
	with fitted LED light source[3]		coupled light with quartz rod[4]	
Temperature °C	Voltage U_{PEC} V	Current I_{PEC} µA	Voltage U_{PEC} V	Current I_{PEC} µA
450	0.65	80	0.70	90
500	0.54	160	0.60	250
550	0.44	230	0.50	400

Table 3.2: Summarized results from *I-V* characterization under illumination with 10 W-LED/365 nm.

10 W-LED/365 nm				
	with fitted LED light source[3]		coupled light with quartz rod[4]	
Temperature °C	Voltage U_{PEC} V	Current I_{PEC} µA	Voltage U_{PEC} V	Current I_{PEC} µA
450	0.79	120	0.85	100
500	0.68	310	0.66	310
550	0.57	550	0.63	800

In **Table 3.1** and **Table 3.2** the results of *I-V* characterization in dependence with temperature and wave-length are summarized. The cell as sketched in Fig. 3.36 is under operating condition when the top of the HT-PV cell is connected with the bottom electrode of the solid oxide electrolyte. U_{PEC} and I_{PEC} summarized in Tab. 3.1 and Tab. 3.2 represent voltage and current under operation conditions.

At each temperature, by using 365-nm-LED it has been shown that U_{PEC} is approx. 10 mV higher than under illumination with 405-nm-LED. As expected, U_{PEC} is decreasing with temperature whereas I_{PEC} is increasing with temperature. Although the large distance by coupling the light through the quartz rod the resulting voltage and current is slightly higher than with fitted LED light source.

[3]Setup according Fig. 37a

[4]Setup according Fig. 37b

3.3 The high-temperature Photoelectrochemical Cell (SOPEC)

The previous scientific work provided the basis for photoelectrochemical energy conversion processes. In a first approach such process should be realized by demonstrating an UV-driven oxygen pumping process. For this purpose the HT-PV driven solid oxide photoelectrochemical cell as sketched in Fig. 3.36 was slightly adapted. In addition to that a setup with separated gas chambers was designed and constructed for the demonstration of the analytical proof.

3.3.1 Design of experimental setup

The setup is following the concept of a **tubular flow reactor** with **two separated gas chambers**. One gas chamber is isolated from ambient, *i.e.* reaction zone with adjustable gas atmospheres. For simplification from a manufacturing point of view the second gas chamber is open towards outside. The thermal energy required for the process is provided by a tubular furnace in which the two corundum pipes are submerged. The photoelectrochemical cell is fixed between the corundum pipes. The several parts of the tubular reactor are shown as follows:

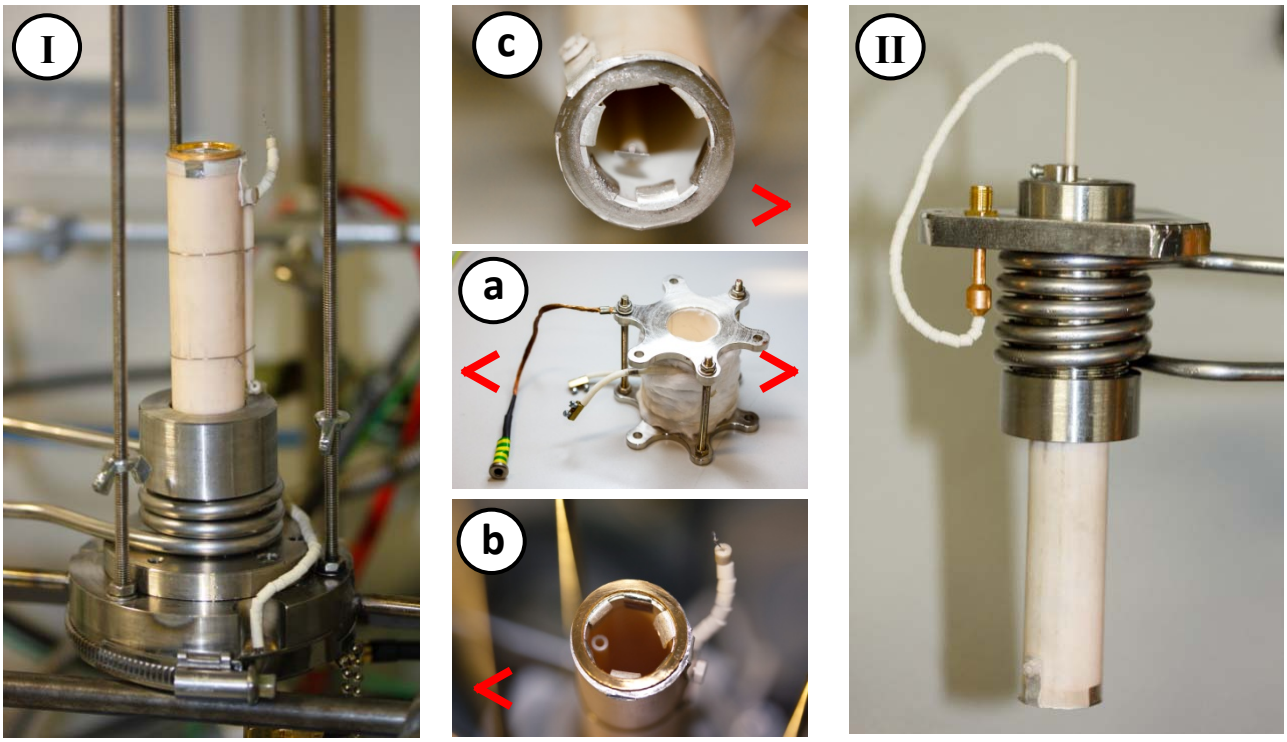

Figure 3.42: Several parts of the SOPEC tubular reaction (SOPEC-RR-V1); consisting of I) the bottom part with adjustable gas atmospheres via b) gas inlet and outlet, II) the upper part with c) electrical contacting, and a) the electrical heater.

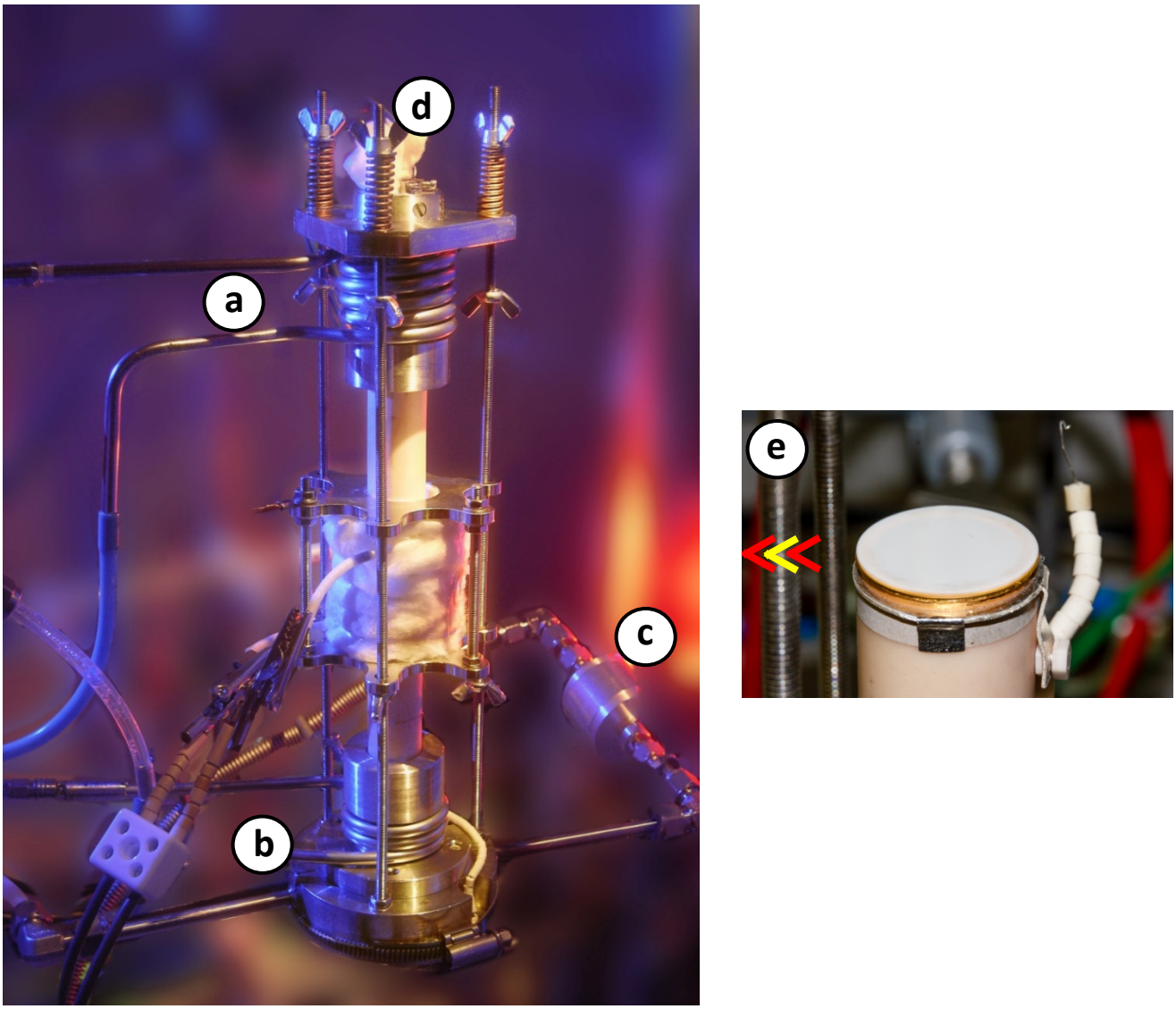

Figure 3.43: SOPEC-RR_V1 tubular reactor in assembled state with cooling system on a) the top part and b) the bottom part, c) an oxygen probe for analytical investigation, and d) mouth for introducing the light with a quartz rod, electrical contacting and thermocouple; e) the cell is fixed between two corundum (Al_2O_3) tubes.

3.3.2 Structure of SOPEC cell and measurement arrangement

The solid oxide photoelectrochemical cell is composed of a **high-temperature photovoltaic** (HT-PV) part and an **electrochemical** part. As already mentioned, the HT-PV cell consist of a heterogeneous material system of strontium titanate single crystal (STO 100) and a thin-film of 20 % strontium doped lanthanum chromite (LSCr82). This STO(100)/LSCr82 heterojunction cell with the dimension (10x10x0.5) mm is packed on a electrochemical cell. For this purpose a commercial yttria stabilized zirconia substrate (Ø20x0.3) mm with 3 mol% Y_2O_3 is used. Both sides of

the YSZ substrate are sputtered with Pt grid electrodes at which porous $La_{0.6}Sr_{0.4}FeO_{3-\delta}$ (LSF64) are brushed and sintered. The composed SOPEC cell is sketched as follows:

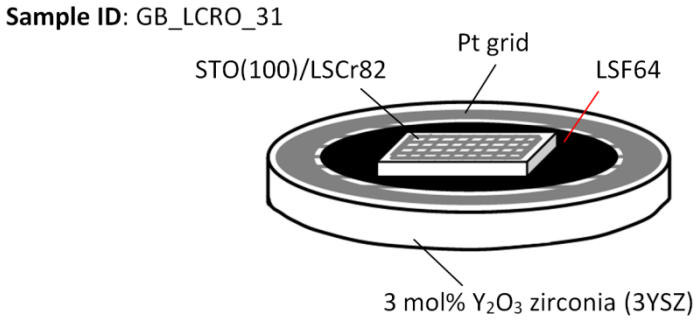

Figure 3.44: Composition of the SOPEC cell with the sample ID: GB_SOPEC_V1.6.

The rear side of the SOPEC cell (as sketched in **Figure 3.44**) is identical with the front; but without the HT-PV cell.

This SOPEC cell is fixed in a tubular pipe reactor such that two different gas compartments result, see Fig. 3.43e. At temperatures between 400 and 500 °C, the SOPEC cell is illuminated by UV light (365 nm) and the electrical performance is investigated, together with chemical effects (oxygen pumping monitored by oxygen partial pressure changes). Voltages are always measured between the LSCr82 top electrode and the shared LSF64 electrode, either without connection between top and SOPEC cell bottom electrode (then indicated by symbol U_{PV}) or with an external short circuit (SC), *i.e.*, under PEC operating conditions (denoted U_{PEC}), see **Figure 3.45**. In the latter case, the voltage of the EC cell part (U_{EC}) equals the measured voltage U_{PEC} due to the external short circuit, *i.e.*, U_{PEC} (=U_{PV}) = U_{EC} (all voltages with positive sign). Currents are either I_{PEC} indicating the short-circuit current of the entire SOPEC cell or I_{PV} when only investigating the HT-PV part of the cell.

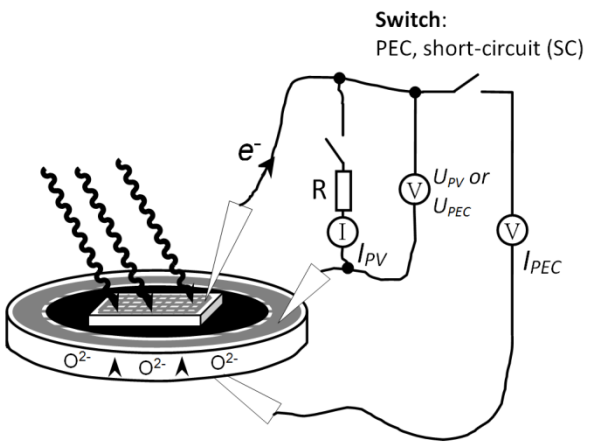

Figure 3.45: Sketch of investigated SOPEC cell with the measurement arrangement.

The short-circuit current I_{PEC} has to be ionic in the zirconia electrolyte and thus electrochemical reactions have to take place at the two LSF64 electrodes of the illuminated SOPEC cell. In the given cell this is 1/2 O_2 + 2e^-→O^{2-}at the bottom LSF electrode and the reverse reaction at the shared LSF64 electrode.

The oxygen ion conduction through the YSZ electrolyte is realized by introduction of dopants. In such case yttria (Y_2O_3) is inserted. The basic idea of defect chemical considerations is a replacement of lattice atoms. In this particular case, a replacement of a tetravalent cation (Zr^{4+}) with a trivalent cation (Y^{3+}) must lead to oxygen vacancies. Such replacement of lattice cations is schematically shown in **Figure 3.46**.

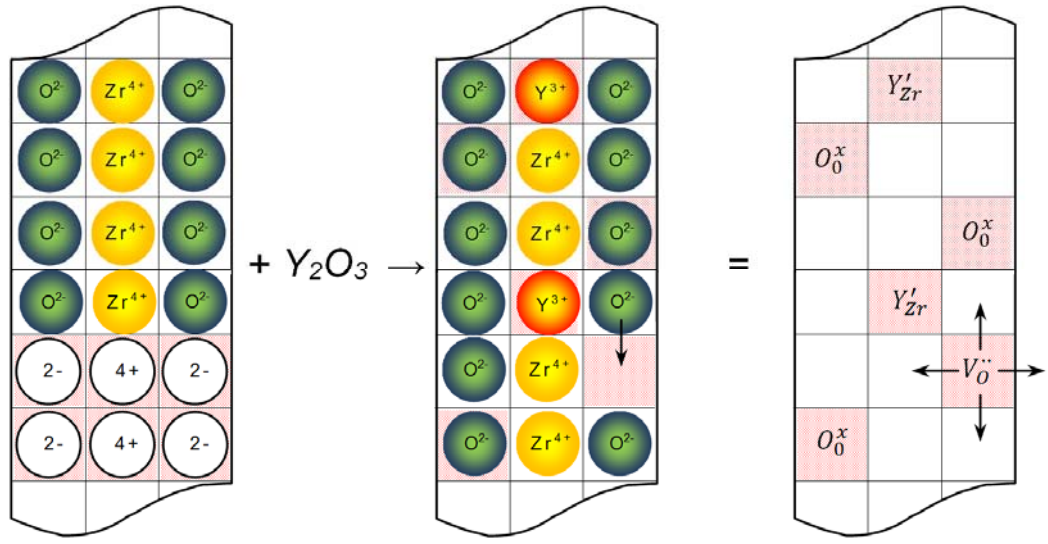

a) ideal charge without chemical defects

b) real charge after introduction of chemical defects

c) corresponding charge by Kröger-Fink notation

Figure 3.46: Scheme of defect chemistry in yttria stabilized zirconia (YSZ).

Theses vacancies would be viewed as defects in the $Y_2O_3(ZrO_2)$ framework, carrying an effective positive charge of 2 (see Eq. 3.8), by using the KRÖGER-FINK notation [78], are denoted by $V_0^{\bullet\bullet}$

$$Y_2O_3(ZrO_2) \rightarrow 2Y'_{Zr} + 3O_0^x + V_0^{\bullet\bullet}, \tag{3.8}$$

leading to oxygen incorporation, as given

$$½O_2 + V_0^{\bullet\bullet} \leftrightarrow 0_0^x + 2h^{\bullet} \tag{3.9}$$

3.3.3 Characterization of SOPEC cell under operation condition

The SOPEC cell as shown in Fig. 3.44 is characterized in the tubular reactor SOPEC-RR_V1 at temperatures between 400 and 500°C in 25°C temperature steps. The UV light (365 nm) is switched on and off. During this measurement process voltages (U_{PEC}, $U_{PV,OC}$) and current (I_{PEC}) is analyzed. For a profound characterization, the arrangement of the measurement (see Fig. 3.45) has allowed the possibility to measure the voltage under operation condition U_{PEC} and under open-circuit condition $U_{PV,OC}$.

In the following the results of *I-V* characterization are shown:

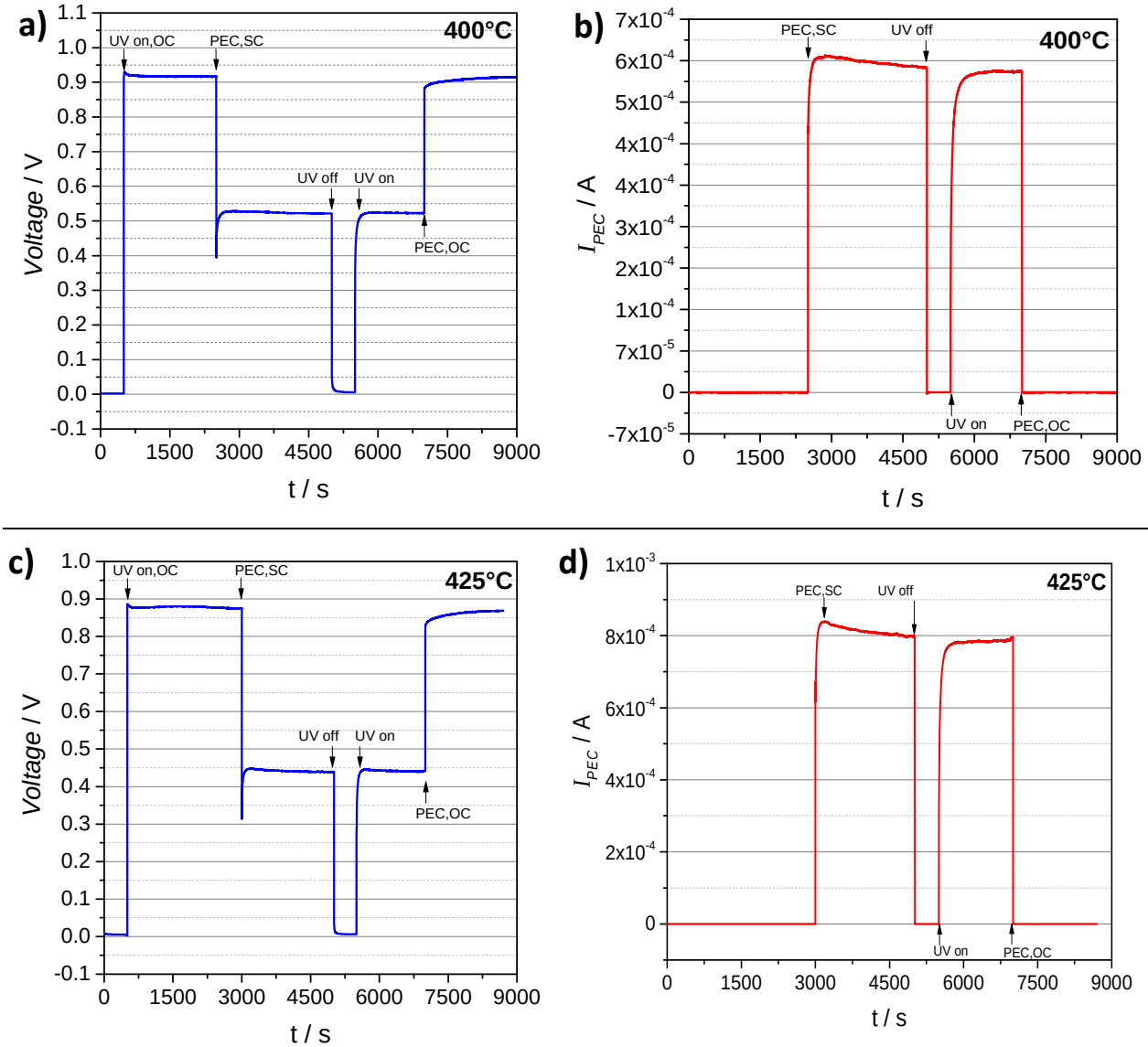

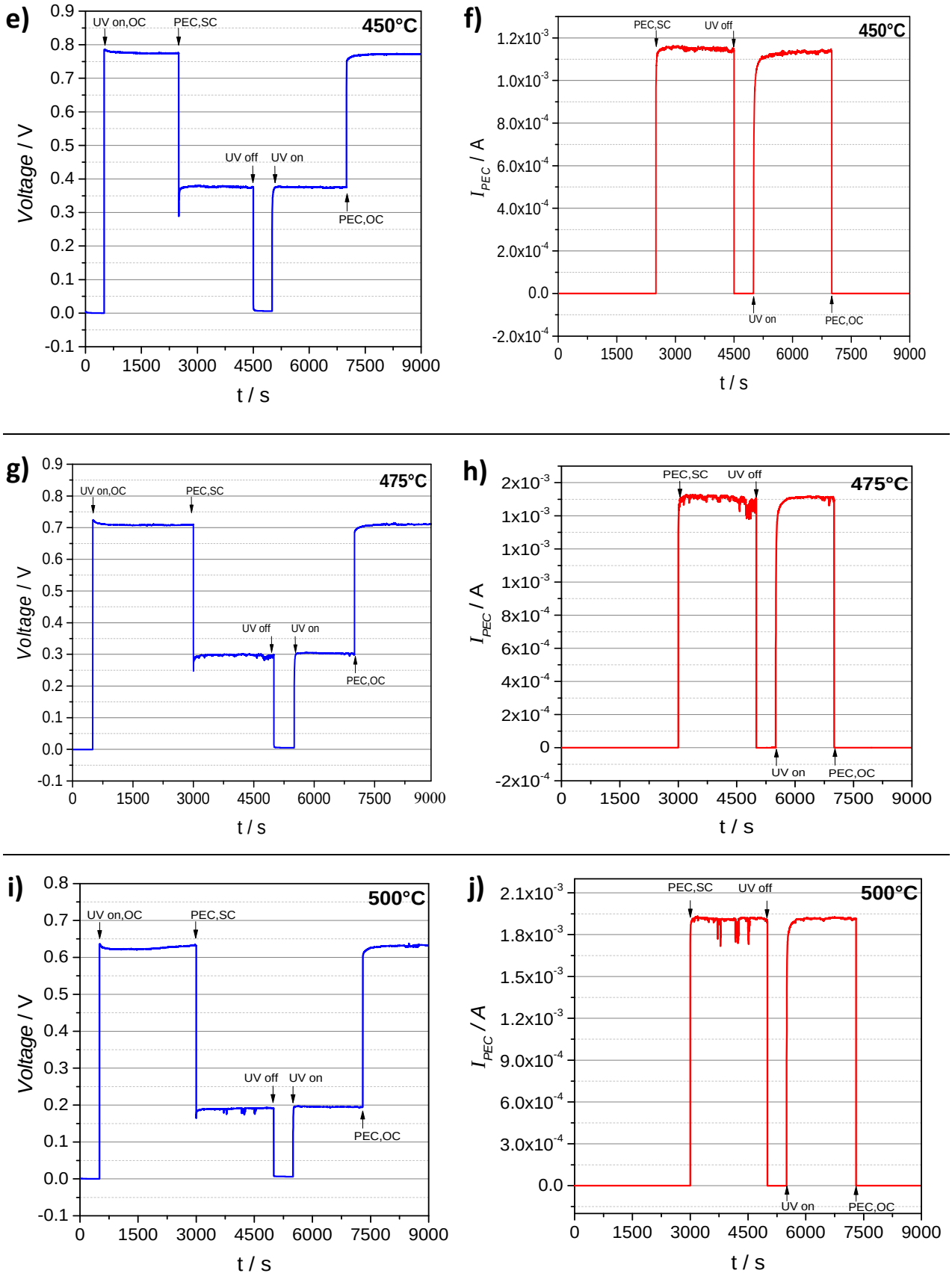

Figure 3.47: a, c, e, g, i) Open circuit voltage ($U_{PV,OC}$) after switching UV on and voltage under working condition of the SOPEC cell (U_{PEC}) after short-circuiting the illuminated PEC cell at a) 400 °C, c) 425 °C, e) 450 °C, g) 475 °C and i) 500 °C in symmetric gas atmospheres, UV on–off is indicated. b, d, f, h, j) corresponding current of the PEC cell (I_{PEC}).

In addition to that, for a better understanding of the solid oxide photoelectrochemical cell, the HT-PV part of the SOPEC cell is also characterized by determining its I–V curves under illumination, *i.e.* measuring U_{PV} and I_{PV} for different loads and temperatures as shown in **Figure 3.49**. For that purpose to obtain an *I-V* curve, a step less adjustable resistance, *i.e.* a potentiometer, is used to simulate an electrical load (see **Figure 3.48**).

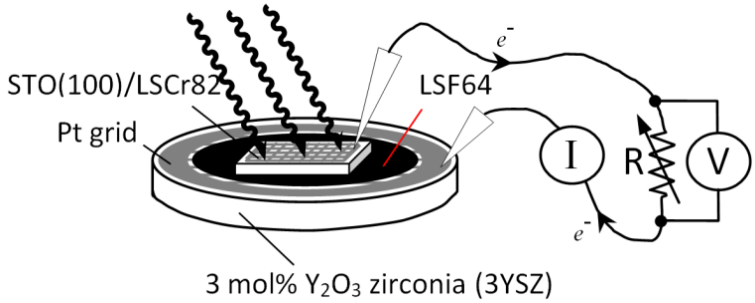

Figure 3.48: Measurement arrangement for *I-V* characterization.

That measurement was performed in-situ at the SOPEC cell by using the electrical test setup (see Fig. 3.48); connected with the HT-PV part.

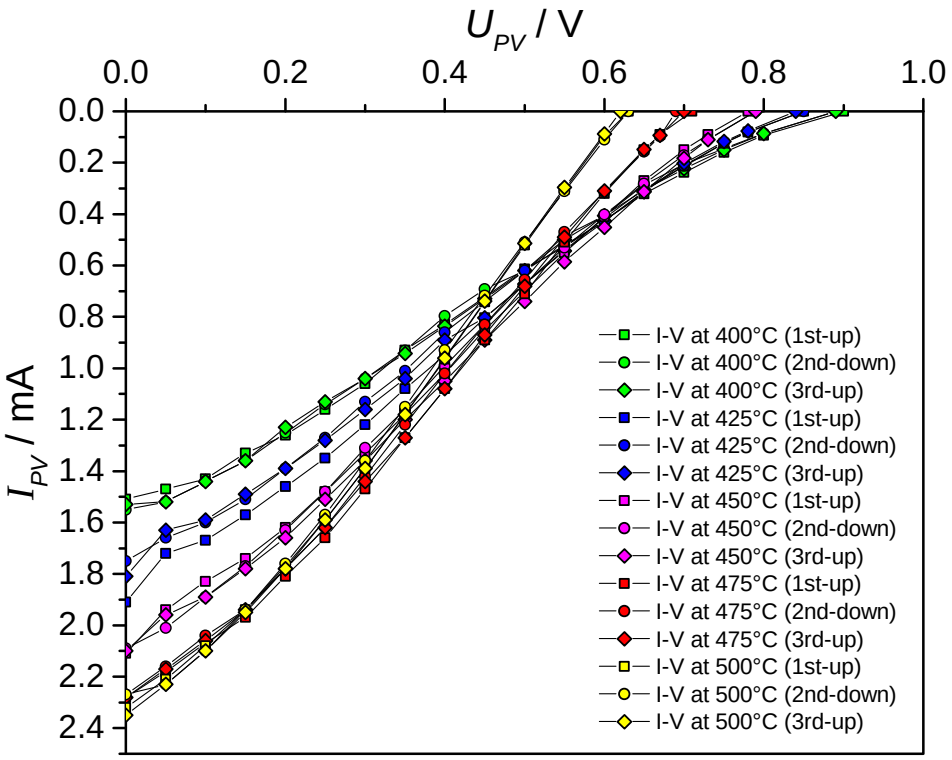

Figure 3.49: *I–V* characteristics of the HT-PV cell solely, obtained by measuring U_{PV} and I_{PV} for different electrical loads and temperatures from 400°C to 500°C.

By obtaining the *I-V* characteristic; for each curve it was started (1st - up) at 0 V, *i.e.* at short-circuit condition (= $I_{PV,SC}$), and due to increasing of ohmic resistance up to open-circuit condition ($U_{PC,OC}$). At next, the other way round (indicated with 2nd - down), and finally once again to open-circuit condition (3rd - up).

The results of the characterization under operation condition and under open-circuit condition are summarized as follows:

Table 3.3: Summarized results of voltages and currents of the HT-PV cell and of the SOPEC cell from 400 to 500°C.

	HT-PV cell		SOPEC cell	
Temperature °C	Voltage $U_{PV,OC}$ V	Current $I_{PV,SC}$ mA	Voltage U_{PEC} V	Current I_{PEC} mA
400	0.89	1.51	0.53	0.58
425	0.84	1.81	0.44	0.79
450	0.78	2.09	0.37	1.17
475	0.70	2.27	0.30	1.50
500	0.62	2.32	0.19	1.95

For a brief discussion, the summarized results of **Table 3.3** are shown in **Figure 3.50** and **Figure 3.51.**

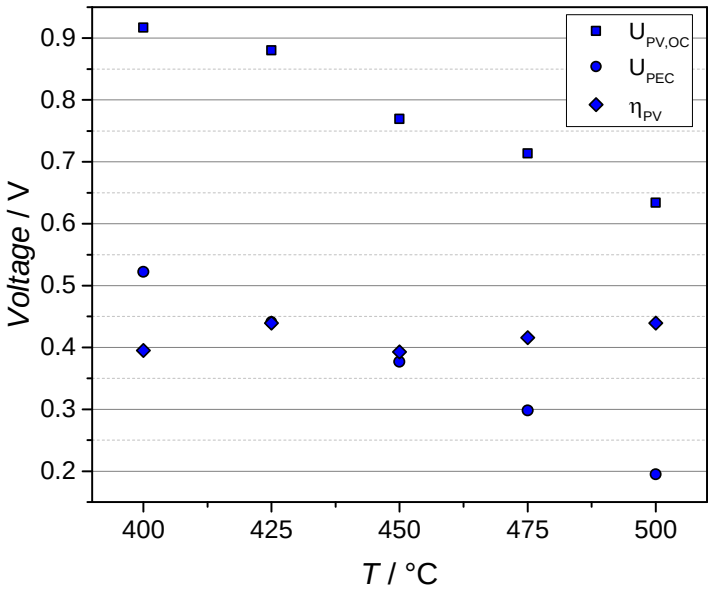

Figure 3.50: Open circuit voltages ($U_{PV,OC}$) of the HT-PV cell, voltage loss in the HT-PV cell (η_{PV}) and voltages U_{PEC} of the operating SOPEC cell at temperatures from 400 to 500°C in symmetric gas atmospheres.

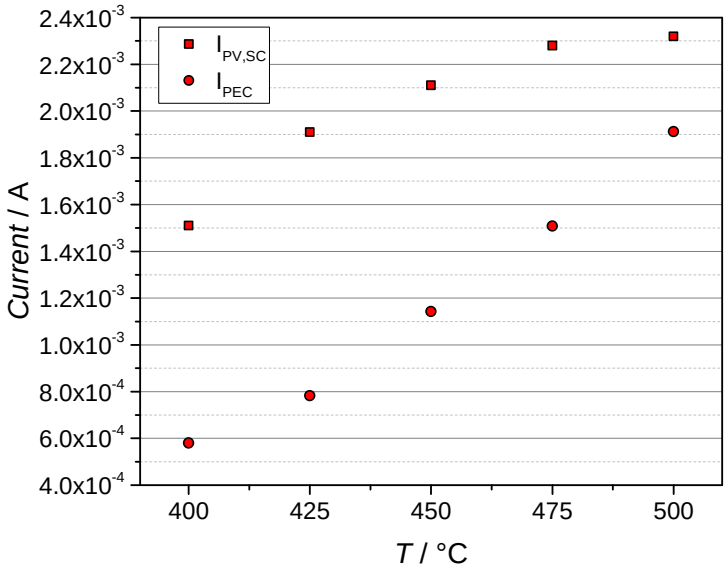

Figure 3.51: Short-circuit currents of the PV cell solely ($I_{PV,SC}$) and of the PEC cell (I_{PEC}) at temperatures from 400 to 500°C in symmetric gas atmospheres.

As already discussed, the open circuit voltage $U_{PV,OC}$ decreases with increasing temperature (see Fig. 3.50), while the short-circuit current $I_{PV,SC}$ increases (see Fig. 3.51). The difference between $U_{PV,OC}$ and U_{PEC}, on the other hand, is the voltage loss in the PV cell (η_{PV}) and can be associated with its internal resistance ($\eta_{PV} = U_{PV,OC} - U_{PEC}$), see Fig. 5.50.

Hence, the maximum power output is rather temperature independent at 0.33–0.45 mW between 400 and 500°C. A detailed mechanistic understanding of the PV cell and its *I–V* curve is beyond the scope of this thesis; it may include not only the photoactive junction but also an ohmic and an additional nonlinear serial resistive contribution.

3.3.4 Experimental proof of UV-driven oxygen pumping

The results of recent studies inspire confidence that the experimental proof of UV-light driven oxygen pumping by using the SOPEC cell will succeed. However, this would require that the condition for the gas tightness is extremely high. A great importance will be attached to the clamping of the SOPEC cell itself. For that purpose some essential conditions must be satisfied.

Figure 3.52: Sealing ring in the evacuated part of the tubular reactor.

Figure 3.53: Sealing ring in the open part of the tubular reactor.

It must be ensured that the sealing surface has to be absolutely smooth. The sealing ring consists of gold (Au). There are several reasons for this: firstly, Au is highly corrosion-resistant at high temperatures, secondly Au has tensile properties at high temperatures which serve to improve the tightness, and thirdly, Au is electrically conductive. The Au-sealing as shown in **Figure 3.54** performs the function of tightness and of electrical contacting, whereas the sealing ring in the upper part only handle the electrical contacting of the cell (see **Figure 3.55**). For reasons of design simplification, the upper part of the tubular reactor (SOPEC-RR-V1) is open towards outside.

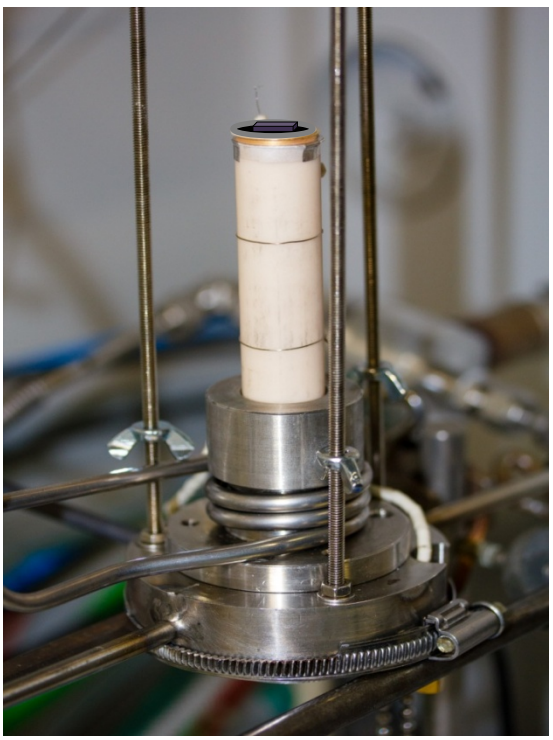

Figure 3.54: Bottom part of SOPEC-RR-V1with the positioned SOPEC cell.

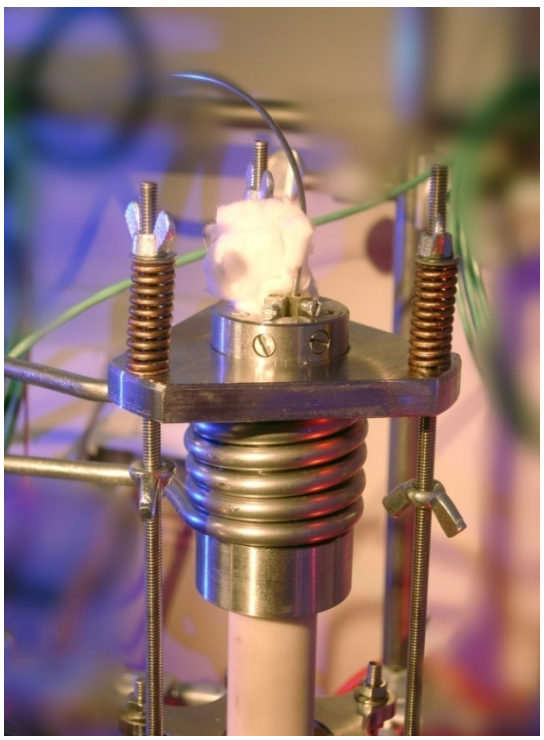

Figure 3.55: Upper part of SOPEC-RR-V with guiding rods, pressure springs and screws.

In Fig. 3.54, the SOPEC-RR-V1 is prepared for assembling as shown. The positioned SOPEC cell will be clamped with the upper part of the tubular reactor by screwing (see Fig. 3.55). In this context it has to be considered that the clamping force must be distributed equally over three screws.

Oxygen pumping against a higher oxygen partial pressure rather than water splitting is employed to demonstrate the potential of the SOPEC cell for conversion of radiation energy into chemical energy. Accordingly, illumination of the SOPEC cell is also performed for asymmetric gas supply, *i.e.* for the HT-PV cell in the upper part (see Fig. 3.55) being in air and the bottom part of the electrochemical cell (see Fig. 3.54) being in nitrogen with approx. 600 ppm remaining oxygen (measured by an oxygen sensor). The HT-PV cell is not affected by the gas change in the bottom compartment, but the EC cell now exhibits an open circuit voltage of 92–98 mV, depending on temperature (**Figure 3.56** a,d,g). This is in accordance with the expected Nernst voltage U_N between ambient air and 600 ppmO_2 (96.8 mV at 500°C). Upon illumination under short-circuit condition, again a substantial voltage U_{PEC} and a current I_{PEC} up to 1 mA at 500 °C are found (Figure **3.56** b,e,h).The measured short-circuit current I_{PEC} leads to pumping of oxygen from the low partial pressure side (oxygen fraction) f_{O2} of ≈600 ppm O_2 in 1 bar gas) to the high partial pressure side (≈20% O_2 in 1 bar gas). **Figure 3.56** c,f,i shows that the oxygen content in the low pressure compartment, measured by the oxygen sensor at the outlet, substantially decreases upon UV light. An oxygen fraction of 480 ppm is reached at 400°C, 400 ppm at 450°C and almost 300 ppm at 500°C.

In the following **Figure 3.56**, the results of the photoelectrochemically driven oxygen pumping experiment performed in asymmetric gas atmospheres at i) 400°C, ii) 450°C and iii) 500°C with indicated UV on–off sequences are shown:

i) 400°C

a)

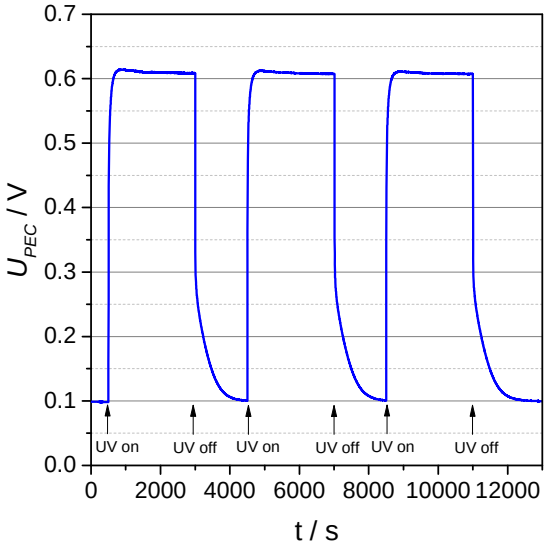
U_{PEC} / V
0.7
0.6
0.5
0.4
0.3
0.2
0.1
0.0
UV on
UV off
UV on
UV off
UV on
UV off
0
2000
4000
6000
8000
10000
12000
t / s

b)

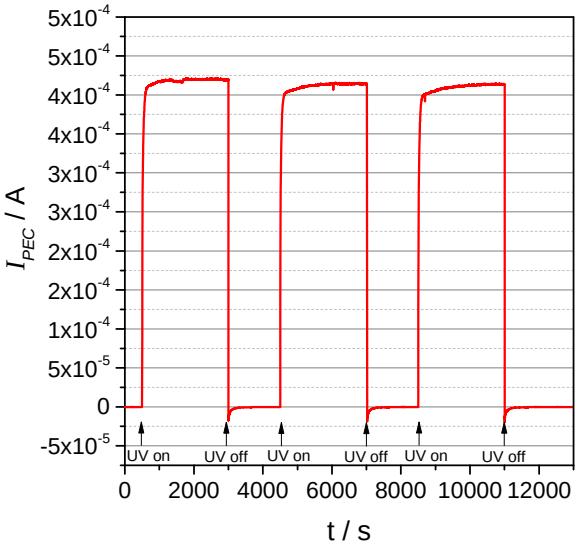
I_{PEC} / A
5x10^{-4}
5x10^{-4}
4x10^{-4}
4x10^{-4}
3x10^{-4}
3x10^{-4}
2x10^{-4}
2x10^{-4}
1x10^{-4}
5x10^{-5}
0
-5x10^{-5}
UV on
UV off
UV on
UV off
UV on
UV off
0
2000
4000
6000
8000
10000
12000
t / s

c)

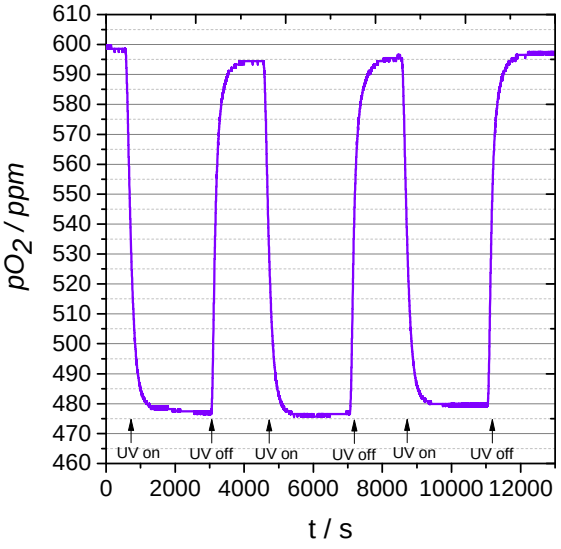
pO_2 / ppm
610
600
590
580
570
560
550
540
530
520
510
500
490
480
470
460
UV on
UV off
UV on
UV off
UV on
UV off
0
2000
4000
6000
8000
10000
12000
t / s

***ii*) 450°C**

d)

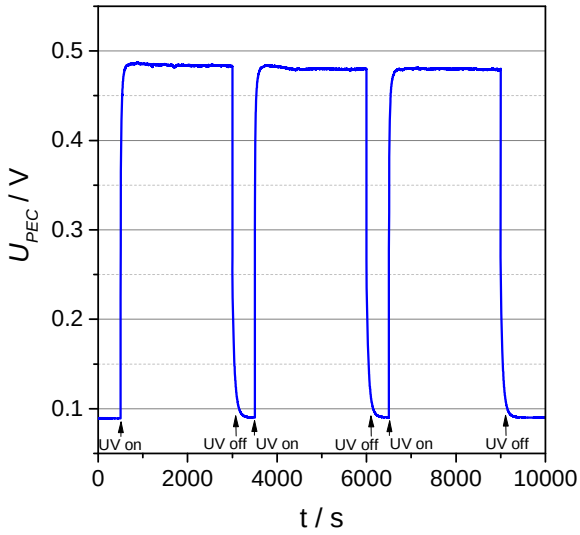
0.5
0.4
0.3
0.2
0.1
U_{PEC} / V
UV on
UV off
UV on
UV off
UV on
UV off
0
2000
4000
6000
8000
10000
t / s

e)

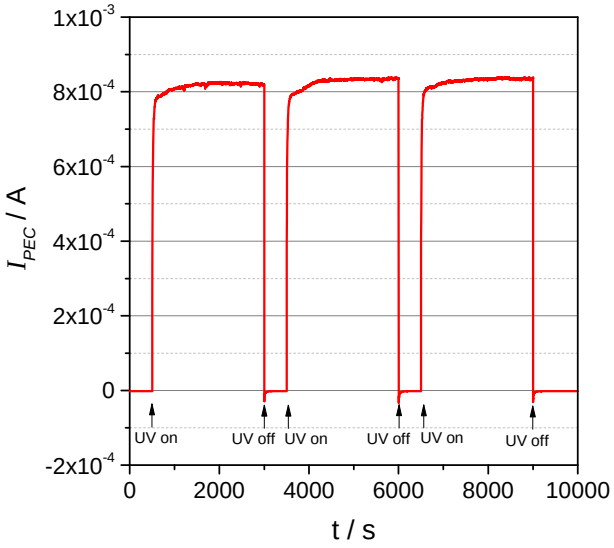
1x10^{-3}
8x10^{-4}
6x10^{-4}
4x10^{-4}
2x10^{-4}
0
-2x10^{-4}
I_{PEC} / A
UV on
UV off
UV on
UV off
UV on
UV off
0
2000
4000
6000
8000
10000
t / s

f)

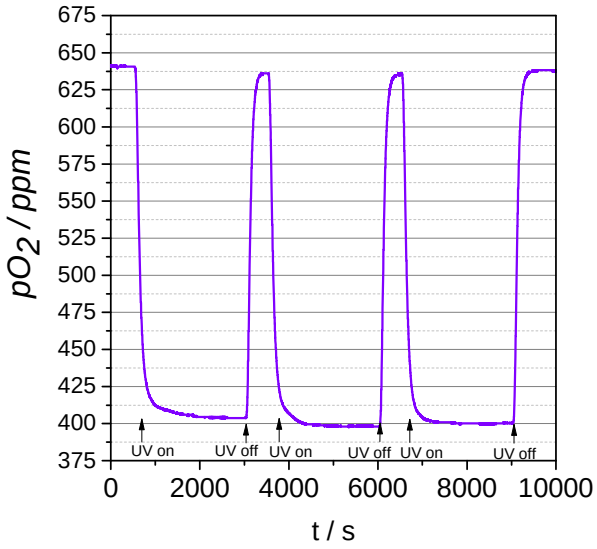
675
650
625
600
575
550
525
500
475
450
425
400
375
pO_2 / ppm
UV on
UV off
UV on
UV off
UV on
UV off
0
2000
4000
6000
8000
10000
t / s

***iii*) 500°C**

g)

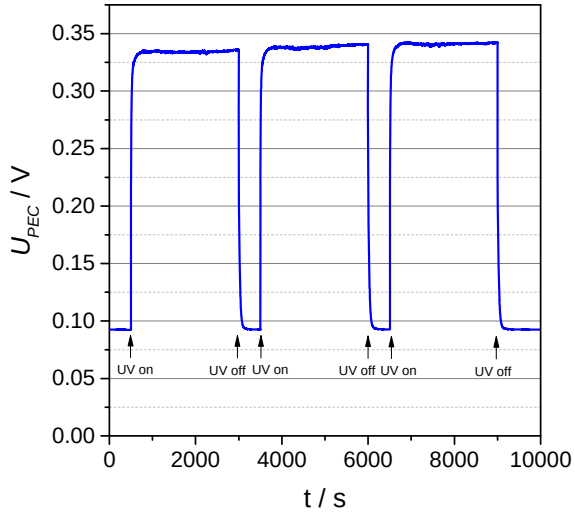

h)

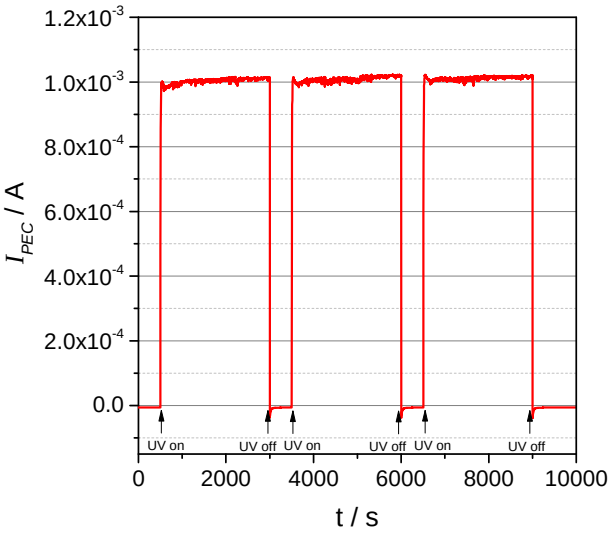

i)

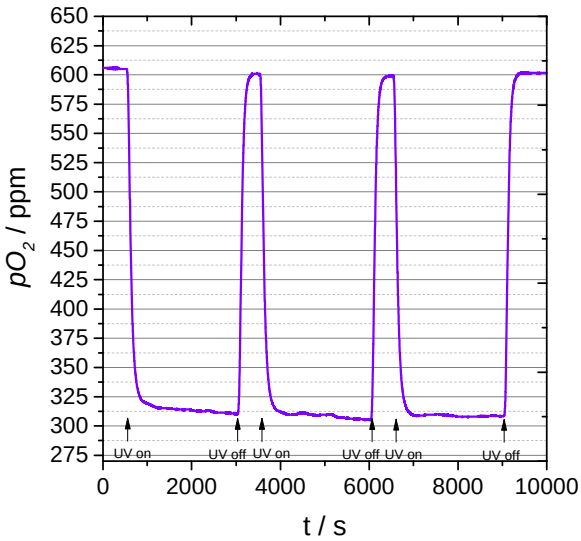

Figure 3.56: a,d,g) Voltage U_{PEC} of the cell with an open circuit voltage before UV on close to 100 mV due to asymmetric gas atmospheres. b,e,h) Current I_{PEC} upon UV light under short-circuit condition. c,f,i) Upon UV light, the oxygen fraction f_{O2} in the gas chambers lowered from 600 to 480 ppm at 400°C, 640 to 400 ppm at 450°C, and 600 to 310 ppm at 500°C.

4 Compilation of the essential results and conclusions

The effect of photochemical energy conversion at high temperatures by using a SOLID OXIDE PHOTO-ELECTROCHEMICAL CELL has been proofed and validated. The scientific work addressing the UV-light-driven oxygen pumping at high temperature as well as material related aspects have been published in the journal *Advanced Functional Materials* [91].

4.1 Acknowledgements

The results of UV-light driven oxygen pumping at high temperatures was realized with a solid oxide photo-electrochemical cell, as shown in Fig. 3.44, and has been published in *Advanced Functional Materials* [91]. This scientific work was supported within the framework of 16thBRIDGEprogram, funded by the Austrian Research Promotion Agency (FFG), with the contribution of Bernhard Rotter, Gregor Walch, Esmaeil Esmaeili, Dr. Alexander Karl Opitz, Prof. Karl Ponweiser, Prof. Johann Summhammer and Prof. Juergen Fleig. Apart from the few textual modifications, the following text is mostly identical with those which is published.

The authors gratefully acknowledge funding by the Austrian Research Promotion Agency (FFG) under project no. 838562. Furthermore, they are thankful to numerous colleagues of the Solid State Electrochemistry and Electroceramics Laboratory for fruitful scientific discussions and to the workshop of Institute for Energy Systems and Thermodynamics (Head: Prof. M. Haider) for excellent support in designing and manufacturing the setup for the photo(electro)chemical investigation, especially to A. Hofer and R. Steininger. Special thanks is also conveyed to Constantia Industries AG and NOVAPECC GmbH for financial support.

4.2 Introduction

A solid state photoelectrochemical cell (SOPEC) is operated between 400 and 500°C under 365 nm UV light. The cell consists of a photovoltaic part, based on a $La_{0.8}Sr_{0.2}CrO_3/SrTiO_3$ junction, and an electrochemical part including a zirconia solid electrolyte with a shared $(La,Sr)FeO_3$ electrode. The photovoltaic cell part leads to open circuit voltages up to 920 mV at 400°C. Upon UV light this driving force is used in the electrochemical part of the cell to pump oxygen from low to high partial pressures, *i.e.* to convert radiation energy to chemical energy. This demonstrates the feasibility of high temperature photoelectrochemical cells for solar energy storage. The detailed characterization of the different resistance contributions in the system by DC and AC methods reveals the parts of the cell to be optimized for finally achieving high temperature photoelectrochemical water splitting.

Exploiting solar energy by solar-to-fuel conversion, *i.e.* by transferring radiation energy to chemical energy, is of extraordinary relevance for future sustainable energy supply. One approach is based on photovoltaic cells and subsequent use of electricity in electrolysis cells to generate fuels such as hydrogen, CO or even hydrocarbons [42,92,93]. Integration of the photovoltaic part into one electrode of an

electrochemical cell is also an option [94]. Alternatively, direct transfer of solar energy to chemical energy is possible in photo(electro)chemical cells [21,48,60,50,95,96,97,98]. By illuminating photochemically active materials such as TiO_2, water splitting and thus hydrogen production takes place without preceding photovoltaic electricity generation. Either oxygen and hydrogen generation take place at one and the same material, or the corresponding reactions are separated to two electrodes of photoelectrochemical cells. Such solar to fuel conversion systems are based on liquid water and despite being heavily investigated, high efficiencies together with high system stability have not been achieved yet [50,96,97,98]. Thermochemical energy conversion based on high temperature materials is a third approach and generally employs two step processes with oxygen release (*i.e.* a reduction reaction) at high temperature and chemical water splitting at lower temperatures [99,35,30,31,36]. Interestingly, only very few activities aim at a combination of high temperatures and photoelectrochemical energy storage. In a theoretical paper, a solid state electrochemical cell was suggested for splitting of steam at high temperatures by solar radiation [100]. Such a high temperature cell running on steam may avoid stability problems of photoactive materials in liquid water, can exploit the reduced theoretical energy input required for water splitting at higher temperatures and does not suffer from problems due to heating in case of high solar energy intensity. However, to the best of the authors' knowledge, experimental realization of solid electrolyte based (photo-)electrochemical cells for photon-driven steam electrolysis has not been reported yet.

The scope of this paper is to experimentally demonstrate the feasibility of a high temperature solid state photoelectrochemical cell (SOPEC). The multilayer cell used consists of a sequence of different oxides, some being active in terms of photovoltaics and some using the voltage to chemically store energy. At operating temperatures between 400°C and 500°C UV light-induced open circuit voltages as high as 900 mV are directly transferred into chemical energy via oxygen pumping from low to high oxygen partial pressure. The experiments show that solid state photoelectrochemical cells can indeed be realized and that improved cells for water splitting and thus hydrogen production are feasible.

4.3 The high-temperature photoelectrochemical cell

The solid state photoelectrochemical cell (SOPEC) investigated in this study is sketched in **Figure 4.1**a. It includes a thin layer of $La_{0.8}Sr_{0.2}CrO_3$ (LSCr82) deposited on a nominally undoped $SrTiO_3$ (100) single crystal; a scanning electron microscopy (SEM) cross section image of such a LSCr82 layer on $SrTiO_3$ is shown in **Figure 4.1**b.

A thin film Pt current collector grid is used on top of LSCr82. The $SrTiO_3$ single crystal with top layers is attached to a symmetrical solid state electrochemical cell with porous $La_{0.6}Sr_{0.4}FeO_{3-\delta}$ (= LSF64) electrodes on a tetragonal zirconia polycrystal (TZP). Hence, the entire cell – in the following denoted as photoelectrochemical (PEC) cell – can be divided into two parts: a photovoltaic (PV) part consisting of LSCr82/$SrTiO_3$/LSF64 and an electrochemical (EC) part including LSF64/zirconia/LSF64. One LSF electrode acts as shared electrode, *i.e.* as top electrode of the EC cell and bottom electrode of the PV cell.

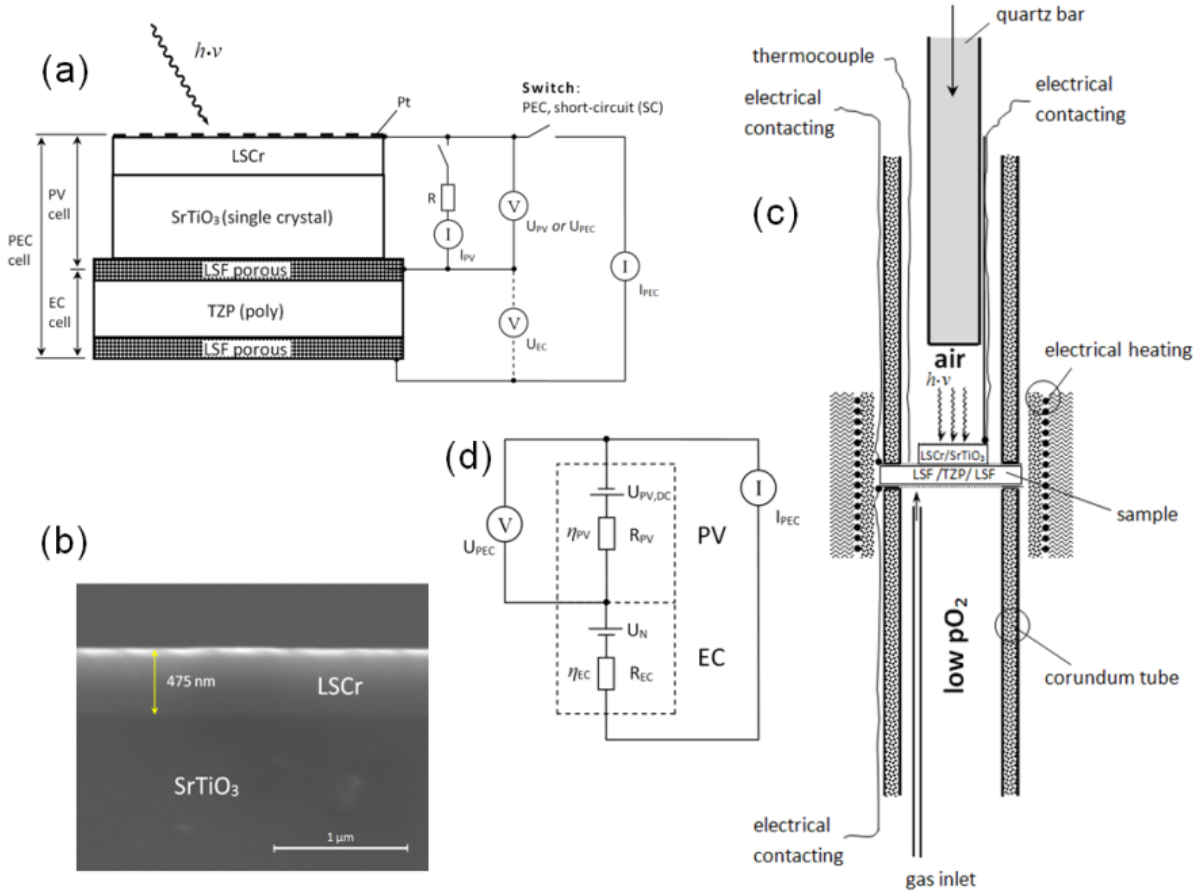

Figure 4.1: a) Sketch of the investigated solid oxide photoelectrochemical cell (SOPEC cell) and the measurement arrangement. b) SEM cross section image of a 20% Sr doped $LaCrO_3$ (LSCr82) layer on a (100) $SrTiO_3$ single crystal. c) Sketch of the entire setup for investigating the photoelectrochemical cell with two different gas chambers. d) Circuit representing the entire PEC cell. Both the PV and EC part are represented by an ideal battery with internal resistance. The PV "battery" with voltage $U_{PV,OC}$ operates only under illumination and the Nernst voltage U_N is only effective for asymmetric gas supply.

This PEC cell is mounted in a tube furnace such that two different gas compartments result, see **Figure 4.1**c. At temperatures between 400 and 500°C the PEC cell is illuminated by UV light (365 nm) and the electrical performance is

investigated, together with chemical effects (oxygen pumping monitored by oxygen partial pressure changes). Voltages are always measured between the LSCr82 top electrode and the shared LSF64 electrode, either without connection between top and PEC cell bottom electrode (then indicated by symbol U_{PV}) or with an external short-circuit (SC), *i.e.* under PEC operating conditions (denoted U_{PEC}), see Fig.4.1a. In the latter case, the voltage of the EC cell part (U_{EC}) equals the measured voltage U_{PEC} due to the external short-circuit, *i.e.* U_{PEC} (= U_{PV})= U_{EC} (all voltages with positive sign). Currents are either I_{PEC} indicating the short-circuit current of the entire PEC cell, or I_{PV} when only investigating the PV part of the cell. A simplified electrical representation of the PEC cell is shown in **Figure 4.1**d. It includes internal resistances of both cell parts and the ideal voltages occurring in the cell, a photovoltaic voltage $U_{PV,OC}$ of the illuminated cell and a Nernst voltage U_N of the electrochemical cell with asymmetric gas supply. This model helps understanding the experiments but is far from being complete; particularly it excludes a detailed representation of the PV cell (internal diode, *etc*.) and non-linearities of the EC cell.

4.4 Results and discussion

4.4.1 UV-light-driven oxygen pumping in the solid state photoelectrochemical cell

When illuminating the PEC cell under open circuit condition, a temperature dependent voltage $U_{PV,OC}$ can be measured at the PV cell. **Figure 4.2**a,c display the fast emergence of the voltage at 400°C and 500°C after switching the UV light on.

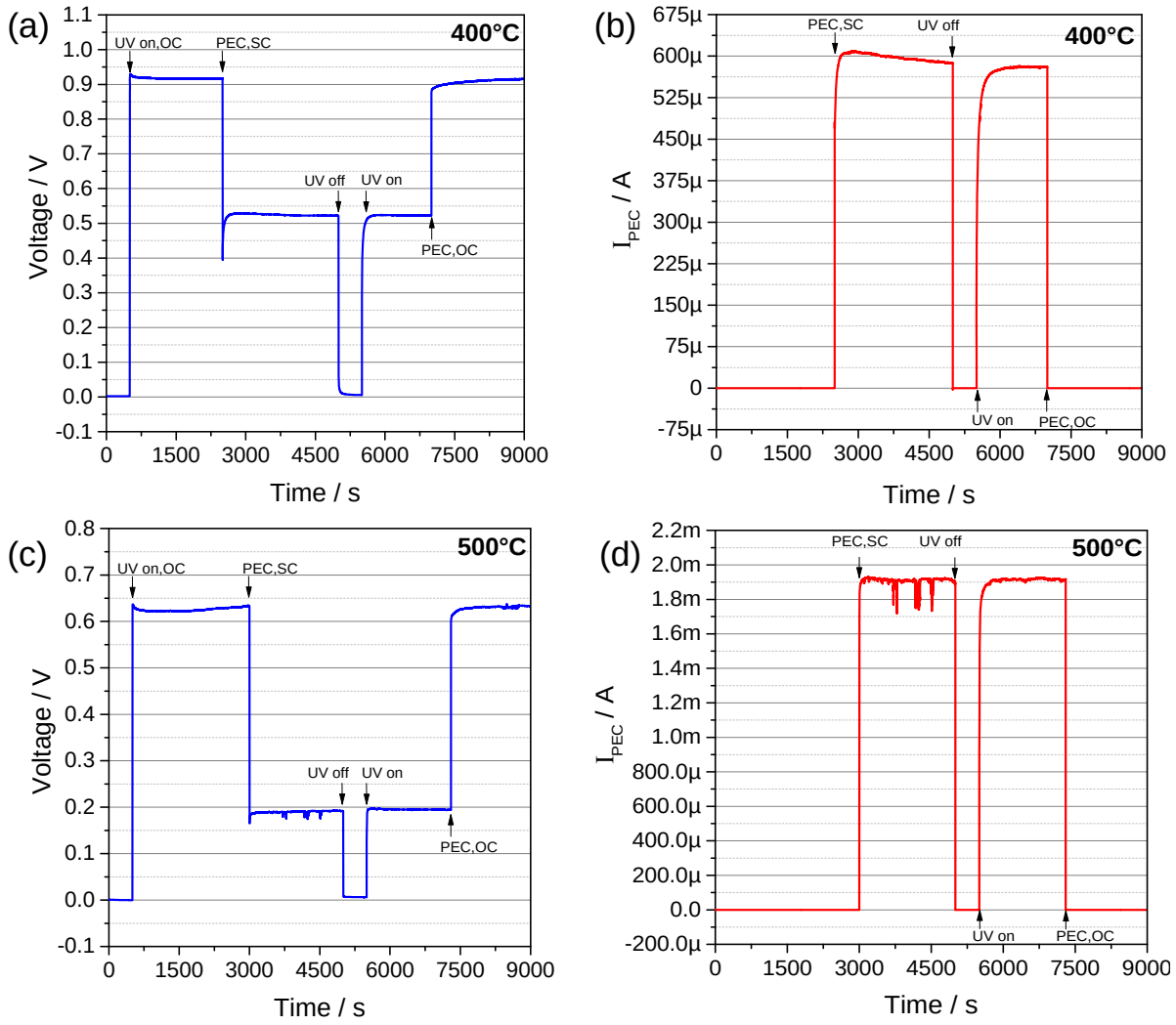

Figure 4.2: (a), (c) Open circuit voltage ($U_{PV,OC}$) after switching UV on and voltage under working condition of the PEC cell (U_{PEC}) after short-circuiting (SC) the illuminated PEC cell at 400°C (a) and 500°C (c) in symmetric gas atmospheres, $T = T_{dark}$, UV on-off is indicated. (b), (d) Corresponding current of the PEC cell (I_{PEC}).

This open circuit voltage with negative polarity at the LSCr82 electrode is highest at 400°C (920 mV) and decreases to 630 mV at 500°C. All values are summarized in **Figure 4.3**a. Short-circuiting the PV cell leads to currents $I_{PV,SC}$ in the mA range. The highest value of 2.3 mA is found at 500°C, all measured currents are summarized in **Figure 4.3**b.

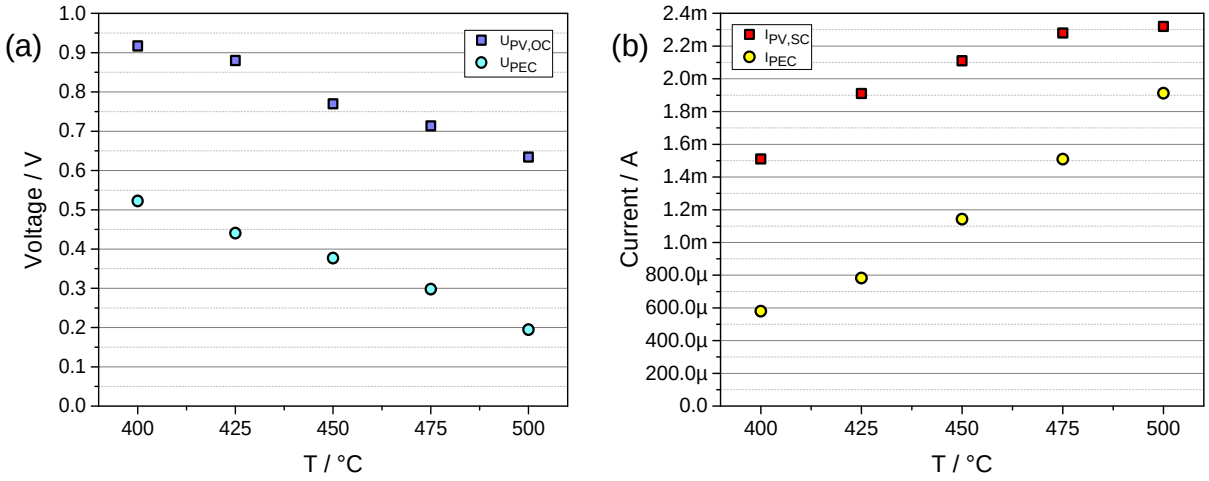

Figure 4.3: (a) PV cell open circuit voltages ($U_{PV,OC}$) and voltages U_{PEC} of the operating SOPEC cell at temperatures from 400-500°C ($T = T_{dark}$) in symmetric gas atmospheres. (b) Short-circuit currents of the PV cell solely ($I_{PV,SC}$) and of the PEC cell (I_{PEC}) at temperatures from 400-500°C in symmetric gas atmospheres.

From this we conclude that the $SrTiO_3$ single crystal together with the Sr doped $LaCrO_3$ (LSCr) top electrode act as an oxide photovoltaic cell with large voltages up to temperatures as high as 500°C. Another high temperature solar cell based on Nb-doped $SrTiO_3$ was described by HORKIKI et.al. [101], but voltages were much smaller in that case. The large voltage found in our cell is the basis of the light-to-chemical energy conversion established here.

When short-circuiting the top (LSCr82) and bottom (LSF64) electrode of the illuminated PEC cell with symmetrical gas exposure (ambient air at both sides), the measured voltage U_{PEC} drops to 0.19-0.52 V (depending on temperature) and a short-circuit current up to 1.9 mA flows in the cell, see **Figure 4.2**b,d. Relating this current to the electrode area of the electrochemical cell (1.8 cm^2) leads to a current density of ca. 1 mA/cm^2. The exact voltages U_{PEC} and currents I_{PEC} of the operating PEC cell are summarized in **Figure 4.3**a,b. The short-circuit current I_{PEC} has to be ionic in the zirconia electrolyte and thus electrochemical reactions have to take place at the two LSF64 electrodes of the illuminated PEC cell. In the given cell this is $1/2\ O_2 + 2e^- \Rightarrow O^{2-}$ at the bottom LSF64 electrode and the reverse reaction at the shared LSF64 electrode. Provided the voltage U_{PEC} is sufficiently large, this could even allow photoelectrochemical water splitting. Recently, it was experimentally shown that in accordance with Nernst's equation splitting of gaseous water with measurable quantities of hydrogen generation may take place already at voltages much lower than the standard decomposition voltage of water, in that specific study already at ca. 600 mV [102].

In our study, however, the voltage of the short-circuited cell (U_{PEC}) is still somewhat lower. Hence, oxygen pumping against a higher oxygen partial pressure

rather than water splitting is employed to demonstrate the potential of the PEC cell for radiation energy to chemical energy conversion. Accordingly, illumination of the PEC cell is also performed for asymmetric gas supply, *i.e.* for the PV cell being in air and the bottom part of the EC cell being in nitrogen with ca. 600 ppm remaining oxygen (measured by an oxygen sensor). The PV cell is not affected by the gas change in the bottom compartment, but the EC cell now exhibits an open circuit voltage of 92-98 mV, depending on temperature (**Figure 4.4**a,d). This is in accordance with the expected Nernst voltage U_N between ambient air and 600 ppm O_2 (96.8 mV at 500°C). Upon illumination under short-circuit condition, again a substantial voltage U_{PEC} and a current I_{PEC} up to 1 mA at 500°C is found (**Figure 4.4**b,e).

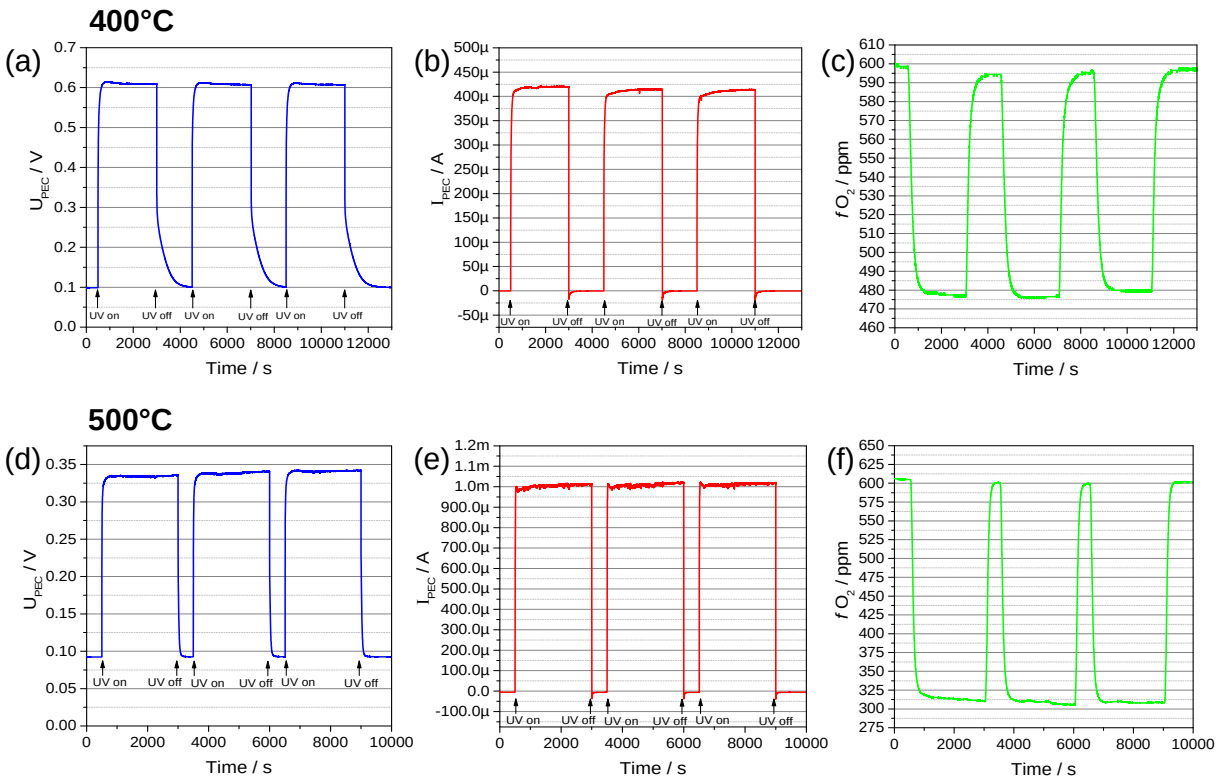

Figure 4.4: Results of the photoelectrochemically driven oxygen pumping experiment performed in asymmetric gas atmospheres at 400°C (top) and 500°C (bottom), $T = T_{dark}$, UV on-off is indicated. (a), (d) Voltage U_{PEC} of the cell with an open circuit voltage before UV on close to 100 mV due to asymmetric gas atmospheres. (b), (e) Current I_{PEC} upon UV light under short-circuit condition. (c), (f) Under UV light the oxygen fraction f_{O2} in the gas chamber is lowered from 600 ppm to 480 ppm at 400°C and 310 ppm at 500°C.

The measured short-circuit current I_{PEC} leads to pumping of oxygen from the low partial pressure side (oxygen fraction, f_{O_2}, of about 600 ppm O_2 in 1 bar gas) to the high partial pressure side (about 20% O_2 in 1 bar gas). **Figure 4.4**c,f shows that the oxygen content in the low pressure compartment, measured by the oxygen sensor at the outlet, substantially decreases upon UV light. An oxygen fraction of 480 ppm is reached at 400°C and almost 300 ppm at 500°C. The correlation between measured

current and oxygen pumping becomes clear from the almost linear relation between current and oxygen fraction change Δf_{O_2} (in ppm), see **Table 4.1**. Obviously, UV induced oxygen pumping indeed takes place and thus transfer of radiation energy to chemical energy. To the best of our knowledge, this is the first experimental demonstration of a light driven reaction in a high temperature solid state electrochemical cell.

Table 4.1: Decrease of the oxygen content in the gas flow at different temperatures and the current of the PEC cell, $T = T_{dark}$.

Temperature	Change of oxygen content Δf_{O2}	Current I_{PEC}
°C	Ppm	µA
400	120	410
450	240	830
500	290	1000

Compared to symmetrical gas condition, voltages U_{PEC} are larger and short-circuit currents I_{PEC} are smaller, cf. Fig. 4.3 and 4.4. This is straightforward to understand: Owing to negligible gas composition changes in a PEC cell with symmetrical gas supply (air on both sides), the voltage $U_{PEC} = U_{PV}$ of the short-circuited PEC cell is entirely consumed to drive the oxide ion current through the EC cell. Hence, U_{EC} ($=U_{PV}$) is the sum of all overpotentials η_{EC} in the EC cell, *i.e.* of anodic, cathodic and ohmic overpotentials. The difference between $U_{PV,OC}$ and U_{PEC}, on the other hand, is the voltage loss in the PV cell (η_{PV}) and can be associated with its internal resistance ($\eta_{PV} = U_{PV,OC} - U_{PEC}$). When an additional Nernst voltage U_N comes into play due to different gas compositions in the two cell compartments, U_{EC} is no longer given by the internal overpotential of the EC cell solely, but reads

$$U_{EC} = U_{PEC} = U_N + \eta_{EC} . \tag{4.1}$$

Therefore, U_{EC} is increased in the asymmetrical cell. The voltage remaining in the PV cell (η_{PV}), on the other hand, is decreased in accordance with

$$U_{PV,OC} = \eta_{PV} + \eta_{EC} + U_N . \tag{4.2}$$

The corresponding voltages are also indicated in Fig. 4.1d: Under short-circuit condition, the ideal open circuit voltage of the PV cell does not only drive a current

across the two internal resistances R_{PV} and R_{EC}, but has also to overcome the Nernst voltage U_N. I_{PEC} is thus lower than for symmetrical gas supply.

For a quantitative estimate of the gas composition change upon UV illumination, we can relate the pumping current I to a molar flux j_{O_2} of oxygen molecules by

$$j_{O_2} = \frac{1}{4F} I \,, \tag{4.3}$$

and correlate this with the gas flow rate Q_{gas}; F denotes Faraday's constant. For ideal gases and gas pressure p_{gas} we get the molar gas flux

$$j_{gas} = Q_{gas} \frac{p_{gas}}{RT} . \tag{4.4}$$

Lowering the O_2 fraction in the gas by Δf_{O_2} corresponds to a current driven molar oxygen flux of

$$j_{O_2} = j_{gas} \Delta f_{O_2} = Q_{gas} \frac{p_{gas}}{RT} \Delta f_{O_2} \tag{4.5}$$

and according to Eq. 4.3 to a current of

$$I = \frac{4F}{RT} Q_{gas}\ p_{gas}\ \Delta f_{O_2} . \tag{4.6}$$

For Q_{gas} = 10 ml/min, p_{gas}= 1 bar and Δf_{O_2} of 290 ppm at 500°C we get 290 µA. This is lower than the measured short-circuit current (ca. 1 mA) but still sufficiently close to be considered as realistic: In our estimate a constant oxygen partial pressure in the entire compartment was assumed even under pumping condition, which is hardly the case. Inhomogeneties (also in combination with the unknown location of small gas leakage(s) which increase the O_2 content in the N_2 stream) may easily cause the larger pumping current found in the experiment.

4.4.2 Characterization of the high-temperature photoelectrochemical cell and the electrochemical cell

For a better understanding of our solid oxide photoelectrochemical cell, we characterized the PV part of the PEC cell by determining its *I-V* curves under illumination, *i.e.* measuring U_{PV} and I_{PV} for different loads and temperatures (**Figure 4.5**).

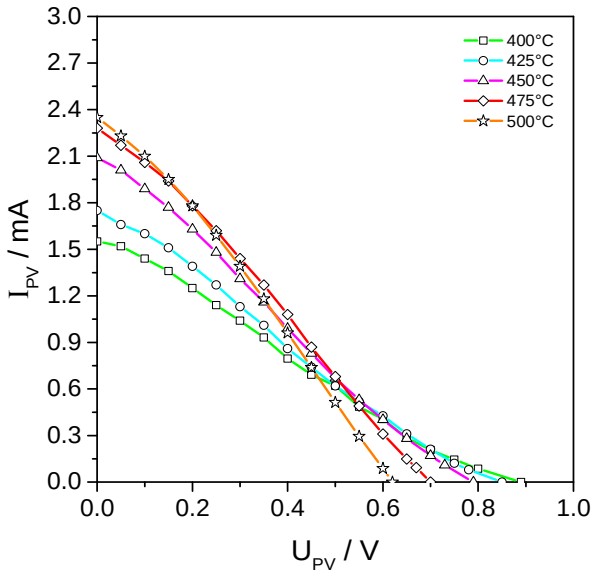

Figure 4.5: *I-V* characteristics of the PV cell solely, obtained by measuring U_{PV} and I_{PV} for different loads and temperatures from 400°C to 500°C ($T = T_{dark}$).

As already discussed, the open circuit voltage $U_{PV,OC}$ decreases with increasing temperature, while the short-circuit current $I_{PV,SC}$ increases. Hence, the maximum power output is rather temperature independent at 0.33-0.45 mW between 400 and 500°C. A detailed mechanistic understanding of the PV cell and its *I-V* curve is beyond the scope of this paper; it may include not only the photo active junction but also an ohmic and an additional non-linear serial resistive contribution. However, we can empirically evaluate the temperature dependent resistance of the PV cell part in the operating PEC cell from

$$R_{PV,PEC} = \frac{\eta_{PV}}{I_{PV}} = \frac{U_{PV,OC} - U_{PV}}{I_{PV}}. \qquad (4.7)$$

The resulting values in the several 100 Ω range decrease with increasing temperature and are plotted in **Figure 4.6**a.

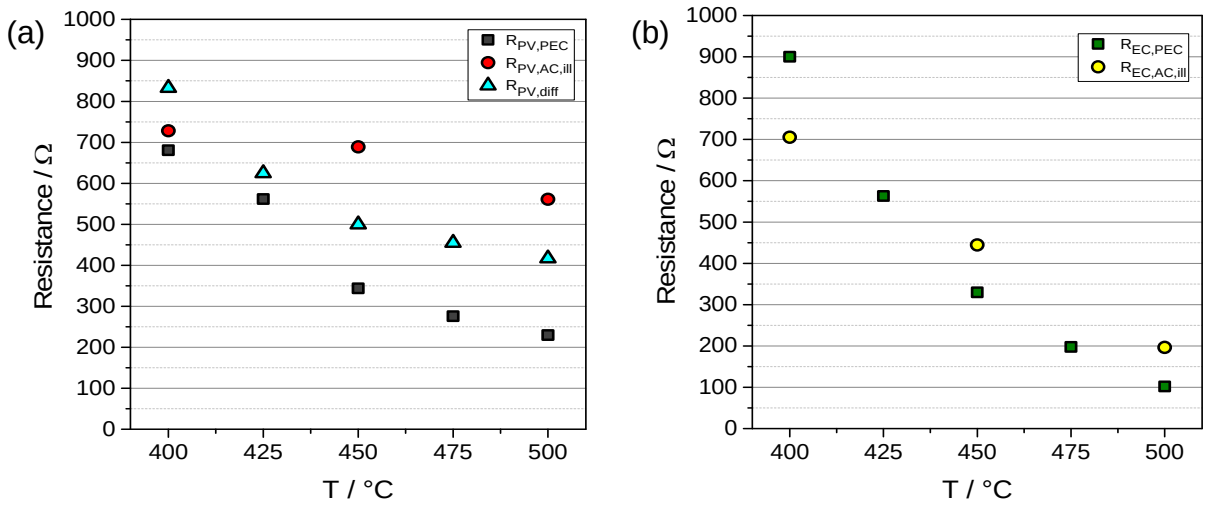

Figure 4.6: (a) Temperature dependent resistances of the PV cell in the operating SOPEC cell ($R_{PV,PEC}$, T = T_{dark}), the corresponding total AC resistance of the illuminated PV cell ($R_{PV,AC,ill}$, T = T_{UV}) and the approximate differential resistances $R_{PV,diff}$ (T = T_{UV}) obtained by linearizing the *I-V* curves at temperatures between 400 and 500°C. (b) Temperature dependent resistances $R_{EC,PEC}$ calculated from U_{PEC}/I_{PEC} (T = T_{dark}) of the illuminated SOPEC cell and the total AC resistances of the illuminated cell ($R_{EC,AC,ill}$, T = T_{UV}) at temperatures between 400 and 500°C.

Alternatively, we may determine approximate differential resistances by linearizing the *I-V* curves in Fig. 4.5. This was done for short-circuiting conditions (*i.e.* $R_{PV,diff}$ = 50 mV/($I_{PV,SC}$-$I_{PV,50mV}$)) and the corresponding resistances are also shown in Figure 4.6a: Values between 417 and 833 Ω are found, in reasonable agreement with $R_{PV,PEC}$.

For further information, impedance spectra were measured on the PV cell part under dark condition and during illumination. In the complex impedance plane the spectrum of the dark PV cell consists of a high frequency arc, an intermediate frequency "shoulder" and a huge low frequency arc. The capacitance of the high frequency arc is close to a typical bulk capacitance of $SrTiO_3$. The resistance of this semicircle is attributed to electronic charge transport in the $SrTiO_3$ single crystal. The corresponding conductivity is strongly temperature dependent ($2.38 \cdot 10^{-6}$ S cm^{-1} at 400°C, $8.33 \cdot 10^{-6}$ S cm^{-1} at 450°C and $2.50 \cdot 10^{-5}$ S cm^{-1} at 500°C), in accordance with literature (hole conduction with deep hole traps) [87,79,88]. The impedance spectrum obtained for a $SrTiO_3$ single crystal with a Pt electrode instead of a LSCr82 electrode (**Figure 4.7**a, inset) indicates that the intermediate frequency feature can most probably be attributed to the LSF64 electrode.

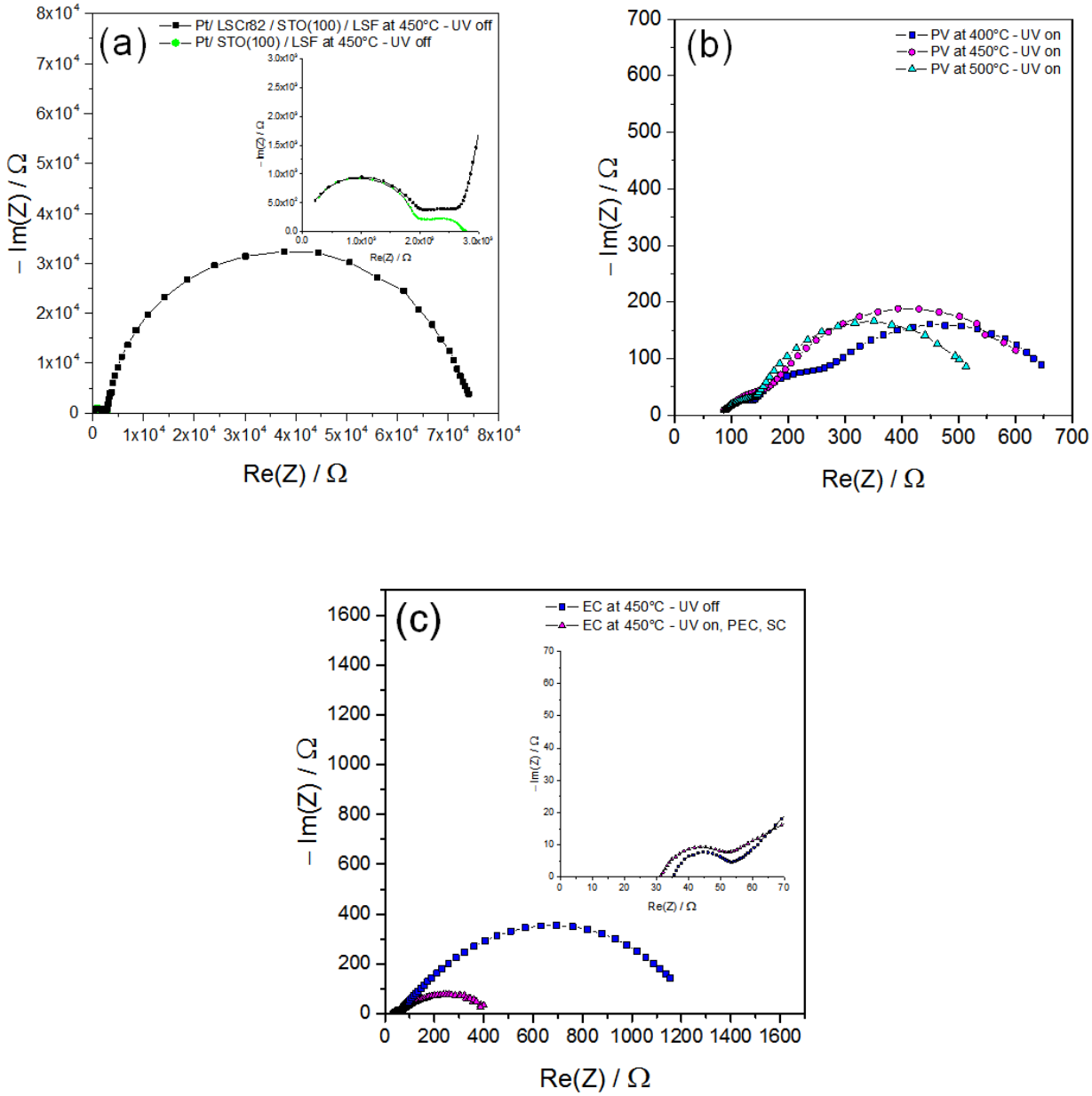

Figure 4.7: (a) Impedance spectrum of the dark PV cell at 450°C; the large arc is caused by the $SrTiO_3$/LSCr82 interface. The inset shows a magnification of the spectrum part caused by the $SrTiO_3$ single crystal and the spectrum of a $SrTiO_3$ single crystal with Pt instead of the LSCr82 as top electrode. (b) Spectra of the illuminated PV cell measured at 400 - 500°C ($T = T_{UV}$) under short-circuit condition. (c) Impedance spectra of the EC cell before and during illumination of the short-circuited PEC cell at 450°C ($T = T_{UV}$ for UV on, and $T = T_{dark}$ for UVoff).

Accordingly, the very pronounced low frequency arc of the PV cell reflects the $SrTiO_3$/LSCr82 interface, *i.e.* a space charge zone with strong depletion of the main charge carrier (holes in undoped $SrTiO_3$) [88,103]. Within the framework of the drift-diffusion model, we may even estimate the space charge potential from the relaxation frequencies ω_i of the bulk arc (b) and the interfacial space charge (sc) arc [104,105] according to

$$\frac{\omega_b}{\omega_{sc}} = \frac{\exp(e\Delta\varphi / kT)}{2e\Delta\varphi / kT}. \qquad (4.8)$$

From the spectra we obtain 845 mV at 450°C and thus a realistic value with regard to the open circuit voltage of the illuminated PV cell at the same temperature (778 mV).

The spectrum changes drastically under illumination: **Figure 4.7**b displays the impedances measured at 400 - 500°C under short-circuit condition. The high frequency arc is now outside the measurable frequency range, due to a strong decrease of its resistance and thus strong increase of its relaxation frequency. The resistance of the illuminated $SrTiO_3$ single crystal is drastically decreased to about 4 % of its original value at 450°C. However, it is no longer significantly temperature dependent. From this we conclude that photoconductivity is strongly increased in the entire $SrTiO_3$ single crystal. Possibly the recombination of the generated electronic charge carriers in $SrTiO_3$ is sufficiently slow to "flood" the entire single crystal with electrons.

Transmission spectra of a $SrTiO_3$ single crystal and band gaps estimated from 50 % of the maximum transmittance are shown in **Figure 4.8**.

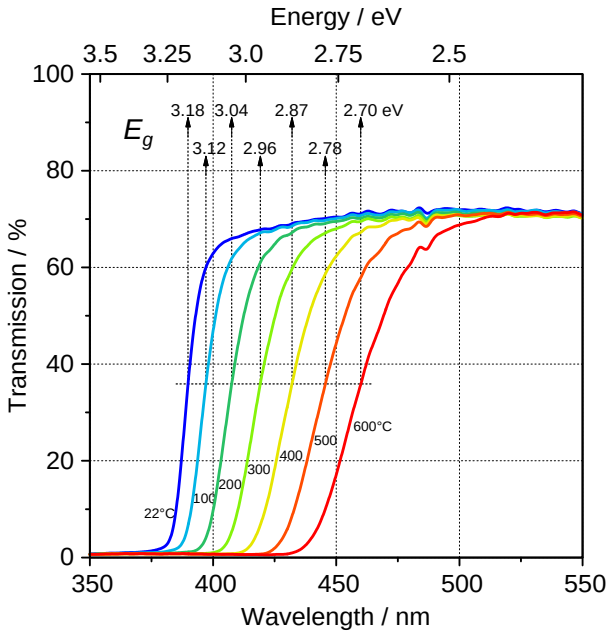

Figure 4.8: Wavelength dependent transmission of light through a $SrTiO_3$ single crystal (0.5 mm thickness) as function of temperature measured in air. Band gap energies E_g are deduced from half maximum transmission and also indicated ($T = T_{setup}$).

At room temperature 3.18 eV are found, in good agreement with the indirect band gap reported in literature (3.2 eV) [106,107] while at 500°C the band gap is reduced to 2.78 eV. Hence, $SrTiO_3$ strongly absorbs the UV light used here (365 nm → 3.39 eV). (The indirect band gap of Sr-doped $LaCrO_3$ at room temperature is around 2.8 eV [86,85] but varies with dopant concentration; this material was recently suggested as a *p*-type transparent conducting oxide [108]. The size of the low frequency arc drastically decreases upon UV light by about two orders of magnitude at 450°C. The corresponding total AC resistance of the illuminated PV cell (*i.e.* the low frequency intercept $R_{PV,AC,ill}$) is also included in **Fig. 4.6**a and is in acceptable agreement with the differential resistance determined from the *I-V* curve close to short-circuiting condition.

A similar analysis can be made for the resistance of the EC part of the photoelectrochemical cell. For symmetrical gas supply, the entire voltage $U_{PEC} = U_{EC}$ is consumed by the different contributions to the overpotential of the electrochemical cell and thus a resistance can be calculated from

$$R_{EC,PEC} = \frac{U_{PEC}}{I_{PEC}}. \qquad (4.9)$$

Figure 4.6b displays the corresponding values for the illuminated PEC cell. Those are strongly temperature dependent and decrease from about 900 Ω at 400°C to 100 Ω at 500°C. This strong temperature dependence (reflecting an activation energy of about 1 eV) is not surprising, taking into account that temperature dependent processes are

involved, namely ion conduction in zirconia and oxygen reduction/production at LSF64 electrodes.

In order to get more details on the main contributor to this internal EC resistance, again impedance spectroscopic studies were performed. **Figure 4.7**c shows spectra measured before and during illumination of the short-circuited PEC cell at 450°C. In both cases the spectrum consists of a high frequency intercept, a small intermediate frequency arc and a large distorted low frequency arc. The capacitance of the intermediate frequency arc is much larger than a typical bulk capacitance of zirconia, indicating that it is either due to grain boundaries in TZP or an interfacial electrode effect. The high frequency intercept is largely due to ion conduction in the bulk (grains) of TZP; the conductivity calculated from the corresponding resistance (ca. $3.1 \cdot 10^{-4}$ S cm^{-1}) fits well to the ionic conductivity of TZP reported in literature (about $3\text{-}4 \cdot 10^{-4}$S cm^{-1}) [109,110]. The low frequency arc has the typical half tear drop shape of porous mixed conducting electrodes in oxygen atmosphere [111] and is attributed to the electrochemical oxygen exchange reactions in the LSF64 electrodes.

Measurements upon illumination lead to much lower values of the LSF electrode related resistance, an effect that can be attributed to the non-linearity of electrode processes in solid state electrochemical cells. The total AC resistance of the cell ($R_{EC,AC,ill}$) is in the same range as the DC resistance $R_{EC,PEC}$ of the operating cell calculated from Eq. 4.9, though less temperature dependent. Differences are most probably again due to the non-linearity of the electrode resistances. The size of the high frequency intercept varies slightly despite nominally identical temperature of dark and illuminated PEC cell. This is attributed to a slight difference between the UV light induced heating of the thermocouple and of the sample itself, see Sec. 5.

From this analysis, we get also information on the cell component that is most critical under PEC cell operation. In accordance with Eq. 4.7 and 4.9 the ratio

$$\frac{R_{PV,PEC}}{R_{EC,PEC}} = \frac{U_{PV,OC}}{U_{PEC}} - 1 \qquad (4.10)$$

is a measure of the relative importance of the two internal resistances. **Figure 4.9** displays this ratio for different temperatures.

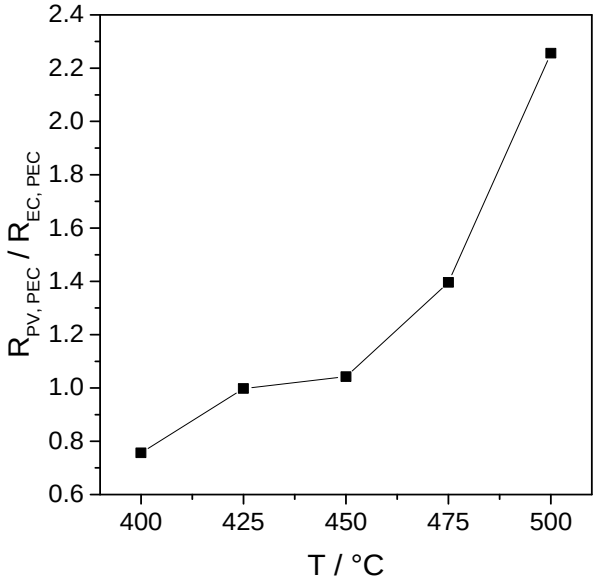

Figure 4.9: Ratio of the two PEC cell internal resistances, *i.e.* of the PV cell resistance $R_{PV,PEC}$ and the EC cell resistance $R_{EC,PEC}$ for temperatures between 400 and 500°C ($T = T_{dark}$).

At 400°C the EC cell contributes slightly more to the overall resistance than the PV cell; at these temperatures significant improvement could be made by optimizing the oxygen exchanging electrodes of the EC cell. At 500°C, on the other hand, the electrochemical cell is already much less resistive than the PV cell. At this temperature, a reduction of the internal resistance of the PV cell would be most efficient. Reduction of the $SrTiO_3$ thickness may help, but also different doping of either $SrTiO_3$ or LSCr82 could be used to optimize performance and to achieve even higher voltages. Both measures could ultimately enable a water splitting photoelectrochemical cell based on high temperature solid state components.

4.5 Experimental section

The photoelectrochemical cell sketched in Fig. 4.1a was prepared as follows: In a first step, a 475 nm thin layer of $La_{0.8}Sr_{0.2}CrO_3$ (LSCr82) was deposited on a nominally undoped $SrTiO_3$ (100) single crystal (Crystec GmbH, Germany, 0.5 mm thickness, 10 x 10 mm^2) by pulsed laser deposition (PLD). The deposition time was 30 minutes (18000 pulses) with the laser operating at a pulse energy of 400 mJ (at the laser) and a repetition rate of 10 Hz. The LSCr82 material for the target was obtained from AMERICAN ELEMENTS, LA, USA, pressed and sintered at 1200°C for 12 hours with a heating and cooling rate of 10°C min^{-1}. A SEM cross section image of a LSCr82 layer on $SrTiO_3$ is shown in Fig. 4.1b. On top of this layer, a Pt current collector grid (stripe

width: 10 μm, stripe distance: 40 μm, Pt coverage of 23%) was prepared by sputter deposition and a subsequent lift-off photolithographic process.

In a second step, a symmetrical zirconia based electrochemical cell was prepared: On a tetragonal zirconia polycrystal (TZP) substrate (KERAFOL Keramische Folien GmbH, 3 mol% Y_2O_3, 300 μm thickness, 2 cm in diameter) two porous mixed conducting $La_{0.6}Sr_{0.4}FeO_{3-\delta}$ (LSF64) electrodes were deposited from a paste. For this purpose, LSF powder from Sigma-Aldrich, Germany was ground with 5 mg ethyl cellulose and mixed with 85 mg terpineol ($C_{10}H_{18}O$) per 0.15 g powder. In a final step, the $SrTiO_3$ single crystal with LSCr82 top layer was placed on the electrochemical cell and the entire oxide stack was heated to 850°C for 5 h with a heating and cooling rate of 5°C min^{-1} in ambient air in order to anneal the LSF64 electrodes and to mechanically link the two sub-systems to form a single photoelectrochemical (PEC) cell. One LSF64 electrode thus acts as shared top electrode of the electrochemical (EC) cell and bottom electrode of the photovoltaic (PV) cell.

The PEC cell was mounted in a tube furnace such that two different gas compartments resulted, see Fig. 4.1c. The PV cell and the top LSF64 electrode of the EC cell were held in ambient air, while the bottom part of the EC cell (second LSF64 electrode) was exposed either to a 10 $mlmin^{-1}$ gas flow of nitrogen (with ca. 600 ppm O_2 remaining oxygen due to non-ideal gas tightness) or ambient air. The oxygen content in this gas was determined by an oxygen sensor (Rapidox 2100, Cambridge Sensotec Ltd., UK) positioned behind the gas outlet of the sample holder.

At temperatures between 400 and 500°C the PEC cell was illuminated by UV light using a 10 W LED (LED ENGIN, San Jose USA) with 365 nm. Light guidance into the setup was established by a quartz bar (10 mm in diameter). The light intensity at the sample surface was about 200-500 mW cm^{-2}. Electrical and electrochemical DC properties were measured with multimeters (DMM 2000, Keithely Instruments Inc., USA) as sketched in Fig. 4.1. Additionally, impedance spectra of both the photovoltaic as well as the electrochemical part of the PEC cell were measured in two-point geometry by connecting the corresponding electrodes to an Alpha-A High Performance Frequency Analyzer from Novocontrol Technologies, Germany.

Upon illumination, the thermocouple (type K) positioned close to the sample, showed a slight increase of typically 6-8°C. When appropriate, the set temperature of the heater was then decreased upon illumination such that the temperature measured by the thermocouple was the same as without illumination. It is indicated in all figures whether the given thermocouple temperature T refers to the dark (T_{dark}) or the illuminated (T_{UV}) case. The change of the TZP electrolyte resistance, measured by impedance spectroscopy, also allows an estimate of the temperature change upon UV illumination. Assuming an activation energy of 1 eV for ion conduction in

zirconia we could deduce temperature increases of ca. 5-10°C, which is in excellent agreement with the changes indicated by the thermocouple.

4.6 Conclusions

Combination of a highly Sr-doped $LaCrO_3$ thin film and a $SrTiO_3$ single crystal leads to a high temperature photovoltaic cell with open circuit voltages up to > 900 mV at 400°C. When stacking this photovoltaic cell and with a solid state electrochemical cell, photo-powered oxygen pumping from low to high oxygen partial pressures becomes possible. Pumping currents of ca. 1 mA cm^{-2} are realized and this causes a significant lowering of the oxygen content in the low oxygen pressure compartment of the PEC cell. Hence, the proof of concept for solar to fuel conversion by high temperature solid state electrochemical cells has been established. The measured voltages could be attributed to different internal resistances in the PEC cell or a Nernst voltage. Already moderate improvements of the cell are expected to lead to voltages and currents that allow water splitting in a steam-based high temperature photoelectrochemical cell.

5 Appendix

5.1 List of figures

Figure 1.1: Schematic of a stationary thermal water-splitting process operating between a high-temperature (T_H) and a low-temperature (T_L) level 2
Figure 1.2: Schematic of a reversible stationary high- temperature electrolysis process operating at a constant high-temperature level (T) with a pressure (p) 4
Figure 2.1: Energy requirements for thermal dissociation of water into hydrogen (H_2) and oxygen (O_2) at 1 bar. Calculated from thermochemical data by using *FactSage 6.1* [26]. 12
Figure 2.2: Energy requirements for thermal dissociation $ZnO(s) \rightarrow Zn + ½\ O_2$ at 1 bar. Calculated from thermochemical data by using *FactSage 6.1* [26] 13
Figure 2.3: Process diagram for regeneration (O_2-releasing) of the reactive material at a high temperature level T_H and an oxidation (H_2-production) at a lower temperature T_L performed by several change of states (CofS); Own graphic and adapted from *Ref.* [11]. 14
Figure 2.4: Theoretical thermochemical water-splitting efficiency compared to Carnot efficiency. 18
Figure 2.5: Scheme of a solid oxide electrochemical cell (SOEC) for high-temperature 20
Figure 2.6: Energy demand of high temperature electrolysis demonstrating the advantage of lowered electrical energy demand at high temperatures; calculated from thermochemical data by using *FactSage* 6.1 [26] 21
Figure 2.7: Typical polarization curves for state of the art electrolyzer technologies [41]. 22
Figure 2.8: Energy demand and temperature dependency of high temperature of H_2O and CO_2 co-electrolysis; calculated from thermochemical data by using *Ref.* [43]. 24
Figure 2.9: Photo-assisted electrochemical water-splitting in an acid electrolyte solution. 26
Figure 3.1: Schematic of the SOPEC cell, using concentrated radiation and an external power supply for a solar hydrogen production. 29
Figure 3.2: Sketch of the investigated Solid Oxide Photo-electrochemical cell 34
Figure 3.3: View in the vacuum chamber of an operating PLD and the indicated distance between target and heater. 35
Figure 3.4: Micro-structured STF73 electrodes deposited on YSZ (100) single crystal and electrically contacted by high-precision manipulators for electrochemical characterization. 35

Figure 3.5: SEM cross section image of a 30% Fe doped $SrTiO_3$ (SFT73) layer on a YSZ (100) single crystal deposited with a) L_{TH} = 7.5 cm, b) L_{TH} = 7.0 cm and c) L_{TH} = 6.5 cm. 36
Figure 3.6: Pseudo-linearity of electrochemical systems at low AC amplitudes. 36
Figure 3.7: Excitation signal and response signal at time *t* with the phase-shift Ø in the response signal. 37
Figure 3.8: Excitation signal and response signal plotted in Lissajous figure. 37
Figure 3.9: Representation of complex impedance constituted as Nyquist plot. 38
Figure 3.10: Equivalent circuit. 38
Figure 3.11: Chamber with heating stage, cooling system and high-precision micro-manipulators. 39
Figure 3.12: Setup for electrochemical characterization with microscope (1), chamber with heating stage (2), pressure gauges (3) and humidifier (4). 39
Figure 3.13: Sketch of the investigated STF73 thin-film microelectrodes deposited on YSZ (100) and the measurement arrangement for electrochemical characterization with EIS. 40
Figure 3.14: Sketch of the measurement environment for electrochemical characterization with EIS. 40
Figure 3.15: EIS measurements on STF73 thin-film microelectrodes with 40 µm in diameter at 700°C (T_{set}) in wet N_2 gas atmosphere by switching the light source (SoLux, 50 W, 4700 Kelvin) on and off. 41
Figure 3.16: DC measurements on STF73 thin-film microelectrodes with 40 µm in diameter at 700°C (T_{set}) in wet N_2 gas atmosphere by switching the light source (SoLux, 50 W, 4700 Kelvin) on and off. 41
Figure 3.17: Arrangement of the tubular furnace with the inserted tubular reactor. . 41
Figure 3.18: Setup with a light source by using a 1000 watts xenon arc lamp. 41
Figure 3.19: EIS measurements on STF73/YSZ/STF73 (25x25x0.3) at 600°C (T_{cell}) in wet N_2 gas atmosphere by switching the light source (Newport, 1000 watts, xenon arc lamp) on and off. 42
Figure 3.20: Sketch of the investigated STO (100) single crystal with the dimension (10x10x0.5) mm in dark and under illumination, equipped with a plane Pt bottom electrode and a Pt mesh electrode on top. 44
Figure 3.21: Impedance spectrum of Pt/STO(100)/Pt 350°C; the large spectrum represents the resistance of $SrTiO_3$ without illumination; under illumination the impedance spectrum is shrinking. 45
Figure 3.22: Impedance spectrum of Pt/STO(100)/Pt 400°C; the large spectrum represents the resistance of $SrTiO_3$ without illumination; under illumination the impedance spectrum is shrinking. 45

Figure 3.23: Impedance spectrum of Pt/STO(100)/Pt 450°C; the large spectrum represents the resistance of $SrTiO_3$ without illumination; under illumination the impedance spectrum is shrinking. 46
Figure 3.24: Pt/ STO(100)/ Pt single crystal in the dimension of (5x5x0.5) mm is equipped with an interdigitated top electrode; and exposed under illumination for EIS characterization. 47
Figure 3.25: Pt/ STO(100)/ Pt single crystal in the dimension of (5x5x0.5) mm is equipped with a circular electrode on top with 1 mm in diameter including a plane bottom electrode; and exposed under illumination for EIS characterization. 47
Figure 3.26: EIS measurements on Pt/ STO(100)/ Pt single crystal (GB_STO_08) in air at a set temperature of 450°C; in dark and with different types of LED sources. 48
Figure 3.27: EIS measurements on Pt/ STO(100)/ Pt single crystal (GB_STO_09) in air at a set temperature of 450°C; in sequence: (1) 2xEIS in dark, (2) 10 min illumination with 10W-LED/405 nm, and (3) LED-off; 8x EIS in dark. 49
Figure 3.28: EIS measurements on Pt/ STO(100)/ Pt single crystal (GB_STO_08) in air at a set temperature of 450°C; in sequence: (1) 2xEIS in dark, (2) 10 min illumination with 10W-LED/405 nm, and (3) LED-off; 4x EIS in dark. 50
Figure 3.29: Ideal perovskite structure in the general formula ABO_3. 51
Figure 3.30: Ordered lattice composed of perovskite unit cells. 51
Figure 3.31: Sketch of STO(100)/LSCr82 heterojunction which is 52
Figure 3.32: View in the vacuum chamber of an operating PLD for the deposition of thin-films. 53
Figure 3.33: SEM cross section image of a 20% Sr doped $LaCrO_3$(LSCr82) layer deposited on a $SrTiO_3$ (100) single crystal. 53
Figure 3.34: DC analysis: U_{OC} (galvanostatic I=0A) at a set temperature of 400°C in air under illumination with LED 1 W/405 nm by switching the light source on-off-on-off. 54
Figure 3.35: DC analysis: I_{SC} (potentiostatic U=0V) at a set temperature of 400°C in air under illumination with LED 1 W/405 nm by switching the light source on-off-on-off. 54
Figure 3.36: Cell structure of a HT-PV cell driven photoelectrochemical cell. 55
Figure 3.37: Analysis environment for DC characterization under illumination with a) fitted LED and b) by coupling the light through a quartz rod, in air at a set temperature of 450, 500 and 550°C. 56
Figure 3.38: *I-V* characteristic of LSCr82/STO(100) + Pt/YSZ/Pt at a,b) 450°C, c,d) 500°C, and e,f) 550°C in air under illumination with fitted 10W-LED-405 nm. 57

Figure 3.39: *I-V* characteristic of LSCr82/STO(100) + Pt/YSZ/Pt at a,b) 450°C, c,d) 500°C, and e,f) 550°C in air under illumination with 10W-LED-405 nm by coupling the light through a quartz rod. 58
Figure 3.40: *I-V* characterization of LSCr82/STO(100) + Pt/YSZ/Pt at a,b) 450°C, c,d) 500°C, and e,f) 550°C in air under illumination with fitted 10W-LED-365 nm. 59
Figure 3.41: *I-V* characterization of LSCr82/STO(100) + Pt/YSZ/Pt at a,b) 450°C, c,d) 500°C, and e,f) 550°C in air under illumination with 10W-LED-365 nm by coupling the light through a quartz rod. 60
Figure 3.42: Several part of the SOPEC tubular reaction (SOPEC-RR-V1); consist of I) the bottom part with adjustable gas atmospheres via b) gas inlet and outlet, II) the upper part with c) electrical contacting, and a) the electrical heater. 62
Figure 3.43: SOPEC-RR_V1 tubular reactor in assembled state with cooling system on a) the top part and b) the bottom part, c) an oxygen probe for analytical investigation, and d) mouth for introducing the light with a quartz rod, electrical contacting and thermocouple; e) the cell is fixed between two corundum (Al_2O_3) tubes. 63
Figure 3.44: Composition of the SOPEC cell with the sample ID: GB_SOPEC_V1.6.. 64
Figure 3.45: Sketch of investigated SOPEC cell with the measurement arrangement.64
Figure 3.46: Scheme of defect chemistry in yttria stabilized zirconia (YSZ). 65
Figure 3.47: a, c, e, g, i) Open circuit voltage ($U_{PV,OC}$) after switching UV on and voltage under working condition of the SOPEC cell (U_{PEC}) after short-circuiting the illuminated PEC cell at a) 400 °C, c) 425 °C, e) 450 °C, g) 475 °C and i) 500 °C in symmetric gas atmospheres, UV on–off is indicated. b, d, f, h, j) corresponding current of the PEC cell (I_{PEC}). 67
Figure 3.48: Measurement arrangement for *I-V* characterization. 68
Figure 3.49: *I–V* characteristics of the HT-PV cell solely, obtained by measuring U_{PV} and I_{PV} for different electrical loads and temperatures from 400°C to 500°C. 68
Figure 3.50: Open circuit voltages ($U_{PV,OC}$) of the HT-PV cell, voltage loss in the HT-PV cell (η_{PV}) and voltages U_{PEC} of the operating SOPEC cell at temperatures from 400 to 500°C in symmetric gas atmospheres. 69
Figure 3.51: Short-circuit currents of the PV cell solely ($I_{PV,SC}$) and of the PEC cell (I_{PEC}) at temperatures from 400 to 500°C in symmetric gas atmospheres. 70
Figure 3.52: Sealing ring in the evacuated part of the tubular reactor. 71
Figure 3.53: Sealing ring in the open part of the tubular reactor. 71
Figure 3.54: Bottom part of SOPEC-RR-V1with the positioned SOPEC cell. 71
Figure 3.55: Upper part of SOPEC-RR-V with guiding rods, pressure springs and screws. 71
Figure 3.56: a,d,g) Voltage U_{PEC} of the cell with an open circuit voltage before UV on close to 100 mV due to asymmetric gas atmospheres. b,e,h) Current I_{PEC} upon UV

light under short-circuit condition. c,f,i) Upon UV light, the oxygen fraction f_{O2} in the gas chambers lowered from 600 to 480 ppm at 400°C, 640 to 400 ppm at 450°C, and 600 to 310 ppm at 500°C. 75
Figure 4.1: a) Sketch of the investigated solid oxide photoelectrochemical cell (SOPEC cell) and the measurement arrangement. b) SEM cross section image of a 20% Sr doped $LaCrO_3$ (LSCr82) layer on a (100) $SrTiO_3$ single crystal. c) Sketch of the entire setup for investigating the photoelectrochemical cell with two different gas chambers. d) Circuit representing the entire PEC cell. Both the PV and EC part are represented by an ideal battery with internal resistance. The PV "battery" with voltage $U_{PV,OC}$ operates only under illumination and the Nernst voltage U_N is only effective for asymmetric gas supply. 79
Figure 4.2: (a), (c) Open circuit voltage ($U_{PV,OC}$) after switching UV on and voltage under working condition of the PEC cell (U_{PEC}) after short-circuiting (SC) the illuminated PEC cell at 400°C (a) and 500°C (c) in symmetric gas atmospheres, $T = T_{dark}$, UV on-off is indicated. (b), (d) Corresponding current of the PEC cell (I_{PEC}). 81
Figure 4.3: (a) PV cell open circuit voltages ($U_{PV,OC}$) and voltages U_{PEC} of the operating SOPEC cell at temperatures from 400-500°C ($T = T_{dark}$) in symmetric gas atmospheres. (b) Short-circuit currents of the PV cell solely ($I_{PV,SC}$) and of the PEC cell (I_{PEC}) at temperatures from 400-500°C in symmetric gas atmospheres. 82
Figure 4.4: Results of the photoelectrochemically driven oxygen pumping experiment performed in asymmetric gas atmospheres at 400°C (top) and 500°C (bottom), $T = T_{dark}$, UV on-off is indicated. (a), (d) Voltage U_{PEC} of the cell with an open circuit voltage before UV on close to 100 mV due to asymmetric gas atmospheres. (b), (e) Current I_{PEC} upon UV light under short-circuit condition. (c), (f) Under UV light the oxygen fraction f_{O2} in the gas chamber is lowered from 600 ppm to 480 ppm at 400°C and 310 ppm at 500°C..... 83
Figure 4.5: *I-V* characteristics of the PV cell solely, obtained by measuring U_{PV} and I_{PV} for different loads and temperatures from 400°C to 500°C ($T = T_{dark}$). 86
Figure 4.6: (a) Temperature dependent resistances of the PV cell in the operating SOPEC cell ($R_{PV,PEC}$, $T = T_{dark}$), the corresponding total AC resistance of the illuminated PV cell ($R_{PV,AC,ill}$, $T = T_{UV}$) and the approximate differential resistances $R_{PV,diff}$ ($T = T_{UV}$) obtained by linearizing the *I-V* curves at temperatures between 400 and 500°C. (b) Temperature dependent resistances $R_{EC,PEC}$ calculated from U_{PEC}/I_{PEC} ($T = T_{dark}$) of the illuminated SOPEC cell and the total AC resistances of the illuminated cell ($R_{EC,AC,ill}$, $T = T_{UV}$) at temperatures between 400 and 500°C. 87
Figure 4.7: (a) Impedance spectrum of the dark PV cell at 450°C; the large arc is caused by the $SrTiO_3$/LSCr82 interface. The inset shows a magnification of the spectrum part caused by the $SrTiO_3$ single crystal and the spectrum of a $SrTiO_3$ single

crystal with Pt instead of the LSCr82 as top electrode. (b) Spectra of the illuminated PV cell measured at 400 - 500°C ($T = T_{UV}$) under short-circuit condition. (c) Impedance spectra of the EC cell before and during illumination of the short-circuited PEC cell at 450°C ($T = T_{UV}$ for UV on, and $T = T_{dark}$ for UVoff). 88
Figure 4.8: Wavelength dependent transmission of light through a $SrTiO_3$ single crystal (0.5 mm thickness) as function of temperature measured in air. Band gap energies E_g are deduced from half maximum transmission and also indicated ($T = T_{setup}$). 90
Figure 4.9: Ratio of the two PEC cell internal resistances, *i.e.* of the PV cell resistance $R_{PV,PEC}$ and the EC cell resistance $R_{EC,PEC}$ for temperatures between 400 and 500°C ($T = T_{dark}$). 92

5.2 List of tables

Table 2.1: Exergy analysis of two-step water-splitting thermochemical cycle using Zn/ZnO material system. ZnO and H_2O molar flow rates are set to 1 mol/s. 16
Table 2.2: Exergy analysis of two-step water-splitting thermochemical cycle using FeO/Fe_3O_4 material system. Fe_3O_4 and H_2O molar flow rates are set to 1 mol/s. 17
Table 2.3: Exergy analysis of two-step water-splitting thermochemical cycle using Ce_2O_3/CeO_2 material system. The molar flow rates of CeO_2 is set to 2 mol/s and H_2O is set to 1 mol/s. 17
Table 3.1: Summarized results from *I-V* characterization under illumination with 10 W-LED/405 nm. 61
Table 3.2: Summarized results from *I-V* characterization under illumination with 10 W-LED/365 nm. 61
Table 3.3: Summarized results of voltages and currents of the HT-PV cell and of the SOPEC cell from 400 to 500°C. 69
Table 4.1: Decrease of the oxygen content in the gas flow at different temperatures and the current of the PEC cell, $T = T_{dark}$. 84

5.3 References

[1] M. Carmo, D. L. Fritz, J. Mergel, D. Stolten: "A comprehensive review on PEM water electrolysis"; *International Journal of Hydrogen Energy* **2013,** *38* (12), 4901-4934.

[2] J. Mergel, M. Carmo, D. L. Fritz, in *Transition to Renewable Energy Systems* (Ed: D. Stolten, V. Scherer), Wiley-VCH, Weinheim, **2013**, 425-450.

[3] M. Zahid, J. Schefold, A. Brisse, in *Hydrogen and fuel cells: Fundamentals, Technologies and Applications* (Ed: D. Stolten), Wiley-VCH, Weinheim, **2010**, 227-242.

[4] M. Laguna-Bercero: "Recent advances in high temperature electrolysis using solid oxide fuel cells: A review"; *Journal of Power Sources* **2012,** *203*, 4-16.

[5] A. Ursua, L. M. Gandia, P. Sanchis: "Hydrogen production from water electrolysis: current status and future trends"; *Proceedings of the IEEE* **2012,** *100* (2), 410-426.

[6] Q. Fu, C. Mabilat, M. Zahid, A. Brisse, L. Gautier: "Syngas production via high-temperature steam/CO_2 co-electrolysis: an economic assessment"; *Energy & Environmental Science* **2010,** *3* (10), 1382-1397.

[7] V. N. Nguyen, L. Blum: "Syngas and Synfuels from H_2O and CO_2: Current Status"; *Chemie Ingenieur Technik* **2015,** *87* (4), 354-375.

[8] C. M. Stoots, J. E. O'Brien, J. S. Herring, J. J. Hartvigsen: "Syngas production via high-temperature coelectrolysis of steam and carbon dioxide"; *Journal of Fuel Cell Science and Technology* **2009,** *6* (1), 011014.

[9] I. Barin, *Thermochemical Data of Pure Substances*, VCH Verlagsgesellschaft mbH, Weinheim, **1989**, Part I, p 649.

[10] J. Larminie, A. Dicks, M. S. McDonald, *Fuel cell systems explained*, Wiley New York, **2003**, 2.

[11] A. Steinfeld, A. Meier: "Solar fuels and materials"; *Encyclopedia of Energy* **2004,** *5*, 623-637.

[12] IEA, "2014 Key World Energy Statistics". International Energy Agency (IEA): 2014; pp 6, 24, 28.

[13] A. J. Morris, G. J. Meyer, E. Fujita: "Molecular approaches to the photocatalytic reduction of carbon dioxide for solar fuels"; *Accounts of Chemical Research* **2009,** *42* (12), 1983-1994.

[14] G. Centi, S. Perathoner: "Towards solar fuels from water and CO_2"; *ChemSusChem* **2010,** *3* (2), 195-208.

[15] A. Le Gal, S. Abanades, G. Flamant: "CO_2 and H_2O splitting for thermochemical production of solar fuels using nonstoichiometric ceria and ceria/zirconia solid solutions"; *Energy & Fuels* **2011,** *25* (10), 4836-4845.

[16] G. P. Smestad, A. Steinfeld: "Review: Photochemical and thermochemical production of solar fuels from H_2O and CO_2 using metal oxide catalysts"; *Industrial & Engineering Chemistry Research* **2012,** *51* (37), 11828-11840.

[17] V. Artero, M. Fontecave: "Solar fuels generation and molecular systems: is it homogeneous or heterogeneous catalysis?"; *Chemical Society Reviews* **2013,** *42* (6), 2338-2356.

[18] S. Abanades, P. Charvin, G. Flamant, P. Neveu: "Screening of water-splitting thermochemical cycles potentially attractive for hydrogen production by concentrated solar energy"; *Energy* **2006,** *31* (14), 2805-2822.

[19] A. Brisse, J. Schefold, M. Zahid: "High temperature water electrolysis in solid oxide cells"; *International Journal of Hydrogen Energy* **2008,** *33* (20), 5375-5382.

[20] M. Kato, T. Cardona, A. W. Rutherford, E. Reisner: "Photoelectrochemical water oxidation with photosystem II integrated in a mesoporous indium–tin oxide electrode"; *Journal of the American Chemical Society* **2012,** *134* (20), 8332-8335.

[21] A. Fujishima, K. Honda: "Electrochemical photolysis of water at a semiconductor electrode"; *Nature* **1972,** *238*, 37-38.

[22] J. Nitsch, C.-J. Winter: "Solar hydrogen energy in the F.R. of Germany: 12 theses"; *International Journal of Hydrogen Energy* **1987,** *12* (10), 663-667.

[23] E. A. Fletcher, R. L. Moen: "Hydrogen-and oxygen from water"; *Science* **1977,** *197* (4308), 1050-1056.

[24] S. Ihara: "Feasibility of hydrogen production by direct water splitting at high temperature"; *International Journal of Hydrogen Energy* **1978,** *3* (3), 287-296.

[25] S. Ihara: "Direct thermal decomposition of water"; *Solar-hydrogen energy systems* **1979,** *1*, 59-79.

[26] C. Bale, E. Bélisle, P. Chartrand, S. Decterov, G. Eriksson, K. Hack, I.-H. Jung, Y.-B. Kang, J. Melançon, A. Pelton: "FactSage thermochemical software and databases—recent developments"; *Calphad* **2009,** *33* (2), 295-311.

[27] A. Steinfeld: "Solar hydrogen production via a two-step water-splitting thermochemical cycle based on Zn/ZnO redox reactions"; *International Journal of Hydrogen Energy* **2002,** *27* (6), 611-619.

[28] A. Steinfeld, S. Sanders, R. Palumbo: "Design aspects of solar thermochemical engineering—a case study: two-step water-splitting cycle using the Fe_3O_4/FeO redox system"; *Solar Energy* **1999,** *65* (1), 43-53.

[29] R. B. Diver, J. E. Miller, M. D. Allendorf, N. P. Siegel, R. E. Hogan: "Solar thermochemical water-splitting ferrite-cycle heat engines"; *Journal of Solar Energy Engineering* **2008,** *130* (4), 041001.

[30] S. Abanades, G. Flamant: "Thermochemical hydrogen production from a two-step solar-driven water-splitting cycle based on cerium oxides"; *Solar Energy* **2006,** *80* (12), 1611-1623.

[31] W. C. Chueh, C. Falter, M. Abbott, D. Scipio, P. Furler, S. M. Haile, A. Steinfeld: "High-flux solar-driven thermochemical dissociation of CO_2 and H_2O using nonstoichiometric ceria"; *Science* **2010,** *330* (6012), 1797-1801.

[32] M. Romero, A. Steinfeld: "Concentrating solar thermal power and thermochemical fuels"; *Energy & Environmental Science* **2012,** *5* (11), 9234-9245.

[33] K. Lovegrove, W. Stein, *Concentrating solar power technology: principles, developments and applications*, Elsevier, **2012**, ISBN: 0857096176.

[34] Y. Tamaura, A. Steinfeld, P. Kuhn, K. Ehrensberger: "Production of solar hydrogen by a novel, 2-step, water-splitting thermochemical cycle"; *Energy* **1995,** *20* (4), 325-330.

[35] M. Roeb, C. Sattler, R. Klüser, N. Monnerie, L. de Oliveira, A. G. Konstandopoulos, C. Agrafiotis, V. Zaspalis, L. Nalbandian, A. Steele: "Solar hydrogen production by a two-step cycle based on mixed iron oxides"; *Journal of Solar Energy Engineering* **2006,** *128* (2), 125-133.

[36] H. Ishihara, H. Kaneko, N. Hasegawa, Y. Tamaura: "Two-step water splitting process with solid solution of YSZ and Ni-ferrite for solar hydrogen production (ISEC 2005-76151)"; *Journal of Solar Energy Engineering* **2008,** *130* (4), 044501.

[37] B. M. Abraham, F. Schreiner: "General principles underlying chemical cycles which thermally decompose water into the elements"; *Industrial & Engineering Chemistry Fundamentals* **1974,** *13* (4), 305-310.

[38] J. O'Brien, In: *Thermodynamic Considerations for Thermal Water Splitting Processes and High-Temperature Electrolysis*, 2008 ASME International Congress and Exposition, paper# IMECE2008-68880, Boston, **2008**.

[39] B. Yildiz, M. S. Kazimi: "Efficiency of hydrogen production systems using alternative nuclear energy technologies"; *International Journal of Hydrogen Energy* **2006,** *31* (1), 77-92.

[40] J. E. O'Brien: "Thermodynamics and transport phenomena in high t emperature steam electrolysis cells"; *Journal of Heat Transfer* **2012,** *134* (3), 031017.

[41] J. B. Hansen: "Solid oxide electrolysis–a key enabling technology for sustainable energy scenarios"; *Faraday Discussions* **2015,** *182*, 9-48.

[42] S. Licht, B. Wang, S. Ghosh, H. Ayub, D. Jiang, J. Ganley: "A new solar carbon capture process: solar thermal electrochemical photo (STEP) carbon capture"; *The Journal of Physical Chemistry Letters* **2010,** *1* (15), 2363-2368.

[43] A. Roine, P. Lamberg, J. Mansikka-aho, P. Björklund, J.-P. Kentala, T. Talonen *HSC Chemistry*, 6.12; Outotec Research Oy: Finnland, 1974-2007.

[44] A. Fujishima, K. Kohayakawa, K. Honda: "Formation of hydrogen gas with an electrochemical photo-cell"; *Bulletin of the Chemical Society of Japan* **1975,** *48* (3), 1041-1042.

[45] H. O. Finklea, *Titanium dioxide (TiO_2) and strontium titanate ($SrTiO_3$). Chapter 2*, In *Semiconductor electrodes*, **1988**.

[46] T. Bak, J. Nowotny, M. Rekas, C. Sorrell: "Photo-electrochemical hydrogen generation from water using solar energy. Materials-related aspects"; *International Journal of Hydrogen Energy* **2002,** *27* (10), 991-1022.

[47] A. Fujishima, X. Zhang, D. A. Tryk: "TiO_2 photocatalysis and related surface phenomena"; *Surface Science Reports* **2008,** *63* (12), 515-582.

[48] T. Ohnishi, Y. Nakato, H. Tsubomura: "The Quantum Yield of Photolysis of Water on TiO_2 Electrodes"; *Berichte der Bunsengesellschaft für Physikalische Chemie* **1975,** *79* (6), 523-525.

[49] M. S. Wrighton, A. B. Ellis, P. T. Wolczanski, D. L. Morse, H. B. Abrahamson, D. S. Ginley: "Strontium titanate photoelectrodes. Efficient photoassisted electrolysis of water at zero applied potential"; *Journal of the American Chemical Society* **1976,** *98* (10), 2774-2779.

[50] J. Nowotny, C. Sorrell, T. Bak, L. Sheppard: "Solar-hydrogen: Unresolved problems in solid-state science"; *Solar Energy* **2005,** *78* (5), 593-602.

[51] T. Bak, J. Nowotny, M. Rekas, C. Sorrell: "Photo-electrochemical properties of the TiO_2-Pt system in aqueous solutions"; *International Journal of Hydrogen Energy* **2002,** *27* (1), 19-26.

[52] R. van de Krol, Y. Liang, J. Schoonman: "Solar hydrogen production with nanostructured metal oxides"; *Journal of Materials Chemistry* **2008,** *18* (20), 2311-2320.

[53] L. Andrade, T. Lopes, H. A. Ribeiro, A. Mendes: "Transient phenomenological modeling of photoelectrochemical cells for water splitting–Application to undoped hematite electrodes"; *International Journal of Hydrogen Energy* **2011,** *36* (1), 175-188.

[54] L. Sheppard, J. Nowotny: "Materials for photoelectrochemical energy conversion"; *Advances in Applied Ceramics* **2007,** *106* (1-2), 9-20.

[55] A. Murphy, P. Barnes, L. Randeniya, I. Plumb, I. Grey, M. Horne, J. Glasscock: "Efficiency of solar water splitting using semiconductor electrodes"; *International Journal of Hydrogen Energy* **2006,** *31* (14), 1999-2017.

[56] R. Dholam, N. Patel, M. Adami, A. Miotello: "Physically and chemically synthesized TiO_2 composite thin films for hydrogen production by photocatalytic water splitting"; *International Journal of Hydrogen Energy* **2008,** *33* (23), 6896-6903.

[57] S. Licht: "Solar water splitting to generate hydrogen fuel: photothermal electrochemical analysis"; *The Journal of Physical Chemistry B* **2003,** *107* (18), 4253-4260.

[58] S. Licht: "Solar water splitting to generate hydrogen fuel—a photothermal electrochemical analysis"; *International Journal of Hydrogen Energy* **2005,** *30* (5), 459-470.

[59] J. M. Bolts, M. S. Wrighton: "Correlation of photocurrent-voltage curves with flat-band potential for stable photoelectrodes for the photoelectrolysis of water"; *The Journal of Physical Chemistry* **1976,** *80* (24), 2641-2645.

[60] J. Mavroides, J. Kafalas, D. Kolesar: "Photoelectrolysis of water in cells with $SrTiO_3$ anodes"; *Applied Physics Letters* **1976,** *28* (5), 241-243.

[61] F. Williams, A. Nozik: "Irreversibilities in the mechanism of photoelectrolysis"; *Nature* **1978,** *271*, 137-139.

[62] H.-X. Chen, Z.-X. Wei, Y. Wang, W.-W. Zeng, C.-M. Xiao: "Preparation of $SrTi_{0.1}Fe_{0.9}O_{3-\delta}$ and its photocatalysis activity for degradation of methyl orange in water"; *Materials Chemistry and Physics* **2011,** *130* (3), 1387-1393.

[63] E. Jeong, S. Yu, J. Yoon, J. Bae, C. Cho, K. Lim, P. Borse, H. Kim: "The codopant concentration dependence on visible light photocatalytic efficiency in

$SrTi_{1-x}Fe_{[x/2]}Cr_{[x/2]}O_3$ ($0.01 \leq x \leq 0.2$) perovskite photocatalysts"; *Journal of Ceramic Processing Research* **2012,** *13* (5), 517-522.

[64] P. Reunchan, N. Umezawa, S. Ouyang, J. Ye: "Mechanism of photocatalytic activities in Cr-doped $SrTiO_3$ under visible-light irradiation: an insight from hybrid density-functional calculations"; *Physical Chemistry Chemical Physics* **2012,** *14* (6), 1876-1880.

[65] Y. Su, S. Wang, Y. Meng, H. Han, X. Wang: "Dual substitutions of single dopant Cr^{3+} in perovskite $NaTaO_3$: synthesis, structure, and photocatalytic performance"; *RSC Advances* **2012,** *2* (33), 12932-12939.

[66] M. Yang, X. Huang, S. Yan, Z. Li, T. Yu, Z. Zou: "Improved hydrogen evolution activities under visible light irradiation over $NaTaO_3$ codoped with lanthanum and chromium"; *Materials Chemistry and Physics* **2010,** *121* (3), 506-510.

[67] P. Kanhere, J. Nisar, Y. Tang, B. Pathak, R. Ahuja, J. Zheng, Z. Chen: "Electronic structure, optical properties, and photocatalytic activities of $LaFeO_3$–$NaTaO_3$ solid solution"; *The Journal of Physical Chemistry C* **2012,** *116* (43), 22767-22773.

[68] R. Dholam, N. Patel, M. Adami, A. Miotello: "Hydrogen production by photocatalytic water-splitting using Cr-or Fe-doped TiO_2 composite thin films photocatalyst"; *International Journal of Hydrogen Energy* **2009,** *34* (13), 5337-5346.

[69] T. Bak, M. Nowotny, L. Sheppard, J. Nowotny: "Charge transport in Cr-doped titanium dioxide"; *The Journal of Physical Chemistry C* **2008,** *112* (18), 7255-7262.

[70] A. K. Rumaiz, J. Woicik, E. Cockayne, H. Lin, G. H. Jaffari, S. I. Shah: "Oxygen vacancies in N doped TiO_2: Experiment and first principle calculations"; *Applied Physics Letters* **2009,** *95*, 262111.

[71] G. Brunauer. Exergieanalyse von solargetriebenen Kreisprozessen zur regenerativen Produktion von Wasserstoff und dem Ausblick auf ein grundlegend neuartiges Verfahrensblick. Diplomarbeit, TU Vienna, Vienna, **2011**.

[72] G. Brunauer, AT 510 156 B1, 2012-02-15, **2012**.

[73] G. Brunauer, J. Fleig, M. Ahrens, K. Ponweiser, M. Haider, WO 2012/045104 A1, 2012-04-12, **2012**.

[74] G. Brunauer, J. Fleig, M. Ahrens, K. Ponweiser, M. Haider, EP 2 625 315 B1, 2015-09-30, **2015**.

[75] A. Nenning, A. K. Opitz, G. Brunauer, M. Ahrens, J. Fleig, In: *Solid State Ionics: Mass and Charge Transport across and along Interfaces of Functional Materials*, E-MRS Spring Meeting, Strasbourg, 2012-05-14 - 2012-05-18; Strasbourg, **2012**.

[76] A. Nenning, A. K. Opitz, G. Brunauer, S. Kogler, B. Rotter, J. Fleig, In: *Topical Issues of Rational Use of Natural Sources*, St. Petersburg, 2013-04-24 - 2013-04-26; St. Petersburg, **2012**, ISBN: 978-5-94211-646-0,pp 234-235.

[77] A. Nenning, A. Opitz, T. Huber, J. Fleig: "A novel approach for analyzing electrochemical properties of mixed conducting solid oxide fuel cell anode materials by impedance spectroscopy"; *Physical Chemistry Chemical Physics* **2014,** *16* (40), 22321-22336.

[78] F. Kröger, H. Vink: "Relations between the concentrations of imperfections in solids"; *Journal of Physics and Chemistry of Solids* **1958,** *5* (3), 208-223.

[79] A. Rothschild, W. Menesklou, H. L. Tuller, E. Ivers-Tiffee: "Defect Chemistry, and Transport Properties of $SrTi_{1-x}Fe_xO_{3-y}$ Solid Solutions "; *Chemistry of Materials* **2006,** *18* (16), 3651-3659.

[80] W. Jung, H. L. Tuller: "Investigation of Cathode Behavior of Model Thin-Film $SrTi_{1-x}Fe_xO_{3-\delta}$ (x= 0.35 and 0.5) Mixed Ionic-Electronic Conducting Electrodes"; *Journal of the Electrochemical Society* **2008,** *155* (11), B1194-B1201.

[81] R. Merkle, R. A. De Souza, J. Maier: "Optically Tuning the Rate of Stoichiometry Changes: Surface-Controlled Oxygen Incorporation into Oxides under UV Irradiation"; *Angewandte Chemie* **2001,** *113* (11), 2184-2187.

[82] J. Fleig, F. S. Baumann, V. Brichzin, H. R. Kim, J. Jamnik, G. Cristiani, H. U. Habermeier, J. Maier: "Thin film microelectrodes in SOFC electrode research"; *Fuel Cells* **2006,** *6* (3-4), 284-292.

[83] J. Fleig, H. R. Kim, J. Jamnik, J. Maier: "Oxygen Reduction Kinetics of Lanthanum Manganite (LSM) Model Cathodes: Partial Pressure Dependence and Rate-Limiting Steps"; *Fuel Cells* **2008,** *8* (5), 330-337.

[84] S. Kogler, A. Nenning, G. M. Rupp, A. K. Opitz, J. Fleig: "Comparison of Electrochemical Properties of $La_{0.6}Sr_{0.4}FeO_{3-\delta}$ Thin Film Electrodes: Oxidizing vs. Reducing Conditions"; *Journal of The Electrochemical Society* **2015,** *162* (3), F317-F326.

[85] P. V. Sushko, L. Qiao, M. Bowden, T. Varga, G. J. Exarhos, F. K. Urban III, D. Barton, S. A. Chambers: "Multiband optical absorption controlled by lattice strain in thin-film $LaCrO_3$"; *Physical Review Letters* **2013,** *110* (7), 077401.

[86] K. Maiti, D. Sarma: "Electronic structure of La_{1-x} Sr_xCrO_3"; *Physical Review B* **1996,** *54* (11), 7816.

[87] I. Denk, W. Münch, J. Maier: "Partial Conductivities in $SrTiO_3$: Bulk Polarization Experiments, Oxygen Concentration Cell Measurements, and Defect-Chemical Modeling"; *Journal of the American Ceramic Society* **1995,** *78* (12), 3265-3272.

[88] G. M. Choi, H. L. Tuller: "Defect Structure and Electrical Properties of Single-Crystal $Ba_{0.03}Sr_{0.97}TiO_3$"; *Journal of the American Ceramic Society* **1988,** *71* (4), 201-205.

[89] R. Buttner, E. Maslen: "Electron difference density and structural parameters in $CaTiO_3$"; *Acta Crystallographica Section B: Structural Science* **1992,** *48* (5), 644-649.

[90] H. Kay, P. Bailey: "Structure and properties of $CaTiO_3$"; *Acta Crystallographica* **1957,** *10* (3), 219-226.

[91] G. C. Brunauer, B. Rotter, G. Walch, E. Esmaeili, A. K. Opitz, K. Ponweiser, J. Summhammer, J. Fleig: "UV-Light Driven Oxygen Pumping in a High-Temperature Solid Oxide Photoelectrochemical Cell"; *Advanced Functional Materials* **2016,** *26* (1), 120-128.

[92] M. Uzunoglu, O. Onar, M. Alam: "Modeling, control and simulation of a PV/FC/UC based hybrid power generation system for stand-alone applications"; *Renewable Energy* **2009,** *34* (3), 509-520.

[93] T. L. Gibson, N. A. Kelly: "Predicting efficiency of solar powered hydrogen generation using photovoltaic-electrolysis devices"; *International Journal of Hydrogen Energy* **2010,** *35* (3), 900-911.

[94] O. Khaselev, J. A. Turner: "A monolithic photovoltaic-photoelectrochemical device for hydrogen production via water splitting"; *Science* **1998,** *280* (5362), 425-427.

[95] G. Wang, H. Wang, Y. Ling, Y. Tang, X. Yang, R. C. Fitzmorris, C. Wang, J. Z. Zhang, Y. Li: "Hydrogen-treated TiO_2 nanowire arrays for photoelectrochemical water splitting"; *Nano Letters* **2011,** *11* (7), 3026-3033.

[96] A. Valdes, J. Brillet, M. Grätzel, H. Gudmundsdottir, H. A. Hansen, H. Jonsson, P. Klüpfel, G.-J. Kroes, F. Le Formal, I. C. Man: "Solar hydrogen production with semiconductor metal oxides: new directions in experiment and theory"; *Physical Chemistry Chemical Physics* **2012,** *14* (1), 49-70.

[97] F. E. Osterloh: "Inorganic materials as catalysts for photochemical splitting of water"; *Chemistry of Materials* **2008,** *20* (1), 35-54.

[98] J. Gan, X. Lu, Y. Tong: "Towards highly efficient photoanodes: boosting sunlight-driven semiconductor nanomaterials for water oxidation"; *Nanoscale* **2014,** *6* (13), 7142-7164.

[99] P. Haueter, S. Moeller, R. Palumbo, A. Steinfeld: "The production of zinc by thermal dissociation of zinc oxide—solar chemical reactor design"; *Solar Energy* **1999,** *67* (1), 161-167.

[100] X. Ye, J. Melas-Kyriazi, Z. A. Feng, N. A. Melosh, W. C. Chueh: "A semiconductor/mixed ion and electron conductor heterojunction for elevated-temperature water splitting"; *Physical Chemistry Chemical Physics* **2013,** *15* (37), 15459-15469.

[101] F. Horikiri, T. Ichikawa, L. Q. Han, A. Kaimai, K. Yashiro, H. Matsumoto, T. Kawada, J. Mizusaki: "Nb-doped $SrTiO_3$-based high-temperature Schottky solar cells"; *Japanese Journal of Applied Physics* **2005,** *44* (11R), 8023.

[102] G. Walch, A. K. Opitz, S. Kogler, J. Fleig: "Correlation between hydrogen production rate, current, and electrode overpotential in a solid oxide electrolysis cell with $La_{0.6}Sr_{0.4}FeO_{3-\delta}$ thin-film cathode"; *Monatshefte fuer Chemie* **2014,** *145* (7), 1055-1061.

[103] R. A. De Souza, V. Metlenko, D. Park, T. E. Weirich: "Behavior of oxygen vacancies in single-crystal $SrTiO_3$: Equilibrium distribution and diffusion kinetics"; *Physical Review B* **2012,** *85* (17), 174109.

[104] H. K. Heinisch, in *Semiconductor Contacts* (Ed: Clarendon, Oxford, **1984**.

[105] J. Fleig, S. Rodewald, J. Maier: "Microcontact impedance measurements of individual highly resistive grain boundaries: General aspects and application to acceptor-doped $SrTiO_3$"; *Journal of Applied Physics* **2000,** *87* (5), 2372-2381.

[106] M. Cardona: "Optical Properties and Band Structure of $SrTiO_3$ and $BaTiO_3$"; *Physical Review* **1965,** *140* (2A), A651.

[107] K. Van Benthem, C. Elsässer, R. French: "Bulk electronic structure of $SrTiO_3$: Experiment and theory"; *Journal of Applied Physics* **2001,** *90* (12), 6156-6164.

[108] K. H. Zhang, Y. Du, A. Papadogianni, O. Bierwagen, S. Sallis, L. F. Piper, M. E. Bowden, V. Shutthanandan, P. V. Sushko, S. A. Chambers: "Perovskite Sr-Doped $LaCrO_3$ as a New p-Type Transparent Conducting Oxide"; *Advanced Materials* **2015**.

[109] N. Bonanos, R. Slotwinski, B. Steele, E. Butler: "High ionic conductivity in polycrystalline tetragonal Y_2O_3-ZrO_2"; *Journal of Materials Science Letters* **1984,** *3* (3), 245-248.

[110] B. Boukamp, T. Raming, A. Winnubst, H. Verweij: "Electrochemical characterisation of 3Y-TZP–Fe_2O_3 composites"; *Solid State Ionics* **2003,** *158* (3), 381-394.

[111] S. B. Adler, J. Lane, B. Steele: "Electrode Kinetics of Porous Mixed-Conducting Oxygen Electrodes"; *Journal of The Electrochemical Society* **1996,** *143* (11), 3554-3564.

5.4 Curriculum vitae (CV)

PERSONAL DATA

Name	Georg Christoph BRUNAUER
Degrees	MSc MSc
Address	THERESIA PAMPICHLER STRAßE 44/1, 2000 STOCKERAU, AUSTRIA
Telephone	+43 664 9130129
email	georg.brunauer@a1.net
	georg.brunauer@tuwien.ac.at
Nationality	Austria
Date of birth	November 8, 1979

PRIMARY EDUCATION

Nursery school	September, 1986 – July, 1987
Elementary school	September, 1987 – July, 1991
Secondary School	September, 1991 – July, 1995

PROFESSION

• Begin - End	September, 1995 – August, 1999
• Employer's address	Elektrounternehmen Franz Brötzner A-5411 - Oberalm bei Hallein (electro enterprise)
• Profession	• Apprenticeship (Electrical Engineering) • Apprenticeship degree with state award and further occupation as Electrical Engineer

MILITARY SERVICE

• Basic service	August, 1999 – November, 2000
• Regular soldier	December, 2000 to November, 2003 • Paramedic • Medical Engineering

CONTINUING EDUCATION

• Begin – End	September, 2000 – November, 2002
• Institution	Austrian Federal Economic Chamber
• Qualification	A – level

UNIVERSITY STUDY

• Begin – End	October, 2003 – July, 2007
• University	University of Applied Science, Upper Austria (FH Wels)
• Kind of course	Automation Engineering

INTERDISCIPLINARY PROJECTS DURING THE STUDY

• Title of projects	Procedure of permission for a train control system based on autonomous train positioning	Conception of an automatic door system for a indoor hospital area, including emergency rooms
• Begin – End	March – July, 2005	October, 2005 – February, 2006
• Involved companies	Fa. Stern & Hafferl; A – 4810 Gmunden	Fa. Aumayr; A - 4221 Steyregg

OBLIGATED PRACTICAL TRAINING AND DIPLOMA THESIS

• Issue	Practical training:	Diploma thesis:
• Title and work package	Technical analysis of an electrolyser (separating of water to hydrogen and oxygen)	Conception of a DC – direct coupled autonomous solar hydrogen electrolyse
• Begin – End	September, 2006 – February, 2007	March, 2007 – July, 2007
• Involved company	Fa. Fronius International; A – 4600 Wels / Thalheim	Fa. Fronius International; A – 4600 Wels / Thalheim

CONTINUING UNIVERSITY STUDY

• Begin – End	March, 2008 – March 2009
• University	Vienna University of Technology, Austria
	Doctorial study
• Kind of program	Additional requirements for completing technical programmes according to s. 5 ss. 3 of the Technical Colleges Act ("Fachhochschulgesetz")
• Begin – End	August, 2010 – July, 2011
• University	Vienna University of Technology, Austria
	Master's course
• Kind of program	Chemical process engineering
• Begin	since March, 2009
• University	Vienna University of Technology, Austria
	Doctorial study
• Kind of program	Chemical process engineering

AWARDS

INiTS - Award	2011 – 3rd place, Category: General Technology

Version: July, 2016